Stereoscopic Particle Image Velocimetry Measurements of Swirl Distortion on a Full-Scale Turbofan Engine Inlet

Michael A. Nelson

Thesis submitted to the faculty of the
Virginia Polytechnic Institute and State University
in partial fulfillment of the requirements for the degree of

Master of Science
in
Aerospace Engineering

K. Todd Lowe, Chair
Walter F. O'Brien
Aurelien Borgoltz
Clinton L. Dancey

August 14, 2014
Blacksburg, Virginia

Keywords: Swirl Distortion, Particle Image Velocimetry, StreamVane, Hybrid Wing Body, Uncertainty

Stereoscopic Particle Image Velocimetry Measurements of Swirl Distortion on a Full-Scale Turbofan Engine Inlet

Michael A. Nelson

ABSTRACT

There is a present need for simulation and measuring the inlet swirl distortion generated by airframe/engine system interactions to identify potential degradation in fan performance and operability in a full-scale, ground testing environment. Efforts are described to address this need by developing and characterizing methods for complex, prescribed distortion patterns. A relevant inlet swirl distortion profile that mimics boundary layer ingesting inlets was generated by a novel new method, dubbed the StreamVane method, and measured in a sub scale tunnel using stereoscopic particle image velocimetry (SPIV) as a precursor for swirl distortion generation and characterization in an operating turbofan research engine. Diagnostic development efforts for the distortion measurements within the research engine paralleled the StreamVane characterization. The system used for research engine PIV measurements is described. Data was obtained in the wake of a total pressure distortion screen for engine conditions at idle and 80% corrected fan speed, and of full-scale StreamVane screen at 50% corrected fan speed. The StreamVane screen was designed to generate a swirl distortion that is representative for hybrid wing body applications and was made of Ultem*9085 using additive manufacturing. Additional improvements to the StreamVane method are also described. Data reduction algorithms are put forth to reduce spurious velocity vectors. Uncertainty estimations specific to the inlet distortion test rig, including bias error due to mechanical vibration, are made. Results indicate that the methods develop may be used to both generate and characterize complex distortion profiles at the aerodynamic interface plane, providing new information about airframe/engine integration.

Acknowledgements

I would first like to thank Virginia Tech and NASA for providing financial support of this research, without which these experiments would not have been possible. Fay Collier, Hamilton Fernandez, and Greg Gatlin of NASA are gratefully acknowledged for their insight, direction, and support in the development of this project. I would also like to acknowledge Bo Walkley of the National Institute of Aerospace, Ron Kawai of Boeing, and Wes Lord of Pratt & Whitney for their important industry perspective and input that has allowed this project to be a success both in organizational collaboration and real world application of technology.

I also wish to thank the members of my thesis committee: Dr. Todd Lowe, Dr. Walter O'Brien, Dr. Aurelien Borgoltz, and Dr. Clint Dancey. Thank you for your assistance, feedback, and support to this research and thesis. Your perspective and guidance has been invaluable. Your encouragement and help has pushed me to keep working hard and to challenge myself when the task at hand didn't seem feasible.

I am grateful for my friends and colleagues at Virginia Tech at the Turbomachinery and Propulsion Lab: Kevin Hoopes, Caroline Kirk, Justin Bailey, Tony Ferrar, Bill Schneck, Todd Pickering, and Gregg Perley; and at the Vortical Flow and Diagnostics Lab: Dan Cadel, Donnie Brooks, and Tobias Ecker. Working with you has been a pleasure and a privilege. Thank you to each and every one of you for your friendship, for listening to my ideas and questions, for your encouragement, and for your assistance. Kevin, thank you for being patient with PIV and being amazed by it, which encouraged me to work harder at it. Thanks for developing such an amazing tool, without which I would not have much of a thesis! I appreciate you always being willing to help me get data at the airport. Caroline and Justin, I would not have completed my degree when I did without your dedicated, hard work and support. Thank you so much for always being willing to run the engine and to do experiments at crazy hours of the evening. You were always there for me when I needed you the most. Tony, I appreciate your support of this research in making sure I did things the right way, helping me to develop the stress analysis, and in keeping the project organized. Todd, you were always available to support my computer modification needs, which enabled our research for which I thank you. Gregg, I thoroughly enjoyed working with you at the lab. I learned so much from you, from riveting to problem solving and all of our discussions. Thank you for being a teacher and friend. Dan, Donnie, and Tobias, it's been so much fun working with you, sharing an office, and going to SciTech. I appreciate your support and friendship through everything. I'm proud to have worked with such a hard-working and intelligent team and I am sincerely grateful to you all.

To my advisor, Dr. Todd Lowe: Thank you for being willing to take me as an undergraduate researcher. Without that experience I probably wouldn't be completing this work at all. I appreciate your expertise and passion for aerospace engineering, which passion has only grown

in me over the last three years. I cannot express how grateful I am for your encouragement at times when it was exactly what I needed to keep going and work harder to obtain the objective we were after. Thank you for your time and effort to help me in this work, and for your training in helping me become a better technical writer. I hope to as excellent a researcher and person as you.

To my parents, Allan and Nancy Nelson, thank you for helping me to become the person that I am so that I could accomplish things like this thesis work. Thank you for your love and always being interested in my work, and for encouraging me to do my best. Thanks for your support, in all its forms, over the years, and for being the amazing examples that you are. I appreciate the love and support of my brother, Mark, and my sister, Katie. To my wife's parents, Tom and Susan Williams, I am grateful for your encouragement and love over the past few years and for all that you do for our family. To all of my family, thank you.

To my wife, Amanda: This work could not have happened without your love, understanding heart, honesty, and encouragement. You are always there for me to celebrate and suffer with me, to put up with long nights of testing and boring evenings of me doing more work at home, of the ever elusive completion date, and all of the other challenges of being in graduate school with a young family. Thank you for being my best friend, always. I love you.

Finally, to my son, Liam: This research would also have been impossible without you. Once you were a little older I knew I could always count on a smile, a shout for joy, and a big hug when I came home. You and your mom helped me keep things together as we played at home or at the park. You spread joy wherever you are and I am a better person because of you and your mother. Thank you for being who you are and for bringing so much happiness to our family.

All photos by author, 2014.

Table of Contents

List of Figures

List of Tables

Nomenclature

Alphanumeric Symbols

A_L, A_L'	Simplified term #1 for M_z
B_L, B_L'	Simplified term #2 for M_z
C_L	Simplified term #3 for M_z
B	Base length of cross section of beam, *m*
c	Airfoil chord, *m*
C_i	Constants of integration
C_l	Section lift coefficient
ds	Differential distance along curve of integration
E	Young's modulus of elasticity, N/m^2
F(x)	Distribution lift force along beam, *N*
H	Height length of cross section of beam, *m*
I(x)	Moment of inertia, mm^4
L	Beam length, *m*
M_1	Constant
$M_z(x)$	Moment distribution along beam, *Nm*
N_1	Fan speed, actual, *%*
N_1c	Fan speed, corrected, *%*
Pix	Number of pixel
R_1	Constant
R_i	Correlation Coefficient
SD_i	Swirl Directivity of i^{th} ring, *deg.*
SI_i	Swirl intensity of i^{th} ring
SS_i	Swirl sector of i^{th} ring, *deg.*
Δt	Time between image 1 and image 2, *sec.*
Δt_{axisym}	Time between image 1 and image 2 for the axisymmetric jet, *sec.*
T_a	Ambient Temperature, *K*
T_{SL}	Reference Temperature, *K*
u	Spanwise velocity (complex plane), *m/s*
v	Vertical velocity (complex plane) , *m/s*
V	Velocity at point ds along path of integration, *m/s*
u_i	Instantaneous velocity measurement at i^{th} point in time, *m/s*
$\bar{u}_i$	Mean velocity, *m/s*
u_i'	Fluctuating part of velocity at i^{th} point in time, *m/s*
$u'_{1,2,3}$	Normal fluctuating velocity component, *m/s*
U	Velocity, *m/s*
U_{axisym}	Velocity of axisymmetric jet, *m/s*
U_θ	Tangential velocity, *m/s*

U_{TJ}	Velocity of turbojet flow, *m/s*
U_x	Axial velocity, *m/s*
V_{ax}	Axial velocity, *m/s*
V_p	Particle velocity, *m/s*
V_y	Shear force, *N*
W(z)	Complex velocity, *m/s*
W_c	Convection complex velocity, *m/s*
X_{image}	Position of image vortex, *m*
X_{vort}	Position of actual vortex, *m*
Δx_p	Displacement of group of particles, *m*
y	Vertical distance from neutral axis, *m*
z	Position in complex plane, *m*
z_i	Position in complex plane of i^{th} vortex, *m*

Greek Symbols

α	Swirl Angle, *deg.*
Γ	Circulation, mm^2/s
$\delta(.)$	Uncertainty in a given quantity
θ	Angle of a data point, *deg.*
θ_i	Position around i^{th} data ring, *deg*.
P	Density of air, kg/m^3
σ_{xx}	Normal Stress, *N*
τ_{ij}	Reynolds Stress Tensor, m^2/s^2

Abbreviations

AIP	Aerodynamic Interface Plane
AOA	Angle of Attack, *deg*.
AOSS	Angle of Side Slip, *deg.*
BLI	Boundary Layer Ingesting
CCD	Charge Coupled Device
CFS	Corrected Fan Speed, *%*
DEHS	Di-EthylHexyl-Sebacate
DES	Distortion Estimation System
ERA	Environmentally Responsible Aviation
FFF	Fused Filament Fabrication
HARV	High Alpha Research Vehicle
HISTEC	High Stability Engine Control
HWB	Hybrid Wing Body
LDV	Laser Doppler Velocimetry

LTO	Landing Take Off
NO_x	Mono-Nitrogen Oxide
PAO	Poly-alpha-olefin
PR	Peak Ratio
SNR	Signal-to-Noise Ratio
SPIV	Stereoscopic Particle Image Velocimetry
SV	StreamVane
TKE	Turbulent Kinetic Energy
UHB	Ultra High Bypass

1. Introduction

The future of commercial and transport aircraft configuration design is being heavily influenced by environmental concerns and is driven by requirements to simultaneously reduce cumulative airframe noise, fuel burn, and Landing Take Off (LTO) mono-nitrogen oxides (NO_x) emissions. NASA's Environmentally Responsible Aviation (ERA) project seeks to identify and develop the important concepts and technologies that enable the realization of these goals for the N+2 timeframe [1-4]. Technologies under investigation include, among numerous items, the use of ultra high bypass (UHB) engines and a highly integrated engine/airframe hybrid wing body (HWB) configuration (see [1]). The need for these efforts in UHB engines has been motivated by wind tunnel studies of HWB configurations (Gatlin et al. [5]). Therein, an HWB model was placed in the 14- by 22-foot subsonic tunnel at NASA Langley Research Center; its angle of attack (AOA) and angle of side slip (AOSS) were varied along with configuration parameters. For AOA=15.6° and AOSS=6° a vortex formed by the leading edge of the airframe was ingested by the engine, evident by the swirling flow around the nacelle (see [5]). Flow fields generated to simulate the HWB vortex being ingested into the UHB engine are investigated in detail in this thesis.

Another configuration design under the ERA project that would experience inlet distortion is a modified tube and wing design that features aft-mounted turbofan engines on top of the fuselage [6-7]. The traditional, less efficient tube and wing configuration typically hangs turbofan engines from the wings, ensuring uniform flow to the engine inlet. Complicated engine/airframe integration distorts the uniform engine inlet flow for which engines are designed, introducing total pressure distortion and swirl distortion at the engine's aerodynamic interface plane (AIP) and in different stages of the engine.

Total pressure distortion can be caused by extreme inlet geometry, airframe boundary layer ingestion, proximity to the ground, and severe flight maneuvers. For many years total pressure distortion was considered the primary source of engine/airframe incompatibility and has thus been an important topic of research in recent years [8-17]. Swirl distortion is the presence of flow angle non-uniformity in the inlet duct and is characterized by swirl angle (α), the angle between the tangential (U_θ) and axial (U_x) flow velocity, which is counter-clockwise positive

(Figure 1., top). There are several types of swirl distortion as shown in Figure 1, namely bulk swirl, twin swirl, tightly wound vortices, and their combinations.

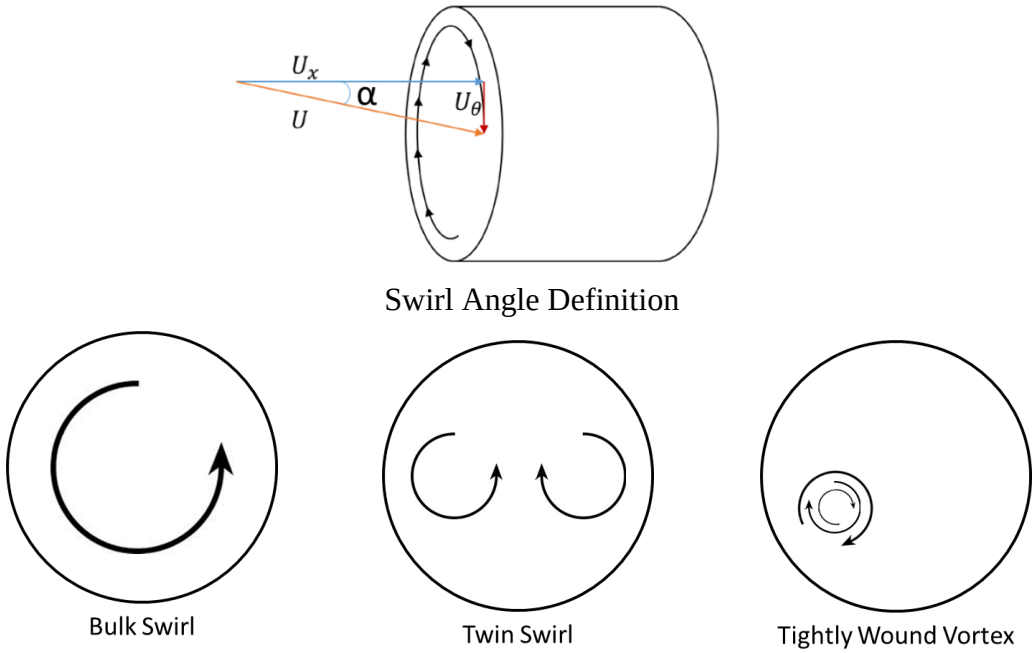

Figure 1. Swirl angle is defined; examples of the three types of swirl distortion are also depicted.

As a rotor blade passes through regions of swirl distortion, the tangential velocity component changes the angle of incidence experienced by the blade which affects the output flow turning angle and the resulting flow past the stator (Fig. 2). These changes from the design condition affect the stage pressure rise, mass flow, work done, and stage efficiency. Strong swirl distortion, coupled with total pressure distortion, can cause flow separation and engine operability issues such as a shifting stall margin, stall, and surge [18]. Swirl distortion has also been linked to high cycle fatigue and other aeroelastic effects as rotor blades continuously pass through regions of highly distorted flow [19-22].

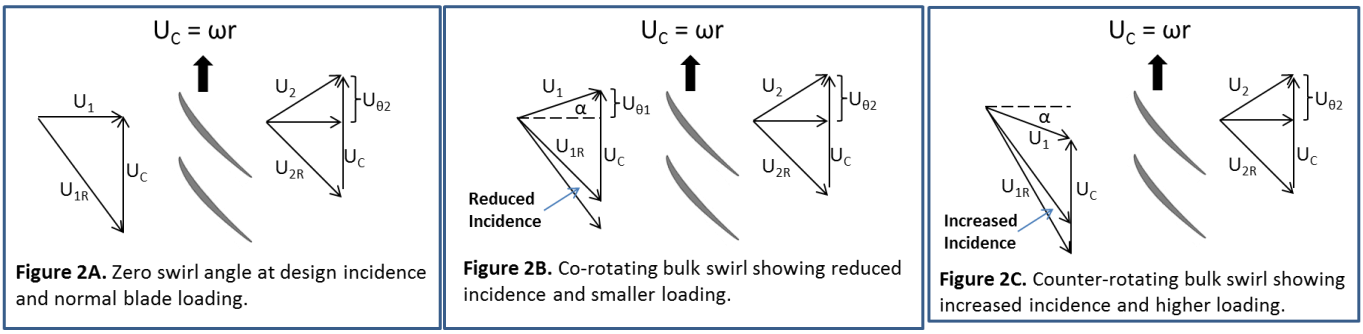

Figure 2. The effect of swirl distortion on rotor incidence.

1.1 Summary of Present Research

Losses and instabilities due to inlet swirl distortion can negatively affect all three of the major aims of the ERA project, as well as overall aircraft safety. An important first step in understanding the effects of a specific inlet swirl distortion on parameters like fan performance and engine operability is to accurately simulate and measure the inlet swirl distortion at the aerodynamic interface plane (AIP) of the engine; the measurement, characterization, and analysis of a real world inlet swirl distortion is the focus of the current work. In the first part of this thesis the experimental setup of both the small scale and full scale test rigs is described as well as efforts to estimate uncertainty that is specific to the full scale inlet distortion test rig. This is followed by experimental results and an explanation of data validation.

1.2 Literature Review

One of the earliest identified cases of airframe/engine compatibility issues was the twin turbofan engine fighter/bomber Tornado aircraft, which underwent prototyping in the mid-1970s. During initial flight testing engine surge occurred at high angles of attack during subsonic flight and during level, supersonic flight in spite of ground testing to determine the effects of total pressure distortion on engine operability. Inlet separation generated bulk counter-swirl due to a thickened boundary layer [18]. A retrofit fence was installed in the inlet to minimize the effects of inlet swirl and the compatibility issues were resolved [18]. This experience brought to light the need to improve ground test procedure to identify and test engines for swirl distortion in addition to total pressure distortion. The challenges of said ground testing include specifically identifying the swirl distortion that the engine will experience for extreme flight conditions, accurately simulating the distortion at the engine's AIP, and measuring the resulting flow field with enough spatial and time resolution to be able to understand how the distortion affects fan and/or compressor performance and overall engine operability. Over the past several decades these ground test challenges have been addressed to varying degrees.

1.2.1 Swirl Generation

A significant challenge in assessing fan response and engine operability in the presence of an inlet distortion is the ability to accurately recreate a three-dimensional velocity vector field at a given plane, the AIP, of an operating jet engine. The goal is to recreate an in-flight condition that

the engine would experience without the required cost and time of manufacturing an aircraft model or prototype. After the experiences of the development of the Tornado aircraft, several methods of swirl generation have been implemented with success in artificially creating generic swirl profiles, including the use of turned vanes [23], a delta wing to generate a vortex pair [23], and a swirl chamber [24-25]. These methods are often difficult to control or adapt and none are able to recreate a complex swirl distortion taken from actual engine/airframe systems.

The most recent efforts have culminated in the invention of the StreamVane (SV) method for inlet swirl distortion generation [26]. This method is able to reproduce specific swirl profiles that are present in real engine/airframe applications and is used to create swirl distortion profiles in the current work. The method is defined by the following steps, as detailed further in [26].

First, a three-dimensional velocity vector field must be specified, typically using CFD, at a given plane (Figure 3). This plane is often chosen to be the AIP, where it is assumed that a duplication of the flow field will result in the same engine response as the real engine/airframe installation. Second, turning vanes are placed everywhere perpendicular to the in-plane velocity vector field with variable vane spacing to best characterize large turning angle gradients and local extrema. Structural supports placed parallel to the flow field provide reinforcement to hold turning vanes in place and to reduce deflection and stress concentration. Third, the geometry of the cross section along each vane line must be chosen in order to achieve the required turning of the flow. In the current work the NACA A_4K_6 camber line [27] is used in combination with a constant thickness profile, chosen for good performance over a large range of output turning angles and easy implementation. Fourth, the vane/support lines and their respective profiles are exported to a CAD package to automatically create solid bodies of the vanes/supports, add a flange for mounting the screen in the inlet distortion test rig, and add a shroud. Finally, additive manufacturing is used to create the swirl distortion screen, enabling the reproduction of complex swirl profiles in both intensity (swirl angle) and pattern (in-plane velocity vector field).

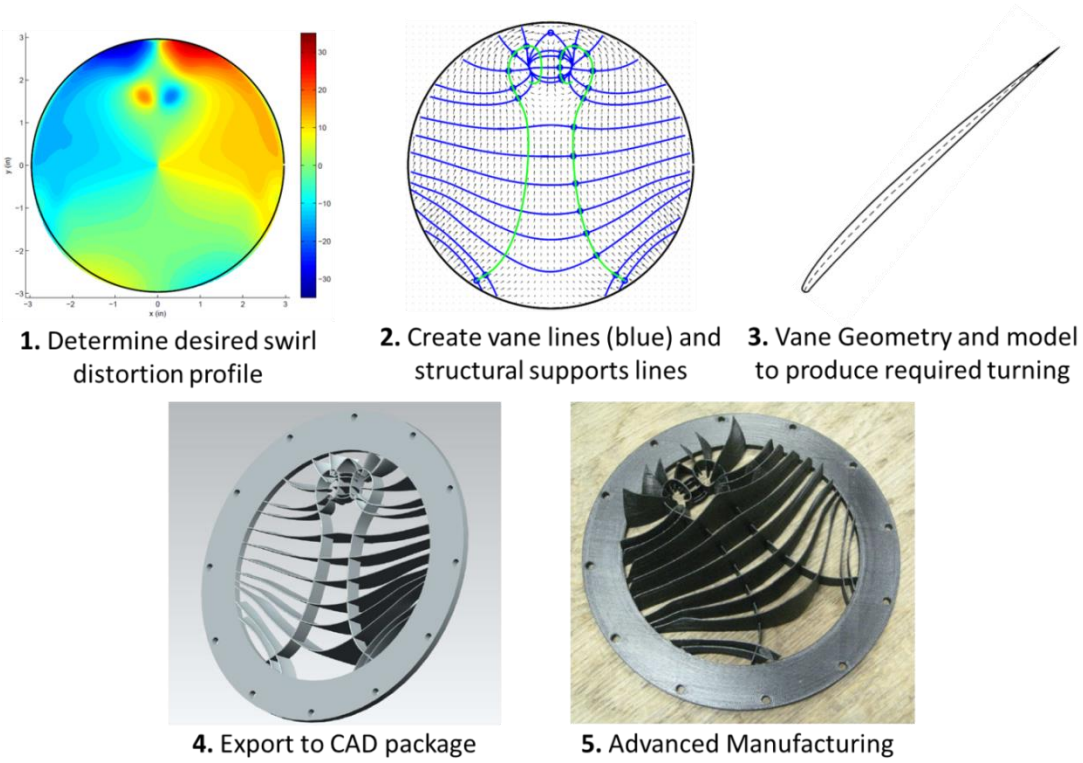

Figure 3. An overview of the StreamVane method is shown as a series of steps, starting from an input swirl distortion profile and ending with a 3D distortion screen.

Reference [26] states a number of recommendations for improvements that can be made to the StreamVane method to advance the method's robustness, performance, and uncertainty. Of these items, a one-dimensional structural analysis of the StreamVane distortion screen, the convection of vortices generated by the screen, and redesign of the turning vane leading edge are addressed in the appendix and represent continued efforts to optimize the inlet swirl distortion screen creation process.

1.2.2 Computational and Experimental Studies on Distortion

With the experience of the Tornado fighter as a catalyst, a great body of work has been completed to create and measure different inlet distortions and their effect on different components of an engine. A majority of the existing, published research focuses on generic total pressure distortions that are created using screens with regions of varying porosity. A few efforts have artificially created swirl distortion in a ground testing environment to determine fan response and engine operability. Another group of work focuses on full scale flight testing that

includes maneuvers that produce both swirl and total pressure distortion, with real time measurement and characterization of the distortion embedded in the engine inlet. This past research has contributed important insights into the study of inlet swirl distortion creation, measurement, and interaction with the engine's fan.

Generic Total Pressure Distortion

There are two related papers done by researchers at the University of Cambridge that computationally study a generic total pressure distortion on a single stage fan. Fidalgo et al. [16] developed a CFD simulation of the transonic fan test rig to demonstrate an accurate simulation and to better understand what is happening between the plane where a distortion is introduced and the fan, as well as the interaction of the distortion with the fan. The inlet distortion is a 120 degree total pressure distortion (DC_{120} of 83%) with the fan at 90% design speed, which corresponds to a mass flow of 32 kg/s. The Rolls-Royce HYDRA CFD solver was used for the simulation. Experimental data [28-31] from the test rig on which the simulation was based was collected by NASA nearly 30 years ago using laser Doppler velocimetry (LDV), static pressure taps, cobra and wedge pressure probes, a total pressure rake, and a total temperature rake. It was found that the fan rotor sucks harder on regions of lower total pressure and, just in front of the rotor, the gradients in the static pressure field induce swirl distortion, which intensifies moving closer to the rotor. The spinner was also found to be a contributor to the generation of swirl distortion in front of the rotor where a non-axisymmetric static pressure field is created. Gunn et al. [17] performed experimental work on a similar low speed test rig using a 5-hole probe and a 60 degree sector of total pressure distortion. No significant swirl was measured at the AIP. Just as with Fidalgo et al., static pressure gradients induced swirl distortion close to the fan rotor, including a 50% increase in mass flow rate in the distorted sector. Where swirl was present, it decreased from hub to tip. The concentrated interest in the topic of swirl distortion generated by a total pressure distortion has been investigated by numerous others who have similar findings.

Representative Total Pressure and Swirl Distortions: Simulated

Aside from generic total pressure distortions, representative swirl profiles have been recreated and measured in sub scale and full scale experiments [see also 32, 33]. Park et al. [34] developed a 2-inch diameter, 3D printed screen that generates a counter-rotating vortex pair. The design was based on Milne-Thompson's circle theorem and the flow physics of Rankine vortices to create turned vanes. Several parameters were varied to obtain the best design; the screens were tested in a blow down wind tunnel driven by a leaf blower using a 7-hole probe to obtain three component velocity measurements. All screen iterations produced a vortex pair with a single iteration chosen as the most effective at recreating the theoretical flow field. The convection of the vortex pair was also studied by making measurements one, three, and five diameters downstream of the screen. While this study doesn't include the influence of the engine's fan and other important systems, the development of a more specific swirl distortion has been demonstrated and measured.

Another effort to create and measure a counter-rotating vortex pair was completed by Pazur et al. [35], who used an inclined delta wing model to create the swirl distortion. The model was traversed and inclined 1.5 fan diameters in front of a two-spool turbofan Larzac 04 engine, which did not have inlet guide vanes. The Larzac 04 has a two stage transonic fan with an inlet diameter of 17.8 inches. Again, 5-hole probes were used to measure the flow field. A stable vortex pair was formed and measured in front of the fan. A swirl distortion representative of a wing tip vortex was created and measured by Mitchell [36] in the Lewis 10- by 10-foot supersonic wind tunnel. A nearly symmetric, tapered wing was mounted to the tunnel wall 8.2 wing tip chord lengths upstream of a 2D, external compression inlet designed for operation at a Mach number of 2.2. The inlet was connected to a J85-GE-13 turbojet engine. A rake of three dimensional flow angularity probes was used to measure the distortion in front of the inlet, primarily to determine the wing position that created the vortex with the largest rotational velocity (found to be an angle of attack of ±11 degrees); these probes had a calibration range of -35 degrees to 35 degrees. By varying the wing angle of attack, both co- and counter-rotating vortices were generated. 2D flow angularity probes and total pressure probes were used at the compressor face to measure the flow field. Measurements showed that from the inlet to the compressor face, the counterclockwise vortex drifted across the compressor face, moving toward

the hub and then away toward the inlet wall. Before entering the inlet, the wing tip induced vortex core diameter was 14% of the wing tip chord length and had a maximum tangential velocity of 51% of the free stream axial velocity. At the compressor face the core had enlarged to 18% wing tip chord length and a maximum tangential velocity of 30% the free stream velocity. Maximum total pressure and static pressure defects of 5% and 3%, respectively, were measured at the compressor face.

Gunn et al. [37], utilizing both the previously mentioned low speed, single stage fan test rig and the CFD computational domain of a transonic research fan, created a total pressure distortion of mild complexity representative of a boundary layer ingesting (BLI) profile using a 3D printed screen of varying porosity. 5-hole measurements were made at five axial locations. Similar results as previously described were obtained, with swirl being induced by gradients in the pressure field and interacting with the spinner, which was replicated in CFD. An important finding was that both the transonic and low speed data exhibited similar fan response to a BLI distortion.

Representative Total Pressure and Swirl Distortions: Flight Test

The final subgroup of related work is that work which did not artificially create a total pressure or swirl inlet distortion, but utilized the full scale airframe with the engine installed and a variety of boundary conditions to create, measure, and analyze an inlet distortion [see also 38-39].

First, and perhaps most prominent, is the development of the F-35B lift fan inlet by Sylvester et al. [19]. Because of strict constraints, the lift fan is highly integrated with the airframe, which included a bellmouth to condition the inlet flow. High bellmouth curvature induced separation due to localized flow acceleration and regions of high total pressure loss were experienced. The primary concern was the identification of excited resonance modes in the lift fan, raising concerns about high cycle fatigue (HCF). The relationship between inlet distortion and high cycle fatigue has also been documented. This occurred in spite of having inlet guide vanes. The magnitude of total pressure distortion was too severe for traditional porous distortion screens, so CFD was used to define an in-flight lift fan aerodynamic stream tube, which was made into a physical inlet distortion generator. While the intent was to generate a specific total pressure distortion, the stream tube device also mimicked the swirl distortion present. After a redesign of

the inlet bellmouth using static pressure ports in extensive wind tunnel testing, six full-scale stream tubes were ground rig tested with the lift fan to determine lift fan operability margins. Relationships were drawn between the subscale wind tunnel tests and the full scale stream tube tests. Further, it was shown that the redesigned inlet reduced inlet pressure distortion by more than 50% for appropriate IGV angles. The research was capped with flight testing of the first F-35 STOVL aircraft, comparing lift fan distortion models developed during the ground test stage to in-flight data.

Walsh et al. [40] detailed flight test data acquired for an F/A-18A High Alpha Research Vehicle (HARV), which contains inlet guide vanes before the three stage fan. Instrumentation on board the aircraft included accelerometers, rate gyros and surface position measurements. Pressure measurements were made at the AIP using a rake of low- and high-frequency-response total pressure probes, which rake was designed to be insensitive to flow angularity; the range of yaw angles was ±25 degrees and the range of pitch angles was -25 to +15 degrees. Static pressure ports were distributed throughout the inlet wall. During the flight test Mach number (0.3 to 0.4), angle of attack (0° to 60°), and angle of side slip (-10° to 10°) were varied. Inlet recovery, turbulence, and circumferential distortion were adversely affected with increasingly negative angle of side slip and increasing angle of attack.

Similar testing was completed by Southwick et al. [41-42] in the high stability engine control (HISTEC) program, whose goal was to obtain in-flight measurements of total pressure distortion in the inlet of an F-15 flight test aircraft with the purpose of enhancing engine stability and the in-flight distortion database. The experimental test flight included a modified production F100-PW-229 inlet case which was instrumented with five high response static pressure measurements, the electrical average of five inner diameter pressure measurements, and four static pressure taps located between struts on the OD and ID inlet case shrouds. This static pressure instrumentation would allow for real time measurements being made in the inlet from which a distortion pattern would be characterized (Distortion Estimation System, DES). A temporal Fourier transform of instantaneous measurements is performed to provide distortion component intensity, which are multiplied by a frequency domain distortion sensitivity function to determine the instantaneous fan/compressor ratio surge margin debit. This debit is communicated to the engine control unit to modify the fan and compressor operating lines to maintain an acceptable stability margin. Additionally, for algorithm validation purposes, an array

of 35 high response total pressure sensors were installed in the leading edges of the inlet guide vanes as well as a total temperature sensor placed at the mid-span of each instrumented inlet guide vane leading edge. The total pressure measurements were used to verify the characterization of distortion from the DES algorithm during in-flight testing; the DES calculation of stability margin debit was within 2% of measurements by the total pressure system, following similar trends in pattern, intensity, and an increasing loss in stability margin with increasing aircraft angle of attack for both steady state angles of attack and an angle of attack sweep. Further flight tests allowed the DES systems data to be used to successfully modify the engine pressure ratio (nozzle exit area) during an aircraft maneuver as desired. While this testing does not quantify or address the effects of swirl distortion on fan performance, engine operability is quantified and controlled successfully for the full turbofan system in the presence of real distortions. The distortion patterns that are published are all relatively simple once-per-rev distortion patterns and are only performed for the right engine.

Advanced flow measurements were made by Schröder et al. [43] using, among other technologies, stereoscopic particle image velocimetry (described in the following section) at the inlet and nozzle of an IAE-V2527 engine mounted to an Airbus A320 MSN 659 inside a sound attenuating hangar. The objective was to develop a measurement database of noise producing regions within the engine, which is generated by large scale, turbulent fluctuations in velocity and density. SPIV was employed to obtain data in the plane normal to the flow just in front of the inlet and parallel to the flow in the shear layer of the exhaust jet. Researchers also attempted to obtain instantaneous measurements of a ground vortex, which forms due to the close proximity of the engine to the hangar floor; they were unsuccessful because of the complexity of the flow field, imaging, and seeding challenges, however, the average flowfield was obtained. Detailed instantaneous 3D flow fields of the turbulent shear layer in the exhaust were obtained in addition to the average. This work highlights many of the challenges present in obtaining acceptable SPIV data for turbine engine inlet flows and emphasizes the need for a controlled testing environment.

1.2.3 Stereoscopic Particle Image Velocimetry Uncertainty

Stereoscopic particle image velocimetry (SPIV) was used at the measurement plane of interest in order to obtain instantaneous planar velocity measurements. SPIV is a noninvasive, planar laser diagnostic technique (Fig. 4) that directly measures flow tracer displacement over a precise increment in time in order to calculate velocity [44]. The flow tracers, commonly termed flow seed or seeding, are small particles with a diameter on the order of one micrometer. Ideally these particles are neutrally buoyant in air and are small enough to follow the trajectory of a local streamline (Stokes number << 1); in practice this is difficult in air and literature exists to address particle lag effects [45, 46]. A dual pulse laser is used to illuminate a planar measurement volume through which the seed particles pass. The circular, Gaussian laser beam existing the laser is passed through a series of lenses to form a sheet of light which is typically a few millimeters thick or smaller. Two digital cameras with a charged-coupled device (CCD) or a CMOS sensor record images of light that is scattered from the seed particles that follow the flow. Another image pair is recorded after a small, known time (for example, several microseconds), allowing the seed particles to displace a small amount. The images are mapped to a common coordinate system and broken down into small interrogation windows. Corresponding interrogation windows are cross-correlated to obtain the displacement of groups of particles. Given four equations for three velocity variables (i.e., simultaneous planar pixel displacements in 2 stereoscopic images), knowing the displacement of particle groups and the time in between image sets, three components of velocity are calculated everywhere seed was present.

In spite of the development of PIV methods and algorithms over its 30 year history, there is no widely accepted framework for reliably quantifying PIV measurement uncertainty, which is an important current field of research [46-48]. Determining PIV uncertainty is very complex because the velocity field is calculated as a result of several successive steps, each of which has its own error sources which cascade through to the end result. The intent of this portion of the paper is not to introduce a new method of global uncertainty quantification, but rather to accept current error analysis for general PIV experiments and to determine and quantify sources of error that are specific to the inlet distortion test rig employed in full scale measurements.

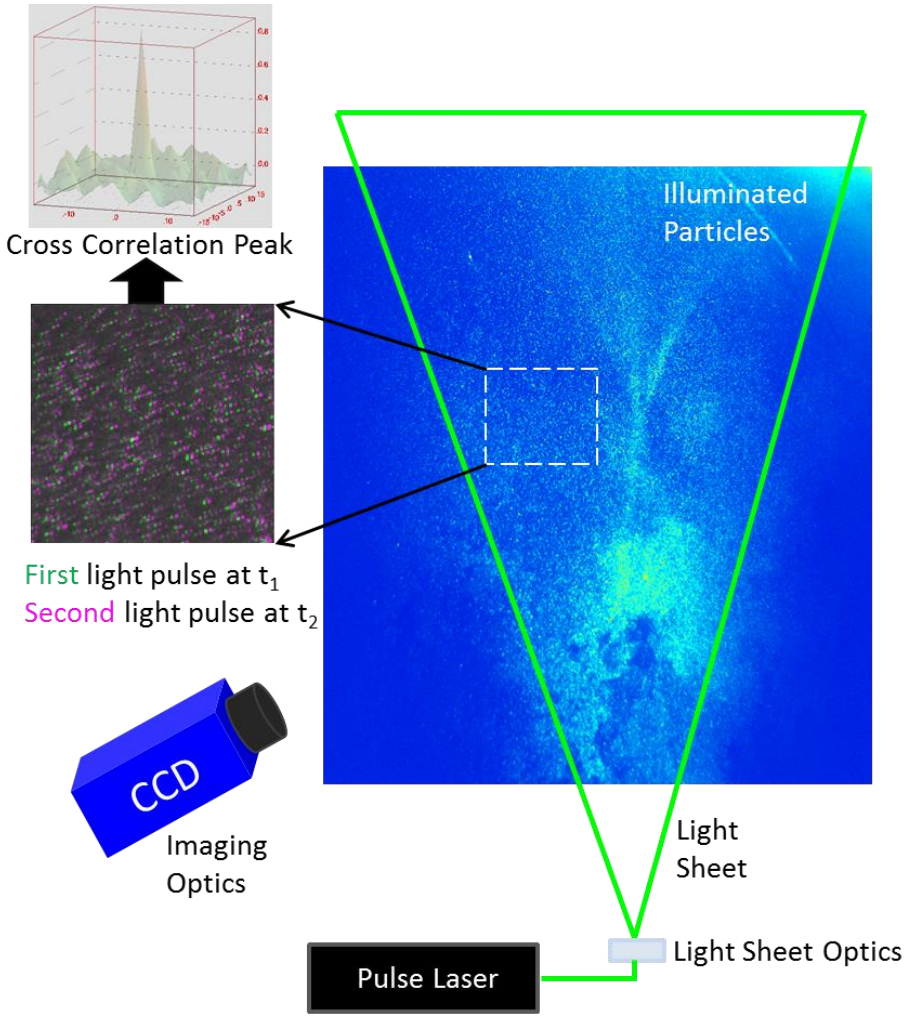

Figure 4. Schematic of a generalized experimental setup for particle image velocimetry (PIV).

Some experimental setups, as the present one, include vibrations which are unavoidably transmitted to the CCD cameras used to record images and to the optics that position the laser sheet. These vibrations cause the cameras to move relative to the measurement plane and relative to one another. The laser sheet can also potentially move relative to the measurement plane and the cameras. The cameras are calibrated such that each is registered to a common coordinate system; small changes in camera or laser sheet position during data acquisition will create bias registration errors in each measurement. The apparatus of the present work includes an operating turbofan jet engine which causes this relative motion. This topic has not been widely addressed in current literature, though some solutions have been successful.

In a dissertation by Jacobs [49] a non-reinforced camera mount was vibrating during testing with an RMS displacement of 7.52 pixels. Camera displacement was determined by plotting the surface of the test article, an airfoil, for all sample images. Reinforcement of the camera mount reduced this value to 0.62 pixels, which was deemed acceptable without any further analysis of the related PIV uncertainty.

Bian et al. [50] both identified camera movement through image processing and corrected for the bias error in post processing. To identify camera movement, a stationary wall was chosen as a reference and a vertical line of pixel intensity was extracted from each image, which region experiences a peak in light intensity. A third order Gaussian function was fit to the pixel intensity data to find the peak; the change in peak location indicated movement of the camera, which displacement was plotted with the transverse velocity component. This showed a coupling between the camera movement and the velocity component. To correct for the error, velocity fluctuations were subtracted on a frame-by-frame basis. The uncertainty due specifically to camera movement was not cited, however, since they were virtually eliminated. For reference purposes, the overall uncertainty was found to be ±6% for the streamwise velocity component and ±10% for the vertical velocity component. The laser sheet was aligned with the streamwise velocity.

LaVision's Davis 8 software [51] has a built in feature that computes a cross correlation between a single interrogation window of user defined size in a reference image to the same interrogation window in each image of the data set. Both translation and rotation of the camera can be accounted for. The bias is then applied to each individual image. This feature can effectively be used when, like the work in Bian et al., there is consistency in light intensity of the reference objects.

The movement of the laser sheet relative to the calibration/measurement plane is also a significant concern; its effect is coupled with the error due to relative motion of the cameras. Several researchers have addressed the importance of correcting for misalignment of the laser sheet. Beresh et al. [52] found the errors in mean velocities were small, while turbulent stresses were reduced because of this error. Additionally, a misalignment of one vector spacing resulted in an error of 5% to 15% of the turbulent stress. Doorne et al. [53] determined that, for an experimental setup with large out-of-plane motion, an error of 1% of the centerline velocity

would require a misalignment of 0.1mm or less. Beresh et al. [52] applied a self calibration to reduce the laser sheet alignment error in turbulent stress by 20%.

1.3 Relationship of Present Research to Other Methods

The present research seeks to build upon the previous work done in the field of ground testing of swirl distortion generation and measurement. Previous work has focused on total pressure distortions in front of a single stage fan test rig or a full scale turbofan engine. This knowledge has added to the understanding of how a fan responds to a distortion, which indeed includes swirl distortion directly in front of the rotor. Very little work has been done to address swirl distortion present not just directly in front of the rotor, but further upstream at the AIP. Ultimately it is under investigation to understand the relationship between the measured total pressure field, the swirl angle field, and engine fan response in the presence of distorted flow. Sylvester et al. [19] have successfully used stream tubes to recreate both a total pressure field and swirl field at the AIP, but no swirl data was presented. The lift fan on the F-35B is a very non-traditional inlet and represents an extreme case.

This work seeks to add to the database and understanding of inlet swirl distortion by full scale, full system validation of the artificial generation of a realistic swirl distortion induced by airframe/engine system interactions. It is important to include the entire system of the turbofan engine (inlet, fan, compressor, combustor, turbine, nozzle, etc.) in order to more completely understand the influence of a distortion on fan response and even overall engine performance; the realization of configuration benefits of these highly integrated airframe/engine designs depends on a clear picture of these important issues. A good place to start is to generate, measure, and characterize an appropriate distortion. This thesis lays the ground work, from sub scale to full scale, of validation and performance of the StreamVane method, including three dimensional time averaged velocity fields, swirl angle, Reynolds stress, and turbulent kinetic energy. The validation of the method will give confidence to future work on the investigation of the effects of fundamental, arbitrary swirl distortion from real airframe/engine systems on fan response and engine operability.

2. Apparatus and Instrumentation

The work for this research was divided into two major groups, 1) the design and construction of a suitable turbofan inlet flow distortion generator and 2) the design and implementation of appropriate instrumentation to measure the distorted flow at the engine inlet. The StreamVane method, as described in §1.2.1, addressed the goal of generating an arbitrary inlet flow distortion. The development and maturing of the StreamVane method was completed in a small scale wind tunnel using particle image velocimetry (PIV) and a five-hole probe. A full scale test rig was then designed and built for the full scale testing of StreamVane screens. The experimental setup and instrumentation for both experiments is herein described, as well as efforts to estimate the uncertainty in PIV measurements—uncertainties specific to the inlet distortion test rig.

2.1 PIV Instrumentation

For all experiments, the following SPIV equipment was used to obtain instantaneous velocity measurements. Images were illuminated with a dual pulse 532nm Nd:YAG laser (New Wave Research Solo 200XT) rated at 200mJ/pulse that operates at up to 15Hz. The laser beams are round, roughly Gaussian, and overlap one another. Two LaVision Imager ProX CCD cameras, each with a resolution of 2048x2048 pixels and a 24mm prime Nikon lens, were used to record images. Each camera lens has an f-stop range of 2.8 to 22. In between the lens and the camera sensor is a Scheimpflug adapter to correct for the variable depth focusing required by the oblique viewing angle of the stereoscopic setup. The cameras are synchronized with each other and the laser and are mounted on metal rails. The laser sheet is formed using a -10mm or -20mm focal length cylindrical lens to expand the width of the sheet and a 500mm focal length spherical lens to focus the thickness of the sheet to 1-2mm at the center of the measurement volume. A LaVision laser delivery arm is used to position the initial laser beam above the test section. The beam passes through the two sheet-forming lenses at the end of the arm. The seed particles used are an atomized oil (used both DEHS and PAO) with an expected mean particle diameter of 0.5 to 1 micron. Images were recorded, calibrated, and cross-correlated initially using LaVision's DaVis 7.2 software; an update to DaVis 8 was obtained before the final data was acquired. Further post-processing was done in MATLAB.

2.2 Small Scale Experimental Setup: StreamVane Development

In order to validate the StreamVane method, several scaled down tests were completed as a proof of concept. A wind tunnel consisting of a large blower followed by a settling chamber, flow straightening screens, and contraction to a 12-inch by 12-inch square section with a square-to-circle adapter was used to generate flow through a 6-inch inner diameter pipe designed to simulate the engine inlet. At typical run speeds of 50 m/s the facility achieves a similar Mach number as the full scale engine tests when run at idle throttle conditions. The pipe was split into two sections, with a plastic screenholder sandwiched between the pipes. The swirl distortion screen, printed out of ABS plastic using the Fused Filament Fabrication (FFF) technique, was bolted inside the screen holder (Figures 5, 6).

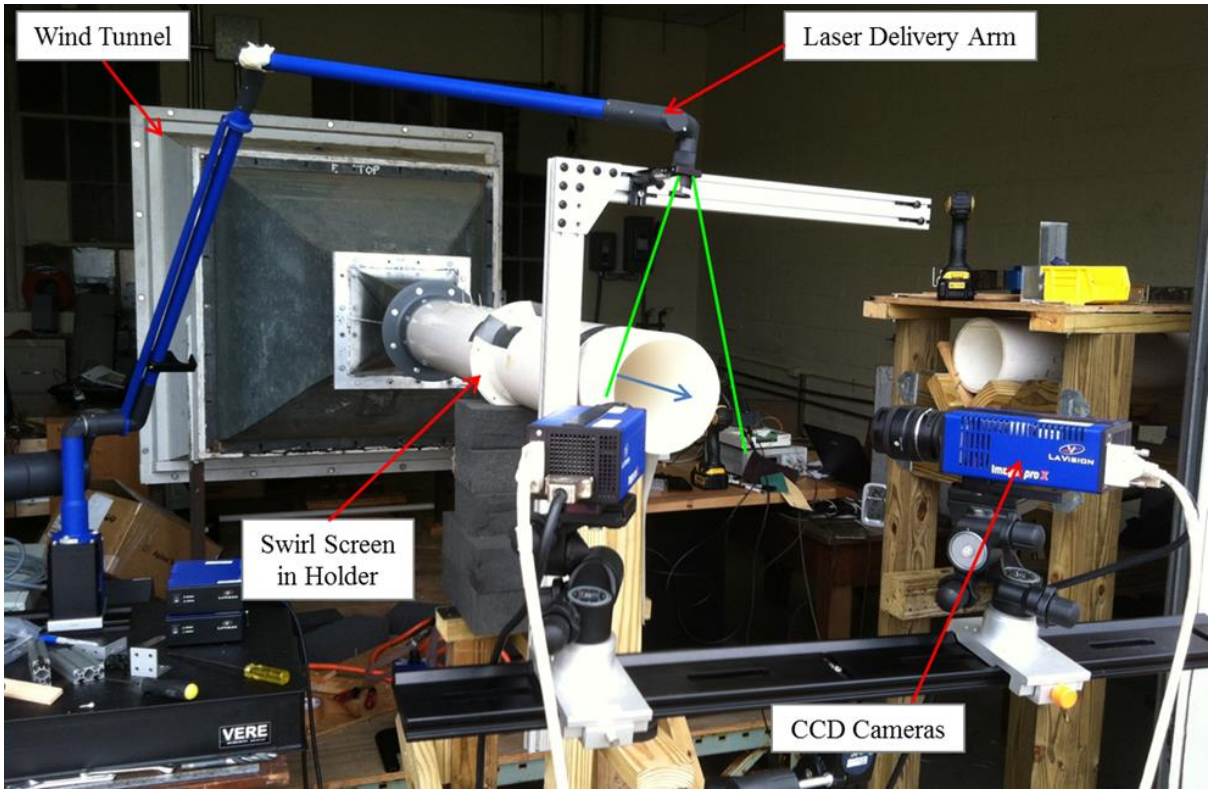

Figure 5. Image of the sub scale test apparatus stereoscopic PIV setup.

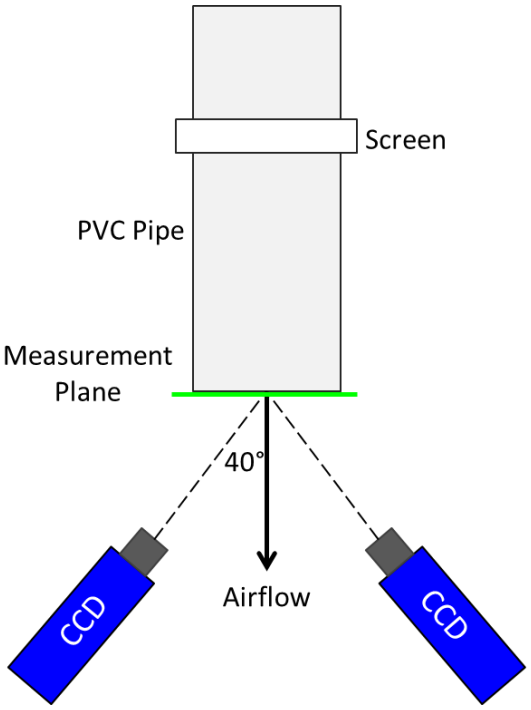

Figure 6. A top view diagram of the sub scale experiment.

2.2.1 PIV

The measurement plane is the plane normal to the flow at the exit of the pipe, which is one diameter downstream from the swirl distortion screen. The cameras (f-stop 2.8) were positioned on a metal rail that was mounted to a tripod downstream of the pipe exit at oblique angles of approximately 40 degrees relative to the pipe centerline. A LaVision seeder containing 4 pneumatic nozzles was used to atomize seed from di-ethylhexyl-sebacate (DEHS) oil. Seed was introduced upstream of the swirl screen on the suction side of the wind tunnel, mounted on a metal grating. In this manner seed could mix sufficiently and be evenly distributed before being illuminated. For SPIV results from a StreamVane screen in this tunnel, see §4.1. The end and interior of the pipe was spray painted flat black (not shown) to minimize laser glare and to better resolve the seed particles near the wall.

2.2.2 Five-Hole Probe

As the StreamVane method progressed, the SPIV system was not available and a five-hole probe was used for further small scale measurements; these probe measurements are presented for comparison purposes only with full scale data. The screenholder previously

mentioned was made with an external gear so that the screen could be rotated by a stepper motor. A linear traverse was placed one diameter downstream at the measurement plane such that, when combined with the screen rotator, a probe can be positioned at any two-dimensional location within a quarter inch of the tunnel wall. For more information see [26].

2.3 Full Scale Inlet Distortion Test Rig

Stereoscopic PIV measurements of swirl inlet distortion in front of an operating turbofan jet engine were completed on a full scale research turbofan engine based upon the Pratt & Whitney Canada (P&WC) JT15D-1 turbofan engine. This low bypass engine is designed for smaller, business class aircraft. Table 1 presents a summary of the design and performance specifications of the JT15D-1.

Table 1. P&WC JT15D-1 Design Specifications

Parameter	**Value**
Fan 100% RPM	16,000
Engine Mass Flow [lb_m/s]	73
Bypass Ratio	3.3
Fan Pressure Ratio	1.5
Compressor Pressure Ratio	8
Fan Diameter [in.]	21
Thrust (SL, Takeoff) [lb_f]	2,200
TSFC (SL, Takeoff) [$lb_m/s/lb_f$]	0.54

The general design of the experimental rig has been used extensively by the Turbomachinery and Propulsion Research Lab at Virginia Tech to measure the effects of total pressure distortion on fan response [54]. The current test rig, pictured in Figures 7 through 9, is comprised of an inlet, a seed distribution device, a distortion screen, a tunnel section with optical access, smooth tunnel sections to connect the subsystems together, and the research engine, which is mounted to a test stand. Each tunnel section is one fan diameter long and is constructed using twenty gauge aluminum sheet metal which is rolled to a twenty one inch diameter circle and riveted together

(countersunk in the gas path) with circular flanges for bolting sections together. Each tunnel section is further reinforced with L-channel brackets.

The optical tunnel section contains four windows – two for camera access and two for laser entry/dump. This tunnel section mounts directly to the engine fan flange. Optically clear, cast acrylic is compressed between layers of sheet metal and bolted in place using nut plates, which are riveted to the thin tunnel wall. Weather stripping acts as a gasket to provide a seal. Because the tunnel wall is so thin (0.032") and not perfectly circular, it was difficult to mount windows that were flush with the tunnel inside surface. As a result, a cavity with a depth of approximately 1/16" is present where each window is, resulting in secondary flow as the air recirculates near the edges of the window. Though it was not possible to obtain data near the wall due to window flare from the laser, any data that would be collected near the wall is suspect until a smoother optical access can be implemented. The cameras and windows were covered with a black cloth during testing to reduce glare on the windows. Additionally, because the experiment is located in a test cell that is open to the environment, testing was performed after sunset to minimize light saturation in the second time exposure of image pairs. The interior of the test rig was spray painted flat black to minimize glare and laser reflections that can compromise SPIV images, though glare from the laser dump window was problematic. The two CCD cameras were mounted to a metal rail that was bolted to an aluminum frame designed to minimize the movement of the CCD cameras and laser sheet relative to the test rig (see Fig. 8). The cameras were oriented at oblique angles of approximately 37 degrees relative to the test rig centerline, looking upstream and away from the fan face. By directing the cameras toward the oncoming seed particles (forward scatter orientation), the amount of imaged scattered light is maximized.

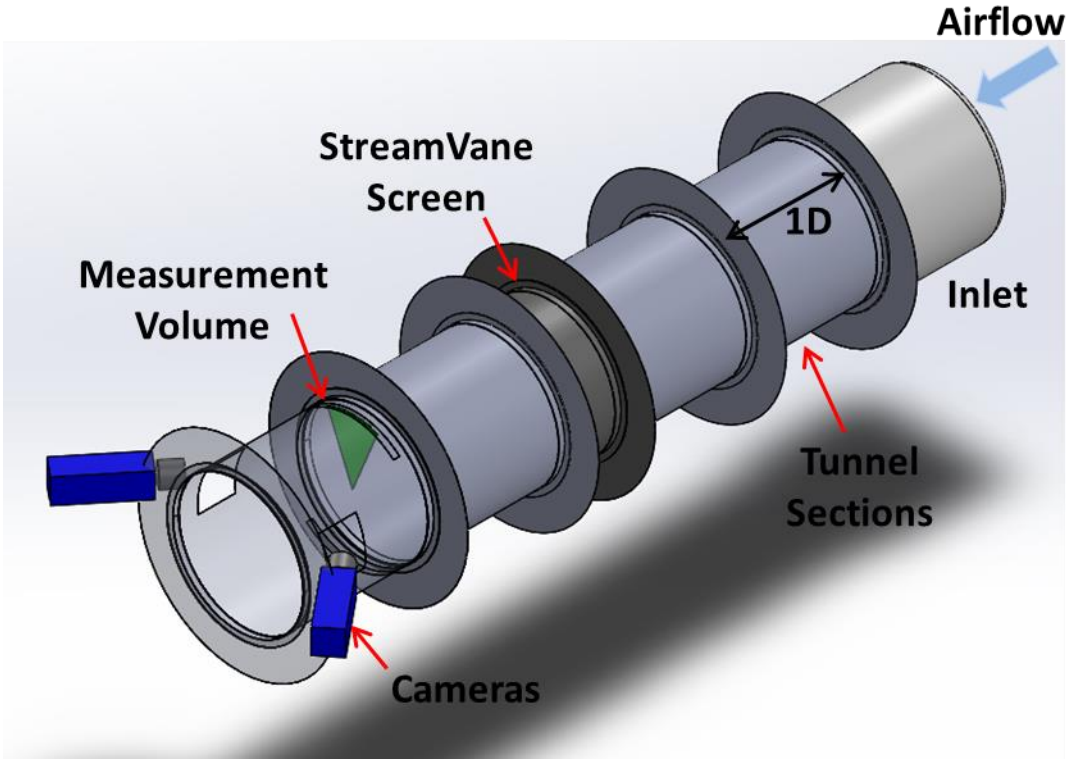

Figure 7. A schematic of the full scale inlet distortion test rig. The measurement volume (green) is one fan diameter upstream of the fan and one diameter downstream of the distortion screen.

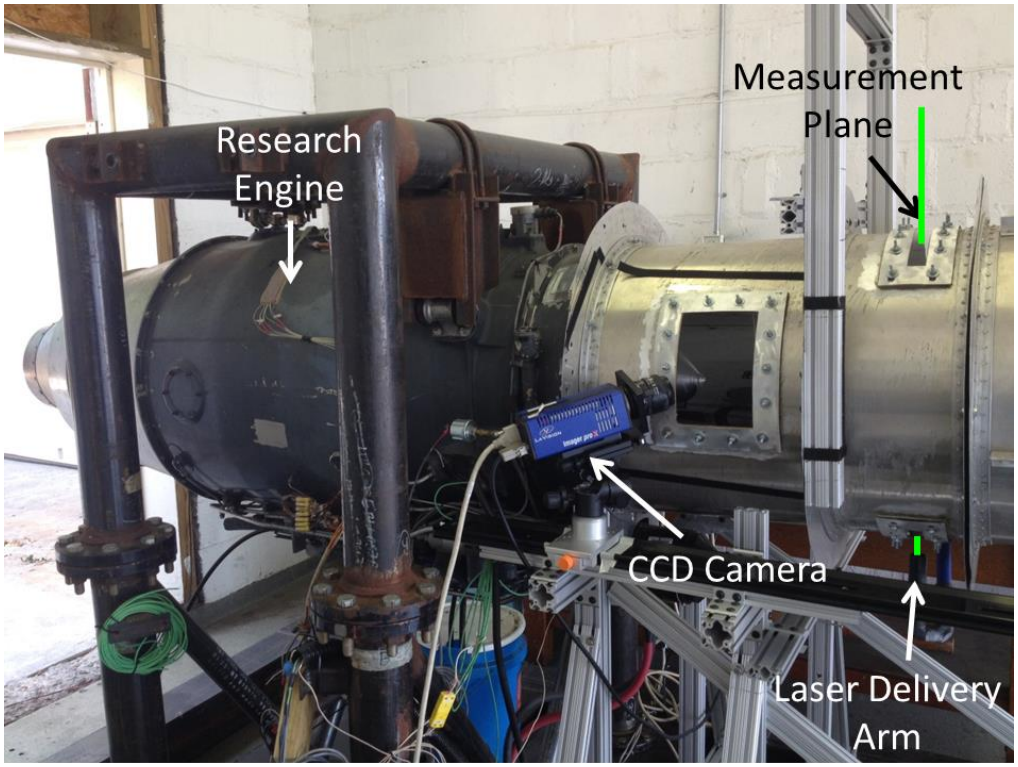

Figure 8. The measurement portion of the inlet distortion test rig is imaged.

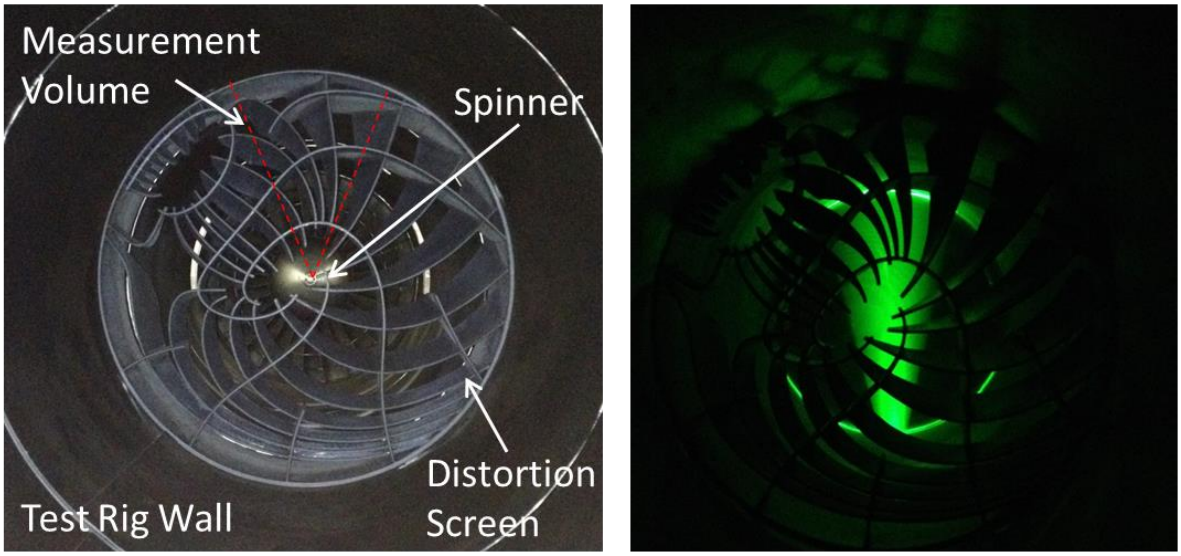

HWB StreamVane Screen in the Inlet Distortion Test Rig

Measurement Volume Illuminated by the Pulse Laser

Figure 9. The StreamVane distortion screen (left) is shown inside the test rig, with the interior of the tunnel painted flat black to reduce laser glare. The measurement volume is illuminated on the right.

The three-component velocity vector field was measured at the AIP, defined as one fan diameter upstream from the fan face, in order to provide information applicable to realistic airframe/engine installation scenarios. Measurements were acquired in a 45 degree sector (Fig. 9), the size of which was driven by several factors. Seeding the test rig was very challenging as discussed in the following section and particle seeding requirements were minimized. The circular nature of the test section prevented a wide field of view being used due to the edges of the measurement volume being cut off, as well as optical distortion effects. A smaller measurement volume would require a smaller window for optical access, which would not disrupt the test rig's boundary layer as much. Finally, it was desirable to concentrate the laser intensity in a smaller region to obtain a better raw image with lower signal-to-noise ratio given the difficult seeding arrangement. During data acquisition, images were captured with the inlet distortion screen in the vertical position; the screen was initially rotated every 45 degrees and images taken again, repeating the process until the entire distortion cross-section has been measured. For the full scale StreamVane data, the distortion screen was rotated every 22.5

degrees to obtain a 50% data overlap. Because the screen was rotated by hand, the engine was spun down and powered off between measurements such that each measurement in independent of the rest. In order for each run to be comparable, the fan speed was corrected for changes in atmospheric conditions, according to equation 1. After cross-correlating and post-processing each set of images, the resulting vector fields are rotated and spliced together.

$$N_1 = N_{1C}\sqrt{\frac{T_a}{T_{SL}}} \qquad (1)$$

where N_1 is the actual fan speed, N_{1C} is the corrected fan speed, T_a is the ambient temperature, and T_{SL} is the sea level temperature.

It has been observed that the research turbofan engine employed in this work operates in a steady manner and free of operability issues in the range of power settings from idle (36% uncorrected fan speed) to 80% corrected fan speed. The data presented in this thesis were made with a distortion at both engine power settings for the total pressure distortion screen, and at 50% corrected fan speed for the StreamVane distortion screen. The range of the clean, axial flow velocity for these power settings is 45m/s (idle), 67m/s (50% cfs), and 120m/s (80% cfs) with corresponding Mach numbers of 0.130, 0.193, 0.346, respectively (Fig. 10).

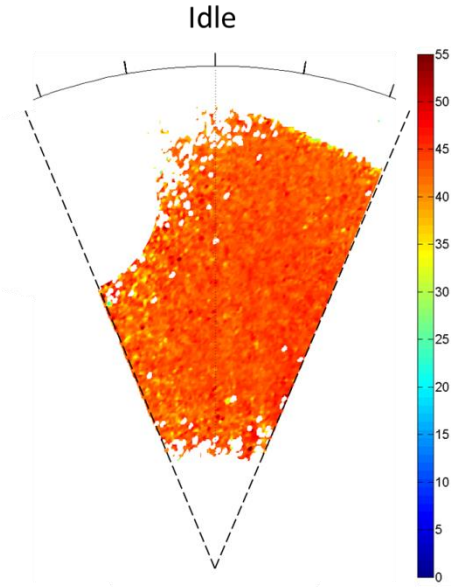

Figure 10. Undistorted axial velocity for idle and 80% corrected fan speeds, measured at the AIP. Regions are whitened due to poor seeding.

2.3.1 Seeding the Full Scale Test Rig

Particle seeding is a major concern in the current application due to the complexity of the distorted flow and challenges of seeding in full scale applications. The seeder used for full scale testing is a pressure vessel that atomizes poly-alpha-olefin (PAO) oil through an array of twelve Laskin nozzles arranged symmetrically around a center feedpipe, producing large quantities of polydisperse liquid aerosol with an average particle diameter of 1 micron. A smoke generator (ViCount Compact 5000) was also used to test seeding methods, but was not used for any presented data.

Because of the importance of seeding a complex flow, the author felt it significant to include what was both successful and unsuccessful. To address the issue, several methods of seeding the flow were tested with the goal of achieving a uniform seed distribution throughout the image. Nine methods were tested: (A) Three stainless steel tubes (~3/8" ID) perforated with 7/16" diameter holes spaced 1/2" apart, mounted to an aluminum ring, injecting seed particles in the airflow upstream of the swirl distortion screen. These tubes are positioned circumferentially at -11.25°, 0°, and 11.25°, where 0° is the top center of the duct, to ensure uniform seed distribution throughout the 45° sector, assuming symmetric and even spreading and mixing of the jets of aerosol ejecting from the holes; (B) The seeder was placed 7.5 feet and 11 feet in front of the engine with a 3/8" ID L-shaped plastic tube to direct the seed cloud toward the engine; (C) The seeder was placed at the same locations as (B) without any ducting, ejecting a vertical plume of seed; (D) The seeding bar assembly described in (A) was removed placed 11 feet in front of the engine; (E) The seed was ducted through 2" PVC pipe to the centerline of the tunnel, 61.5" in front of the inlet plane; (F) Seed was ducted through 2" PVC pipe to a location on the floor of the test cell at the centerline of the tunnel, 24.5" in front of the inlet; (G) Seed was ducted through 2" PVC pipe to a location above the tunnel line with the inlet plane at the center of the tunnel; (H) A smoke generator was placed in the right corner of the test cell in the front entrance plane and was ejected as a free jet toward the inlet; (I) Two seeders were used, each in combination with a leaf blower to direct the seed and diffuse it so as to enhance mixing and encourage a more uniform and consistent distribution. All configurations are shown in Figure 11 and listed in Table 2. Test images with six Laskin nozzles were performed for all cases at two different throttle settings, idle and 80% corrected fan speed to determine which method achieved the highest performance as previously defined.

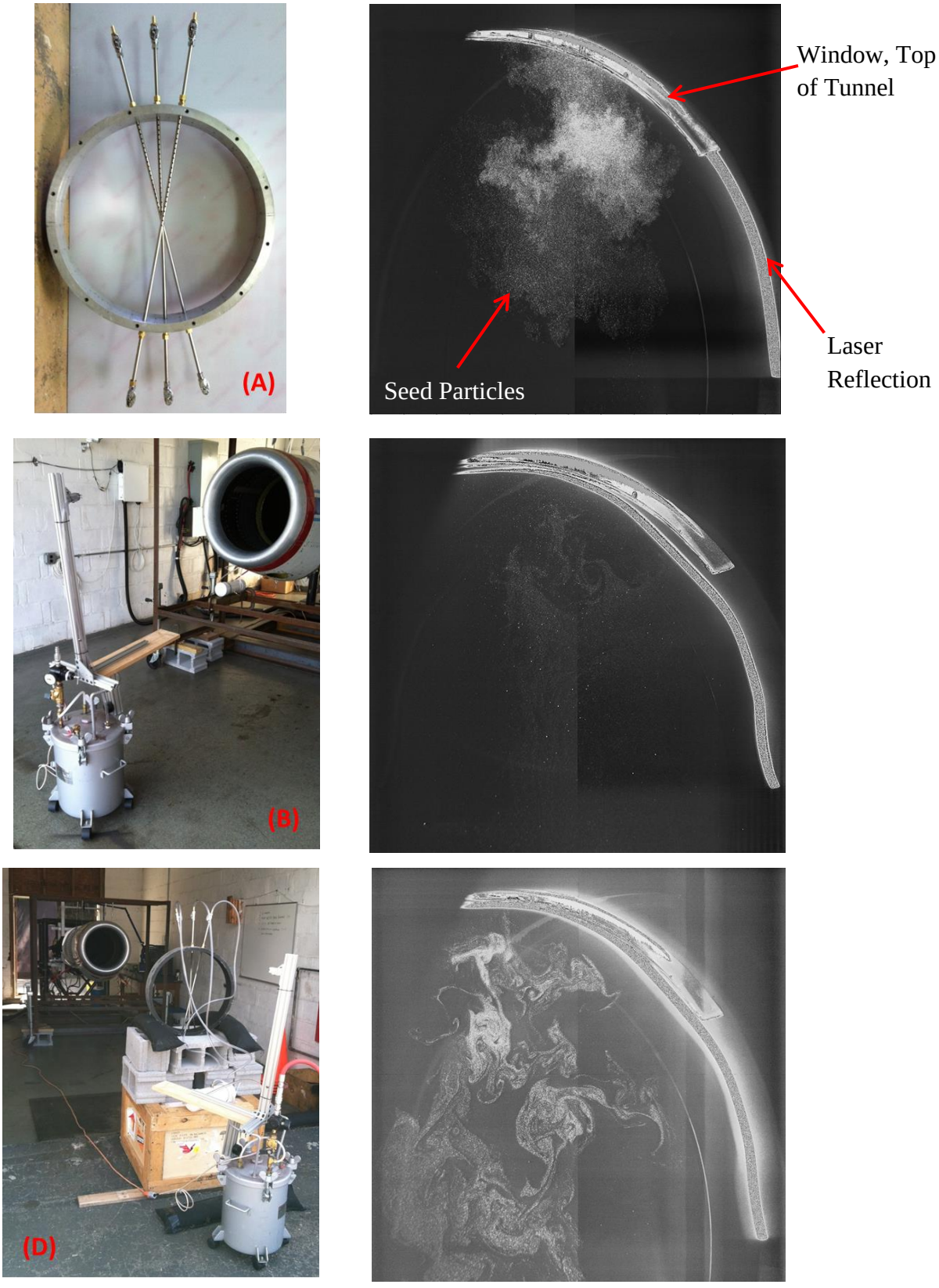

Figure 11. Numerous different methods of seeding the flow were attempted. Methods A through D are depicted above. All seed images are from the perspective of camera 1, first time exposure.

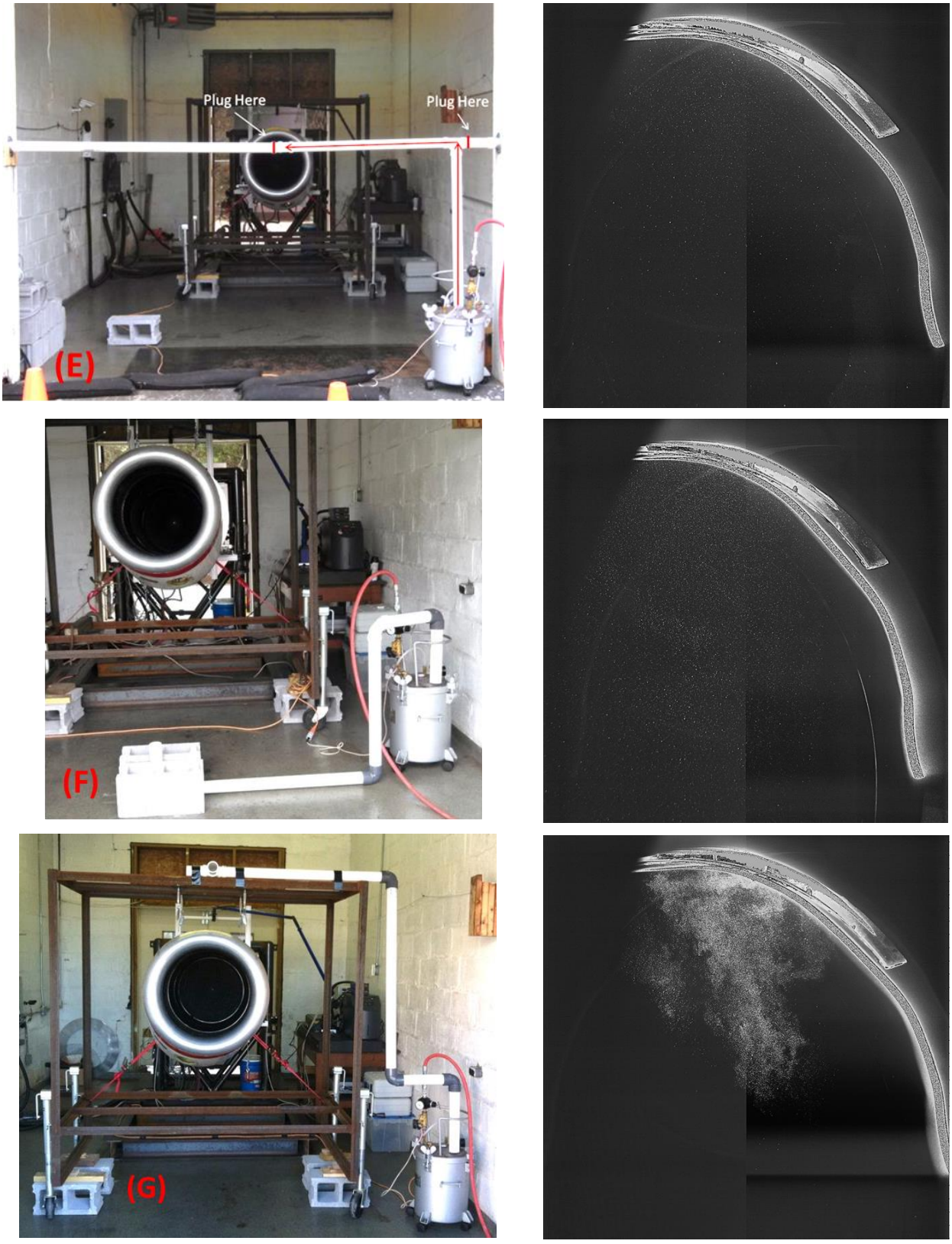

Figure 11. Continued. Seeding methods E through G.

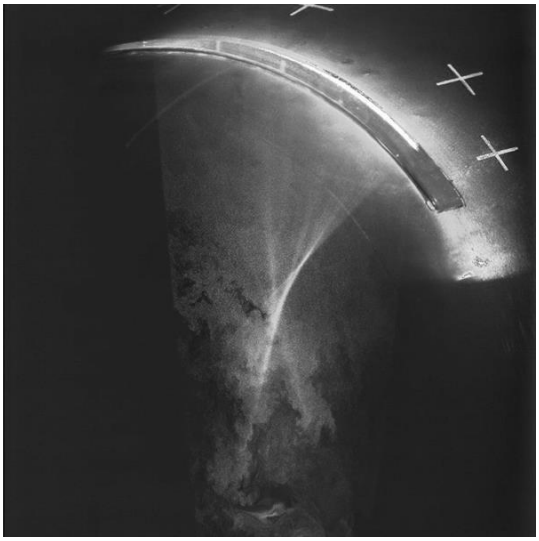

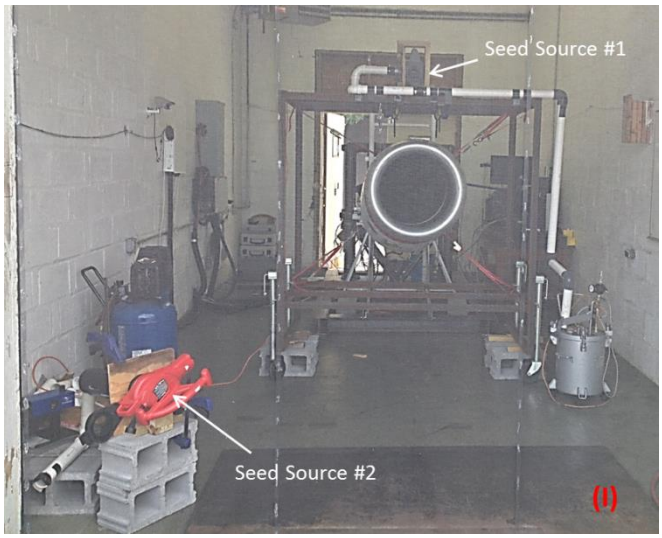

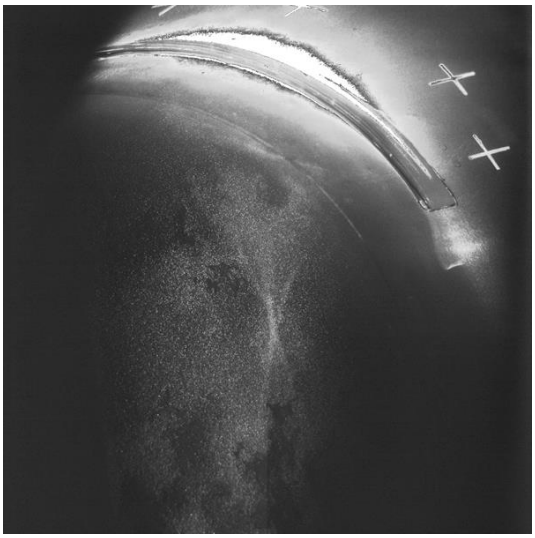

Figure 11. Continued. Methods H and I are shown. These images were taken with a slightly different laser sheet configuration; the laser sheet originated from the bottom of the tunnel and went up. The bright spot in the middle is a refocusing of laser light due to the circular reflective surface (window). “Plus” marks were included to aid in vibration analysis. The previous images had the laser sheet oriented from the top down.

Table 2. Nine different seeding methods were tested with a goal of consistent, uniform seeding at the measurement volume. Results varied. Method I has performed the best to date.

Method	Configuration
A	Laskin nozzle seeder; three seeding tubes with perforated holes, interior to tunnel
B	Laskin nozzle seeder; ducted (3/8" ID), in front of engine
C	Laskin nozzle seeder; unducted, in front of engine
D	Laskin nozzle seeder; seeding tube apparatus, in front of the engine
E	Laskin nozzle seeder; ducted (2" PVC) to engine center line, test cell entrance
F	Laskin nozzle seeder; ducted (2" PVC) to location on floor, 2 feet in front of inlet
G	Laskin nozzle seeder; ducted (2" PVC) to location above the inlet
H	Smoke Generator; free jet, ducted (2" PVC), and blower in test cell corner
I	Laskin nozzle seeder, LaVision pneumatic nozzles; combined with blowers

Method (A) achieved the stated goal, however, it also strongly altered the natural flow in the test rig by introducing wakes (pressure loss, flow distortion) from the cylindrical tubes, which was undesirable. The remaining methods were external to the test rig, allowing for natural flow. A consequence of the test rig being in a test cell was the presence of a ground vortex that formed due to the close proximity of the engine inlet with the floor and walls of the test cell [55]. Methods (B) through (G) all experienced a similar phenomenon. The ground vortex entrained a majority of the seed, generating regions of very dense seed in the images. Quality PIV results require seed to be present where velocity components are desired and an appropriate seed density, neither of which were occurring at the quality desired. The Turbomachinery and Propulsion Research Lab at Virginia Tech has often used a uniform porosity, wire mesh screen for obtaining baseline, undistorted test conditions [54]. This screen was placed in the test rig one diameter upstream from the measurement plane, the seeding methods (sans methods A through D; it was realized that methods B through D were, to some extent, blocking the system's stream tube and the methods were rejected) were repeated, and the effects of the ground vortex were mitigated. Method G was initially chosen as the best option because of consistent, relatively uniform seed density where seed is present at both throttle settings. Because the seed cloud is ejected above the tunnel, it is ingested by the engine in the top-middle region of the inlet, in the exact region of the measurement volume.

Method G was used for the total pressure screen data. While acceptable results were produced, methods H and I represent continued efforts to improve the quality of seed distribution and density in the raw images, which improve the quality of cross-correlated processing and reduce the amount of post-processing required to extract relevant information. Method H gave the desired seed uniformity, however, the seed density was excessive and too much scattered light was recorded by the CCD cameras. The mean particle diameter for the smoke generator is 0.3 microns, three times smaller than the Laskin nozzle seeder. This made it exceptionally difficult to bring individual particles into focus without having access to the cameras during data acquisition. Method I produced above average seeding quality with particles that were in focus. Glare from the laser dump window overwhelmed the signal present in the top of the measurement volume. This problem is being remedied with windows that have an anti-reflective coating; also being considered is the use of a fluorescent paint applied to the inside the optical tunnel section instead of flat black. The paint absorbs the green laser light (wavelength 532nm) and remits the light at a higher wavelength. The cameras are equipped with narrow band-pass filters that are designed to allow green laser light through, filtering the reflected light [56]. This issue is independent of the seed configuration. Method I was used for the full scale StreamVane distortion data, and performed well enough to be used for all future testing.

As an additional note, methods H and I were also conducted with the entrance to the test cell covered in a turbulence screen, which is standard porosity (16-per-inch) window screen. Five pieces were used to cover the 10-foot by 10-foot opening and were connected using hot glue. The screen, to some extent, conditions the flow entering the test cell, providing for repeatable higher quality seeding results. A portion of the screen can be seen in Fig. 11I.

2.4 Inlet Swirl Distortion Characterization and Generation

In order to allow comparison of swirl distortion of varying shape and magnitude in different inlet systems, the S-16 Turbine Engine Inlet Flow Distortion Committee has recommended as industry standard several non-dimensional parameters named swirl descriptors which are detailed in SAE AIR-5686 [18]. These parameters include swirl angle, sector swirl, swirl intensity, and swirl directivity, which are sampled at different radial rings in the flowfield. The mathematical definition of each is given in the following equations. Swirl angle, α_i, is the flow angularity due to the circumferential velocity component, directly affecting the angle of incidence on the first

stage fan rotor. Sector swirl, SS_i, quantifies the average co- or counter-rotating swirl content for the i[th] ring. Swirl intensity, SI_i, quantifies the average absolute swirl angle for each ring and the swirl directivity, SD_i, identifies both the general direction of swirl with respect to the fan rotation and the general pattern of swirl distortion.

$$\alpha(\theta)_i = \tan^{-1}\left(\frac{U_\theta}{U_x}\right) \tag{2}$$

$$SS_i{}^{+,-} = \frac{1}{\theta_i{}^{+,-}} \int_{\theta_i{}^{+,-}} \alpha(\theta)_i d\theta \tag{3}$$

$$SI_i = \frac{SS_i{}^{+} \cdot \theta_i{}^{+} + |SS_i{}^{-}| \cdot \theta_i{}^{-}}{360} \tag{4}$$

$$SD_i = \frac{SS_i{}^{+} \cdot \theta_i{}^{+} + SS_i{}^{-} \cdot \theta_i{}^{-}}{SS_i{}^{+} \cdot \theta_i{}^{+} + |SS_i{}^{-}| \cdot \theta_i{}^{-}} \tag{5}$$

The angular position around the i[th] ring is defined as θ. The circumferential distortion extent for positive and negative swirl angle are θ^+ and θ^-, respectively. The parameters will be calculated and plotted as a function of radius and will primarily be used to compare analytical and experimental data.

In addition to swirl distortion, total pressure distortion was also investigated in the full scale test rig in order to identify any basic relationships between the two types of inlet distortion. The traditional nondimensional parameters for total pressure distortion will not be used because comparisons are not being drawn.

2.4.1 Boundary Layer Ingesting Profile

Initial swirl distortion testing was conducted using the NASA Inlet-A swirl distortion profile [57, 58], which is representative of a distortion that a boundary layer ingesting engine would experience. Such a configuration features engine inlets that are partially embedded in the rear fuselage on top of the aircraft via a serpentine inlet, ingesting 30% of the boundary layer [57] that forms on the top surface of the fuselage. This has benefits such as reduced drag, but the fan experiences severely distorted flow due to the S-duct nature of BLI inlet. The profile (Figure 12) includes a pair of tightly wound, counter-rotating vortices and maximum swirl angle magnitudes of 15 degrees.

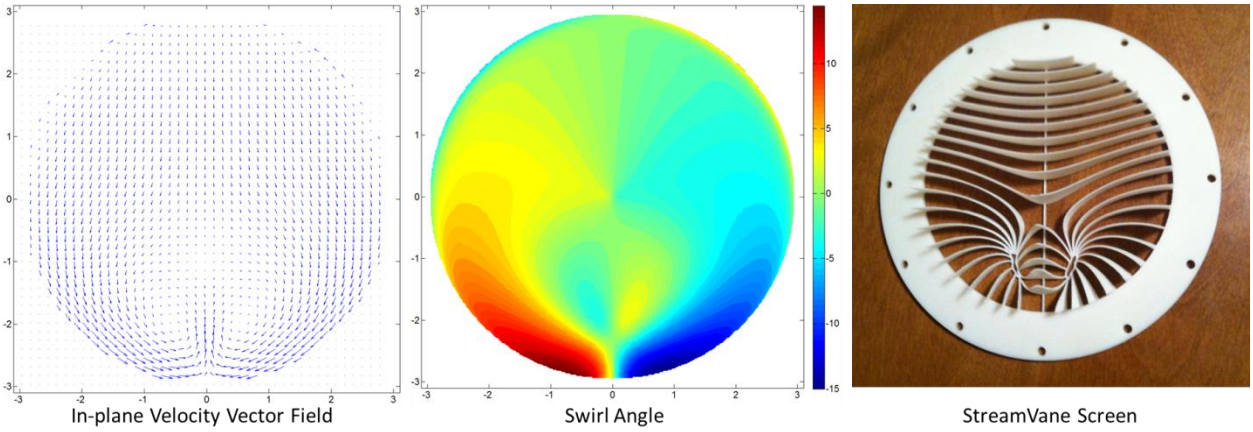

Figure 12. The desired velocity field (left) and swirl angle profile (center) of the NASA Inlet-A swirl inlet distortion profile are made into a distortion screen (right) using the StreamVane method.

CFD was performed to estimate the distortion profile at the AIP of an engine, which is used as the input for the StreamVane method. Given this input, five different radii are sampled and the swirl angle is plotted in Figure 13 for concentric circles at the stated radii. The top half of the profile shows swirl angles of five degrees or less. The bottom half of the profile exhibits a sinusoidal pattern of swirl angle consistent with twin swirl where flow is moving with the rotor in some regions while opposing it in others.

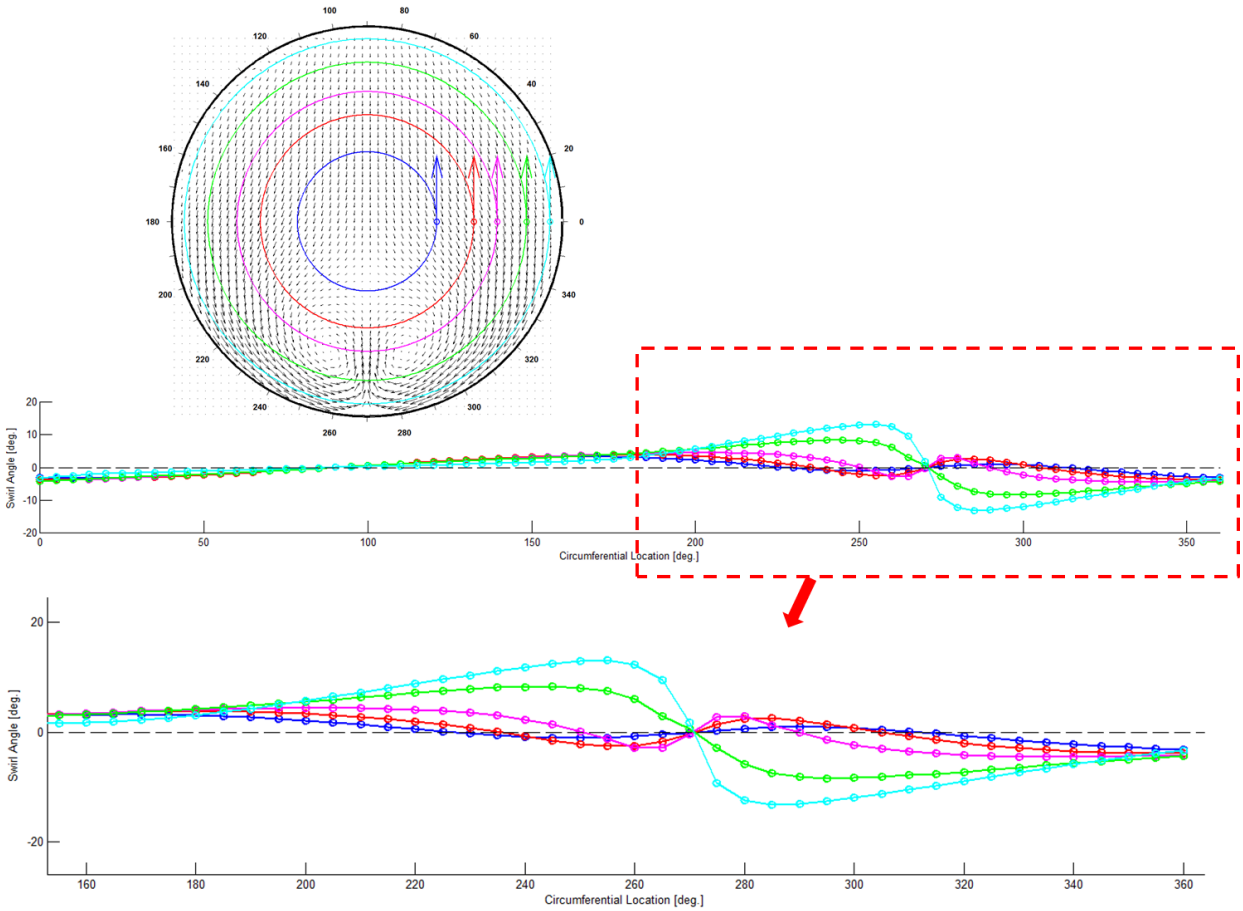

Figure 13. The swirl angle profile was sampled at various radii. A twin swirl pattern is evident.

The distortion profile was made into a six-inch diameter, ABS plastic screen (Fig. 12) using the StreamVane method (see §1.2.1) for use in small scale experimentation. Turning vanes are of uniform thickness of 0.0394" with a structural support running the vertical length of the screen. A flange is added for mounting in the small scale tunnel. This particular screen was made early on in the development of the StreamVane method and is representative of a distortion of medium complexity.

In order to test and validate SPIV instrumentation in the full scale test rig a simple total pressure distortion screen was made which was designed to replicate the total pressure field that is consistent with the same BLI profile of NASA's Inlet-A. This profile exhibits a once-per-revolution low total pressure region in the bottom center of fan face. A backing screen made of 0.5" stainless steel wire mesh with a porosity of 86.1 was used to straighten regions of undistorted flow and was used as a base for finer layers of stainless steel wire mesh, each layer having a porosity of 77.5. Four layers of the finer mesh were used as shown in Figure 14, which

layers were secured together with dental floss and a thin application of hot glue. The overall porosity in each region of layers was not determined.

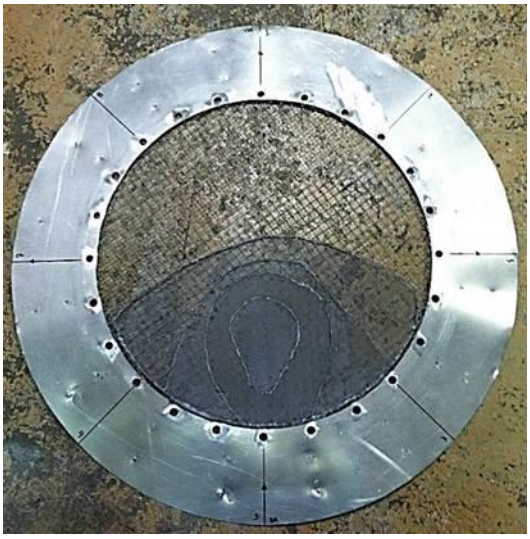

Figure 14. The wire mesh total pressure screen used to simulate a BLI type inlet distortion. The diameter of the mesh region is 21 inches. Note that the screen layering is not symmetric.

2.4.2 Hybrid Wing Body Swirl Profile and StreamVane Screen

As described in the introduction and §4.2.2, the hybrid wing body aircraft configuration is being investigated by NASA for the Environmentally Responsible Aviation project. An important concern in the design of this configuration is the production of large scale, streamwise vortices by the body of the aircraft that are ingested by the engines and the response of the engines' fans to the distortion. In order to obtain a more detailed picture of what is happening in the engine inlet, Boeing Research and Technology has performed CFD studies of the flow produced by the HWB aircraft. Using CFD, a swirl profile was calculated at the nacelle inlet of an advanced HWB configuration in simulated, extreme flight conditions (Figure 15). It is important because it is representative of the swirl distortion present in a real inlet system.

This profile is characterized by a counter-clockwise vortex with a radius of the nacelle with an offset center of 0.664" and 1.08" in the negative x- and y-directions, respectively (for a diameter of 21 inches). A tightly wound vortex is located at 180° at is 2.3" from the nacelle wall. The interaction of the vortices creates a saddle point between their cores and regions of intense swirl distortion with swirl angles ranging from -54.24 degrees to 33.95 degrees. It should be

noted that the bulk swirl is not a true vortex and has significant regions of radial flow, hence the much lower swirl angle in the bottom portion of the profile.

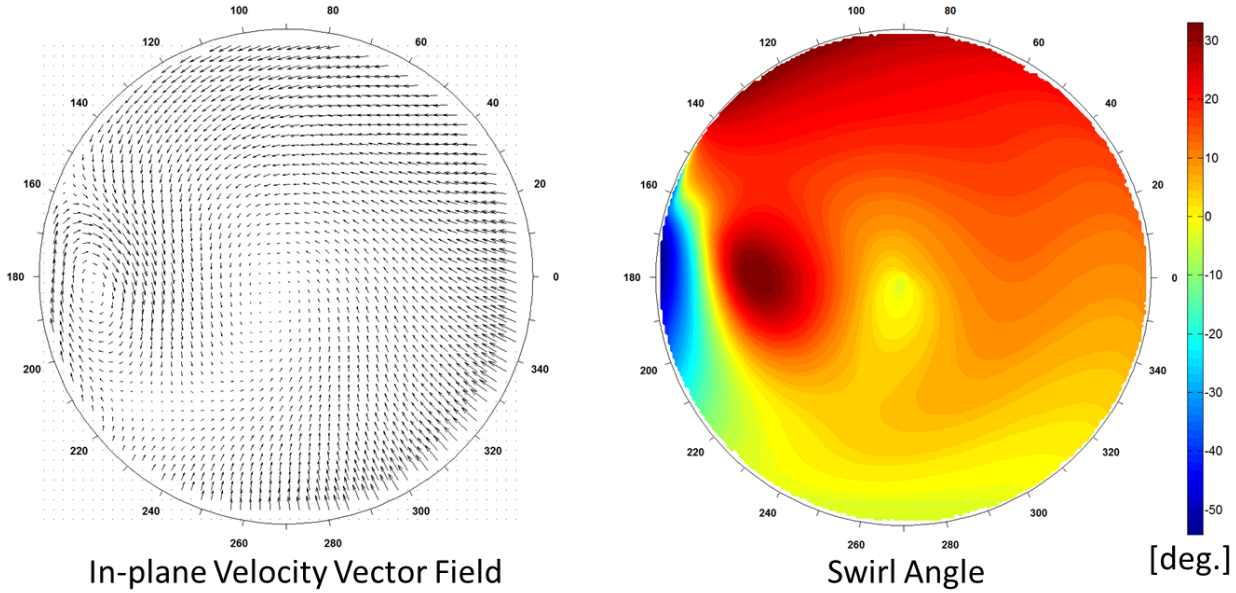

Figure 15. The velocity vector field and resulting swirl angle profile for the hybrid wing body aircraft. Swirl angle ranges from -56° to +34°.

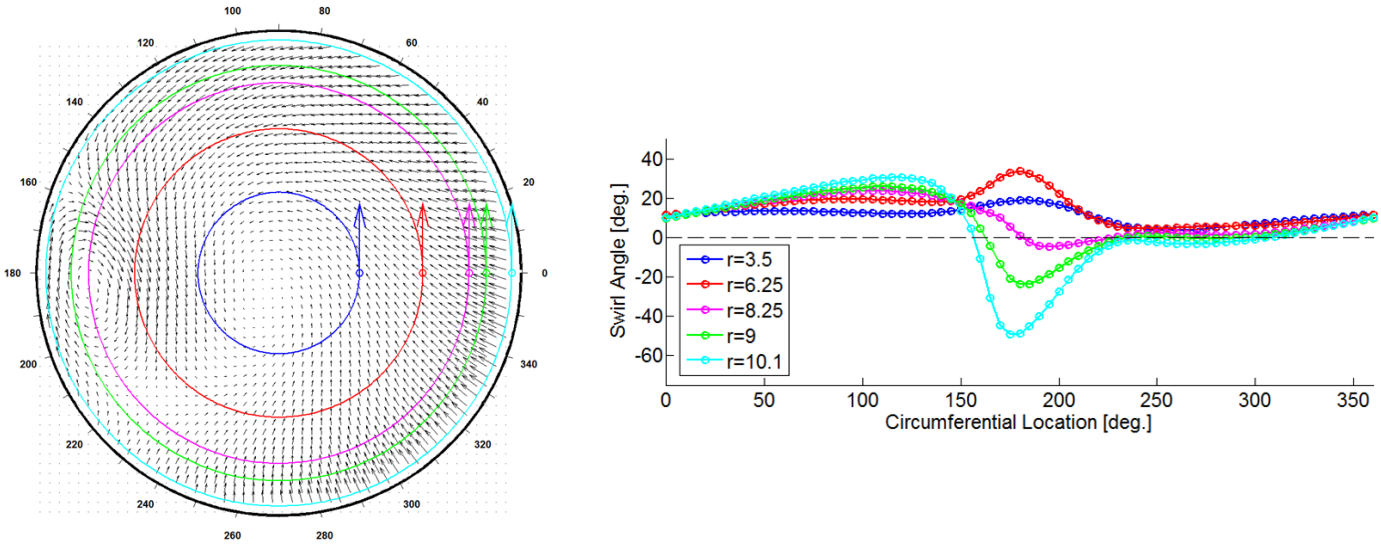

Figure 16. Rings of swirl angle are plotted for the given radii. The highest magnitude swirl is confined to the region of theta = 180°. Significant radial flow is evident in the fourth quadrant.

Five different radii are sampled and the swirl angle is plotted in Figure 16 for concentric circles at the stated radii. Inner rings of swirl angle show purely positive swirl; moving outward, strong regions of negative swirl are encountered due to the tightly wound vortex rotating against the fan direction.

This inlet swirl profile is very complex both in pattern and intensity and represents the most severe inlet distortion conditions calculated during CFD simulations. These swirl descriptors will be revisited in the results section to compare the experimental and computational swirl profiles.

The StreamVane screen for the HWB profile is shown in Figure 10. Many aerodynamic and efficiency improvements were made to the SV method since the screen in §2.4.1 was made, the final details of which are given in [26]. More recent improvements to the method, including the consideration of vortex convection, stress analysis, and CAD model generation are elaborated on in the appendix. The screen is fully shrouded (1/8" wall thickness) to maintain the boundary conditions of a fixed end beam for each turning vane, to reduce the amount of deflection a vane experiences, thus maintaining the desired amount of turning, and to facilitate smooth rotation of the screen in the test rig. The shroud is chamfered at its trailing edge to smoothly transition back to the duct wall, having a trailing edge thickness of 0.3mm and a diffusion angle of 8 degrees. The leading edge of the turning vanes is offset by 0.25" from the upstream flange face to place a fillet at all vane/structure intersections. Each vane section has a flat plate profile with a thickness of 0.138" except for the leading edge, which is elliptical with a major semi-axis of 0.25" and a minor semi-axis of half the vane thickness. The screen was printed as a single piece out of ULTEM* 9085, a high strength-to-weight ratio thermoplastic chosen for having the highest tensile strength [59] of plastic materials available for additive manufacturing. The screen was not made of metal because of size restrictions that prevented printing the screen as a single piece in any metal materials.

3. Uncertainty Analysis

Typical primary sources for PIV uncertainty measurements include shear, displacement, seeding density, particle diameter, system calibration, timing errors, and the optical setup, as well as other systematic and random sources [44]. It has been shown [44, 48] that observed PIV accuracy in most experiments is 0.1 pixels. While the quantification of PIV uncertainty measurement can be very complex, the author seeks to identify and estimate sources of uncertainty that are specific to the inlet distortion test rig. First, the uncertainty of measurement repeatability will be addressed, followed by analysis of a major contributing factor to PIV uncertainty that is specific to the inlet distortion test rig.

3.1 Uncertainty of Measurement Repeatability

The uncertainty of measurement repeatability is calculated at 95% confidence by applying a student t-distribution to the data being compared. When acquiring data the screen was rotated by hand, which necessitated shutdown of the turbofan engine in between data sets. Because of this, each data set is independent. The top three data sets (Fig. 17) in the distortion profile are very similar, most clearly seen in the axial velocity component, and are treated as being nearly identical. This assumption does not hold in the half of the data set closest to the center because of asymmetry and influence from the applied distortion. Repeatability was calculated by finding the standard deviation, σ, of the three data points at each point in the plane of data, multiplying sigma by 4.303 (2 DOF, 95% confidence), and normalizing it on the average profile velocity (~135m/s) to obtain uncertainty percentages for the measurements.

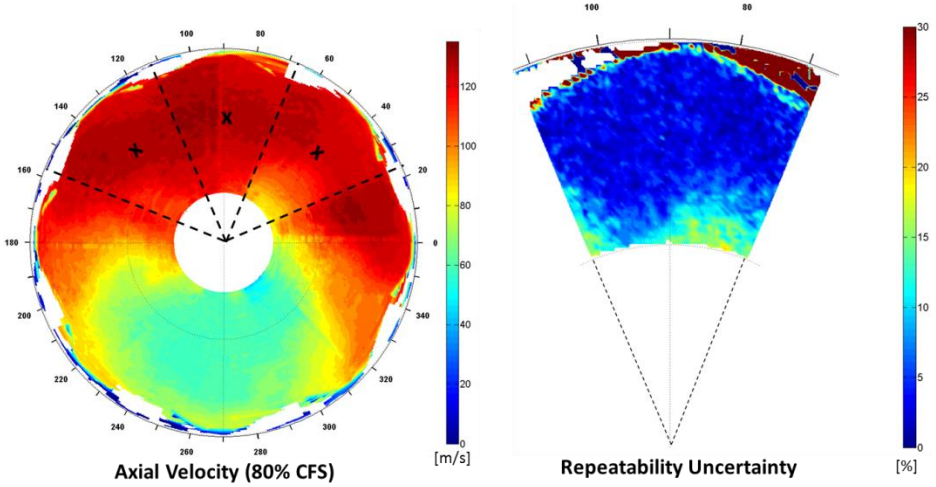

Figure 17. Uncertainty of measurement repeatability is calculated at 95% confidence using the indicated three data sets (left), resulting in an uncertainty less than or equal to 5%.

In regions of quality data the repeatability uncertainty is approximately 5% or less (Fig. 17). In regions where spurious vectors are dominant, this uncertainty is higher and will be resolved by collecting more comparable data, which can further reduce this uncertainty by a factor of nearly 2. The quality of global seed density in the set of raw images from which this was calculated could also be improved.

3.2 Uncertainty SPIV Measurements in due to Relative Motion of CCD Cameras

There are many potential sources of error that are not captured in the repeatability that was previously examined, including unsteadiness through the test cell, cross winds through the test cell, ground vortices ingested by the test rig that introduce secondary flow, imperfections in the test rig manufacturing that influence the boundary layer, intermittent seeding, misalignment of the measurement volume with the machine axis, and the influence of rig vibrations, which cause a small displacement of the cameras relative to the test rig. Most of these error sources are very difficult to quantify, and others have been addressed in past research. In the current work the alignment of the measurement volume with the machine axis was achieved with a level. The levelness of the calibration plate was compared to the levelness of the test rig; this levelness was comparable. To ensure that the plate was normal to the machine axis, the distance from the front edge of the plate to a fixed surface was measured on the far sides of the plate and was made equal. Small misalignments in the yaw or pitch direction will have a varying effect on the measured flowfield, depending on the size and importance of secondary flow. For the measurements of the profile representative of a hybrid wing body configuration, the secondary flow is the same order of magnitude as the axial flow such that small misalignments will not significantly affect what is measured. The alignment of the laser sheet with the calibration plate has been widely studied [52,53] and has important uncertainty implications. To achieve this alignment, the calibration plate was fixed in place and the laser sheet was positioned using an optical post and thin sheet metal shims. While boundary layer measurements in the test rig were beyond the scope of this research, the influence of the test rig on boundary layer growth and general boundary layer growth along the test rig wall are expected to have a negligible effect on measurements, which is of even less concern given the fact that laser glare prevented PIV measurements close to the wall.

Of the described uncertainty sources previously mentioned, the influence of rig vibrations was chosen to further estimate its contribution to overall uncertainty because it most strongly affects the measurement of displacement of particles. In an attempt to mitigate this phenomenon, the cameras were initially mounted directly to the test rig via t-slotted extruded aluminum and are thus subject to the same vibrations that the turbofan jet engine transmits to the test rig; however, some relative motion still occurs. Once the initial analysis was completed and the severity of the bias error realized, the configuration was updated such that the cameras were mounted to the skid of the test stand to try and reduce the transmitted vibrations even more, with success. The following analysis applies to the more extreme case where the cameras and laser sheet optics are mounted directly to the distortion test rig, which is still an important consideration for other extreme testing environments. While these small displacements have a negligible effect on the mean flow field, higher order statistics such as Reynolds stress can suffer from larger errors if not corrected for.

The displacement for each camera was determined as a function of time (Fig. 18) by using MATLAB's built-in function "imregtform" to perform image registry. A reference image is taken when the engine is off and without any seed, the state of the system just after calibrating the cameras.

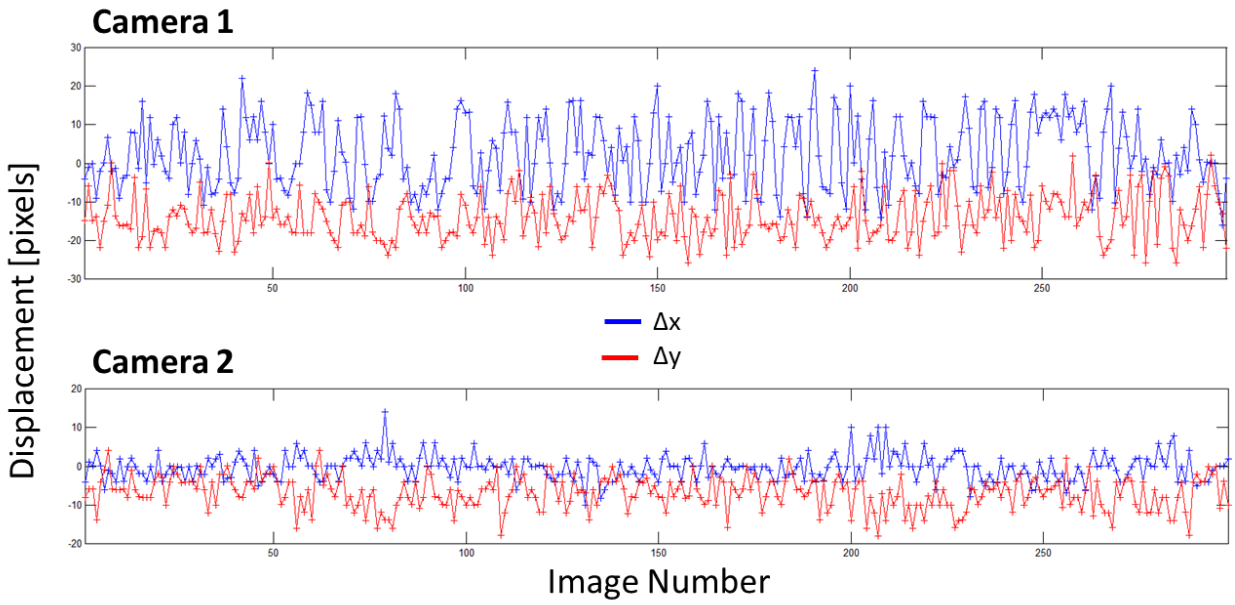

Figure 18. Displacement of both cameras in the x- and y-directions is found via image registration in MATLAB. There are larger displacements in the x-direction for camera 1. The sample size is 300 images.

Each raw image from data acquisition is then compared to the reference and registered in the x- and y-direction, an example of which shown in Fig. 19. It was assumed that displacement occurred as pure translation in the x- and y-directions of the local camera coordinate system. This would determine the pixel displacement bias error due to mechanical vibration of the engine. The amplitude of the vibration, taken from Figure 18, for each camera in each direction is defined in Table 3.

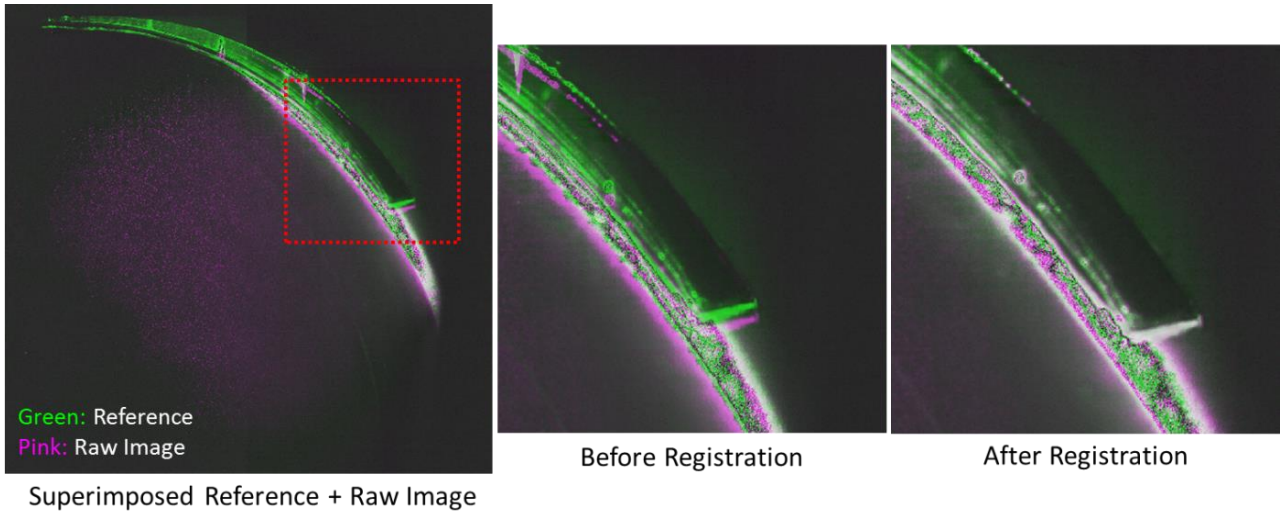

Figure 19. On the left, a raw data image (pink) is superimposed on a reference/calibration image (green) and the images are registered to determine the displacement between the images. In this example, $\Delta x = -0.123$ pixels and $\Delta y = -21.91$ pixels.

Table 3. Root mean square camera perturbation due to engine vibration.

	Δx (pixels)	**Δy (pixels)**
Camera 1	10.61	7.07
Camera 2	3.54	4.24

The correlation coefficient, R_i, can be calculated for the x- and y-movement for the two camera system. An R_i of +1 indicates a positive linear correlation, -1 a negative linear correlation, and an R_i of 0 indicates no linear correlation. Values that lie between these ranges indicate the strength of the correlation falling somewhere between linear and random, or nonlinear.

3.2.1 Correlated Camera Motion

It was first assumed that the correlation was perfectly linear, meaning that the movement of the two CCD cameras is synchronized with one another. To estimate the uncertainty of the SPIV measurements due to rig vibrations a Monte Carlo simulation was conducted wherein the camera displacement was modeled by spacially perturbing the mean flowfield by small amounts in x and y where the perturbation is randomly chosen from a Gaussian distributed PDF. The values from Table 3 were used as the standard deviation of the random data set in the simulation. The input state (CFD for NASA Inlet-A) was perturbed 10,000 times and the uncertainty was calculated (Fig. 20). The uncertainty due to vibrational effects for correlated camera motion has a maximum value of 0.275%. The largest values lie predictably along the largest velocity gradients. The meandering of the mean flow due to the vibration of the engine generates an apparent turbulence, which is actually just movement of the bulk mean on the camera sensor.

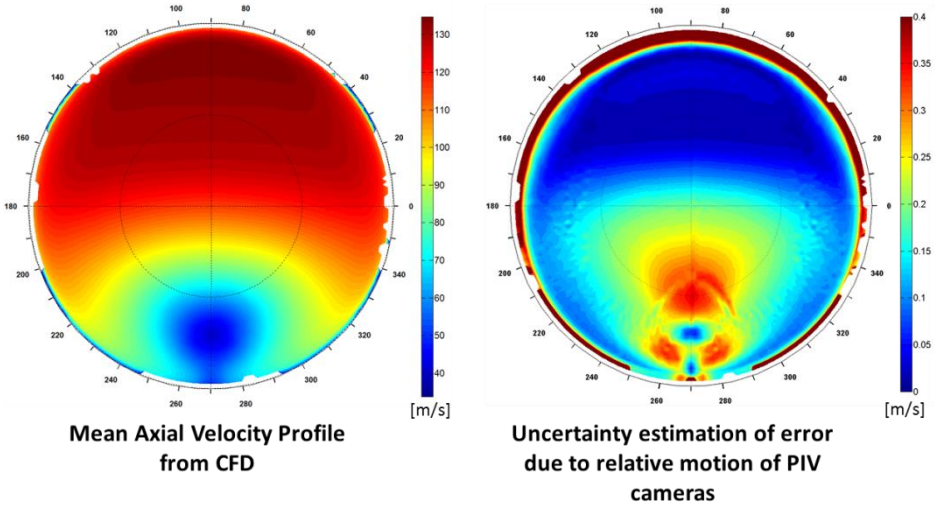

Figure 20. The input CFD profile (left) was perturbed in a Monte Carlo simulation to obtain the uncertainty (right), which peaks along the velocity gradients.

3.2.2 Uncorrelated Camera Motion

Next the camera movement was correlated (Fig. 21) and it was found that the correlation coefficient for x-movement, R_x, was -0.024 and R_y was -0.115. Both were sufficiently low to be categorized as random, meaning that the two cameras are perturbed independently of each other as a result of turbofan engine vibration.

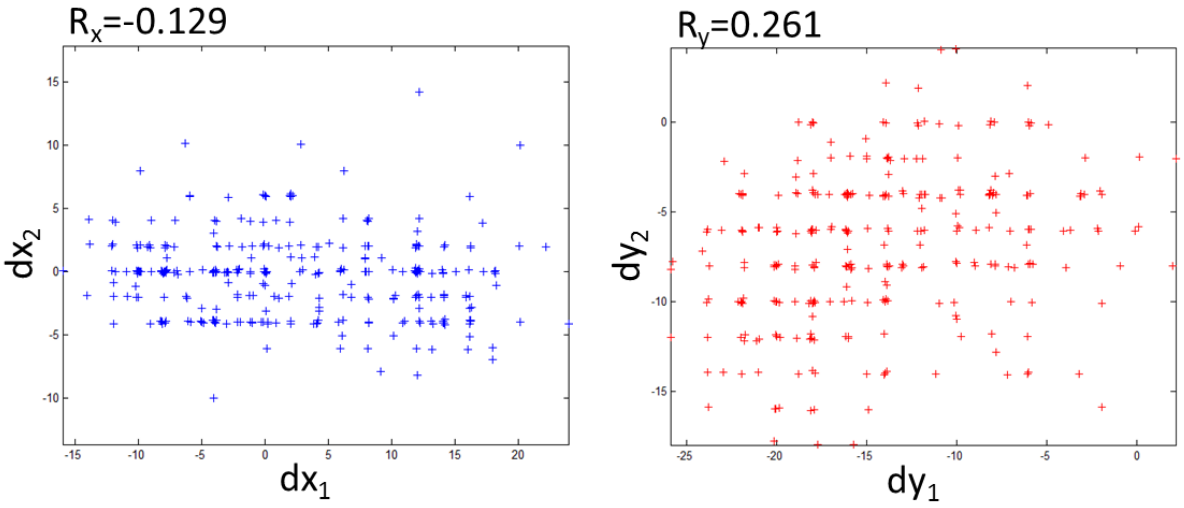

Figure 21. The correlation coefficient for the x-displacement (left) and y-displacement (right) for the two cameras was calculated, showing no correlation. The cameras move independently.

To quantify the uncertainty for the uncorrelated motion case, another Monte Carlo simulation was performed which would account for not only the random motion but also for the oblique viewing angle of the cameras. Two hundred baseline SPIV image sets were taken of an axisymmetric jet with an exit velocity of 8m/s in an environment where vibration is negligible. This raw image set was processed with LaVision's DaVis 7.2 software and post processed in MATLAB; the time-average velocity field is shown in Figure 22.

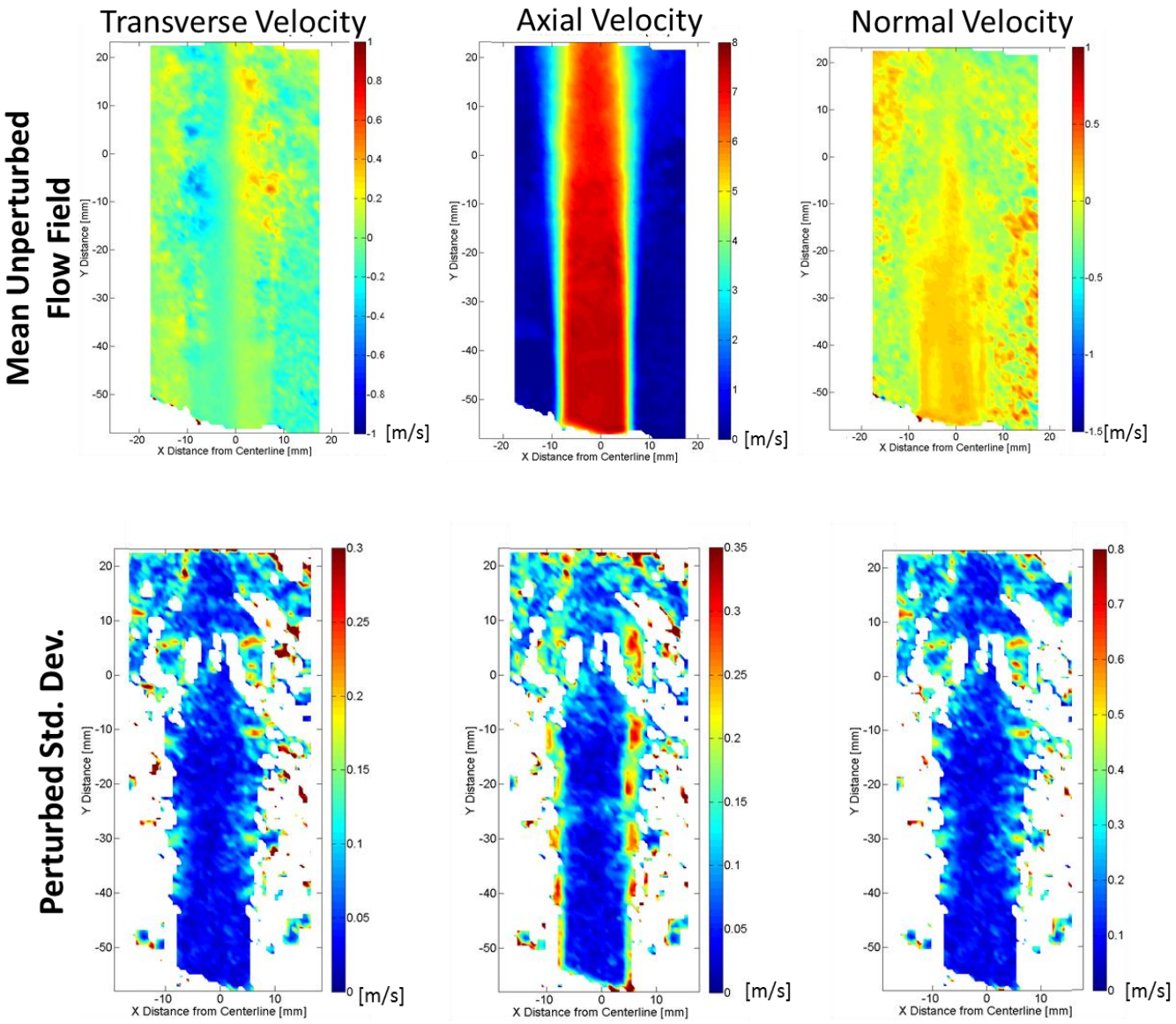

Figure 22. SPIV was performed for an axisymmetric jet; the mean flowfield (top) and the error due to perturbation (bottom).

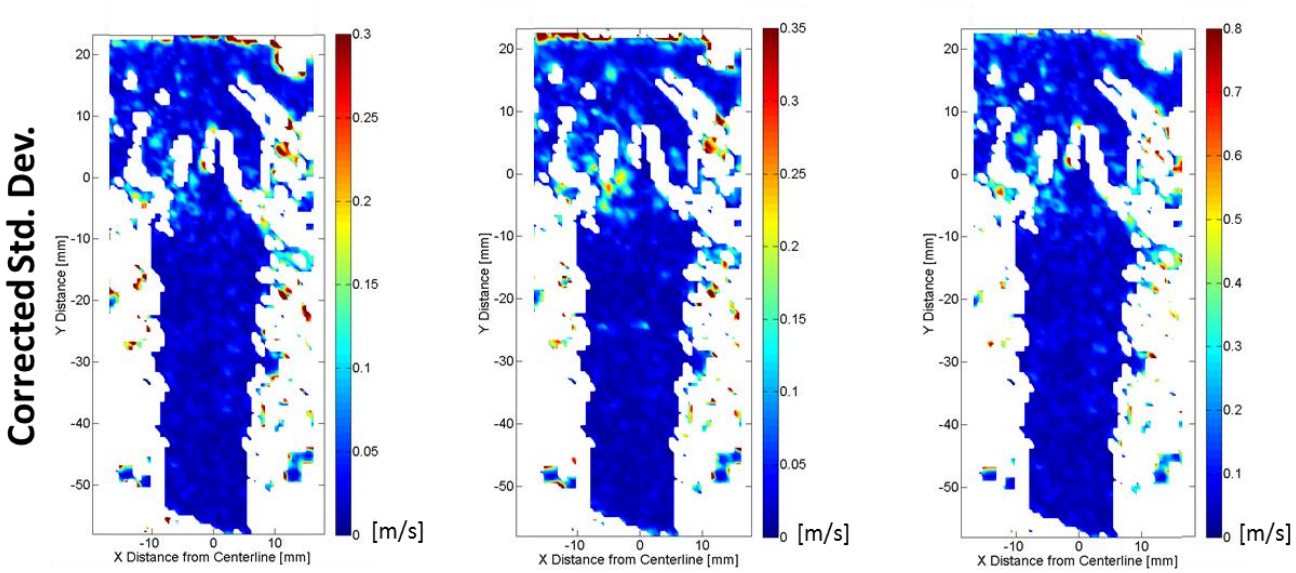

Figure 22. *Continued.* The displacement due to a simulated mechanical vibration was corrected, removing the bias error from the SPIV measurements.

In order to simulate the movement of the cameras such as is experienced on the distortion test rig, one of the two hundred image sets was chosen as the input state and was perturbed 2,000 times in a similar way as described in the previous section. In order to scale the perturbation properly to the different magnification of the axisymmetric jet experiment, equation 6 was used:

$$\delta(pixel)_{axisym} = \frac{\delta U_{TJ}}{U_{TJ}} U_{axisym} \Delta t_{axisym} \left(\frac{pix}{L}\right)_{axisym} \quad where \ \frac{\delta U_{TJ}}{U_{TJ}} = \left(\frac{\delta(pixel)}{U\Delta t}\frac{L}{pix}\right)_{TJ} \qquad (6)$$

To obtain the scaled down displacement uncertainty, $\delta(pixel)_{axisym}$, the normalized full scale (TJ) velocity uncertainty is multiplied by the scaled length of the axisymmetric experiment. Here U is the velocity component, Δt is the time between image frames, pix/L is the image scaling of the experiment, and $\delta(pixel)_{TJ}$ is the calculated displacement from the full scale experiment (see Table 3). This scaling resulted in a perturbation standard deviation of 3 pixels in the x-direction and 1.67 pixels in the y-direction for camera 1, and 1 pixel in the x- and y-direction for camera 2.

After the raw images were perturbed in the x- and y-directions, the image sets were processed with LaVision's DaVis 7.2 software and postprocessed in MATLAB. The uncertainty was estimated by calculating the standard deviation of the perturbed data, shown in Figure 22. Similar results occurred where the largest uncertainty lies along the strongest velocity gradients,

however, the magnitude of the uncertainty is much higher. Maximum values are 2.95%, 4.225%, and 6.7625% for the transverse, axial, and normal velocity components. The transverse and normal velocity components are 10% the magnitude of the dominant axial velocity, which is comparable to inlet swirl distortion data. The uncertainty in this simulation is an order of magnitude higher than the correlated motion simulation because the perturbation is occurring in the raw signal instead of the mean values and small changes cascade through the calculation of the camera calibration and the velocity vectors. This uncertainty will have a minimal effect on the time-averaged velocities and a stronger effect on turbulence calculations.

While the uncertainty values fall within reasonable limits, it is still desirable to mitigate the vibration effects to reduce the uncertainty. The displacement of the cameras could be accounted for via image processing as previously demonstrated and the perturbation removed from each raw, lowering the uncertainty due to test rig vibration from the engine (see Fig. 22). While the image registration is robust, there are images whose displacement is not properly detected, so some outliers will still occur. Stationary markings (See Fig. 11, methods H and I) were drawn on the test rig interior wall to help improve the robustness of the image registration for future correction of camera vibration. In addition to improving the effectiveness of the image registration using deliberate, high contrast markings, the mounting configuration of the CCD cameras and laser sheet could also be modified (Fig. 9) to reduce vibration-induced uncertainty.

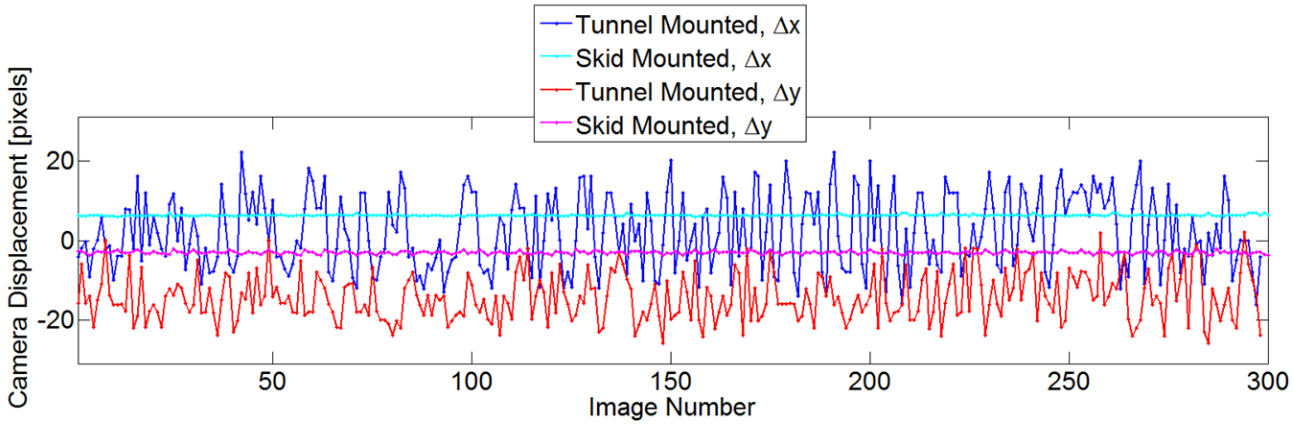

Figure 23. The displacement in the x- and y-directions of camera 1 for the tunnel mounted and skid mounted camera configurations during data acquisition for the HWB StreamVane screen.

The improvement of the stabilized setup over that previously discussed is shown in Fig. 23, where a comparison of the displacement for the two configurations is shown. In the skid mounted configuration, the cameras are mounted via extruded aluminum to the test stand skid. There are dampers in the connection between the engine and the test stand to decouple the engine vibration from the test stand. The test stand is bolted to a steel skid, which is bolted to the floor. While some vibration is still transmitted to the skid and, therefore, the camera mount configuration, the effects are minimal. The root mean square (RMS) displacement for the tunnel mounted camera is 9.293 and 5.968 pixels in the x- and y-directions, respectively. The RMS displacement for the skid mounted setup is 0.179 and 0.359 in the x- and y-directions, respectively, a reduction of 51.9 and 16.6 times, effectively removing camera vibration.

Because the cameras are moving during data acquisition, it was of interest to understand if any of that movement was "permanent" or if the cameras were always returning to their original spatial state by the end of a test. Images were taken with the engine off after calibrating the cameras and in between every data set. Then each image was compared to the image taken before testing using methods previously described; the results in Fig. 24 indicate that there is little to no change the horizontal orientation of the camera. There was an immediate change in the vertical orientation, which steadily became worse over successive runs in a linear trend. The change from run 1 to run 16 in the y-direction is 2.32 pixels. It is possible that the violent, rapid spin up of the engine causes these very small changes in position from one run to another. The uncertainty created by this phenomenon has not been estimated.

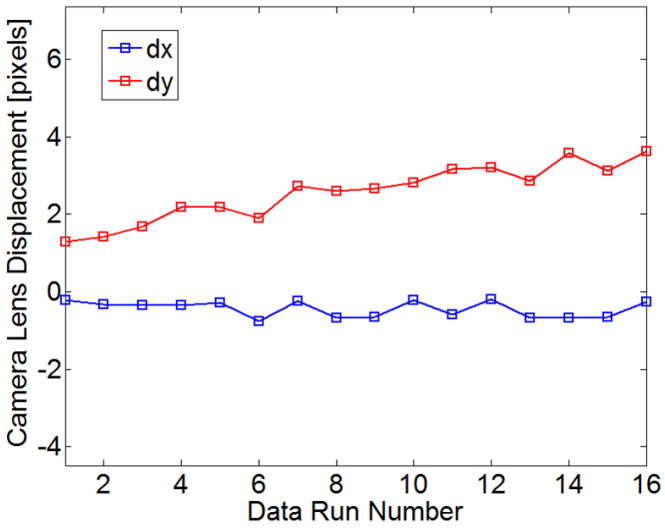

Figure 24. Permanent changes in the x- and y-spatial orientation of camera one for each data set. The engine is turned off between data sets.

3.3 Uncertainty in Calculated Results

In previous sections the uncertainty due to significant mechanical vibration was estimated for the three velocity components. Other important quantities such as swirl angle and Reynolds stress components are reported in the results section. The velocity components as calculated using PIV algorithms also have a general, baseline uncertainty, which is common to most experiments. These items will be addressed and summarized here.

The uncertainty in derived results can be calculated using equation 7, where *R* is the derived result and *a*, *b*, and, *c* are primary measurements.

$$\delta(R) = \sqrt{\left[\frac{\partial R}{\partial a}\partial(a)\right]^2 + \left[\frac{\partial R}{\partial b}\partial(b)\right]^2 + \left[\frac{\partial R}{\partial c}\partial(c)\right]^2 + \cdots} \tag{7}$$

Velocity is calculated according to equation 8, where the uncertainty in the displacement, Δx_p, is given to be 0.1 pixels for a majority of real data under ideal conditions.

$$V_p = \frac{\Delta x_p}{\Delta t} \quad where\ \delta(V_p) = \frac{\partial(\Delta x_p)}{\Delta t} \tag{8}$$

The uncertainty in the time between images, Δt, is negligible compared to the displacement uncertainty. The calibration performed by LaVision's software calculated a scale factor of 6.5948pixels/mm. Using the scale factor, a displacement uncertainty of 0.00001516 m is calculated. The time between images for the 50% corrected fan speed data is 9μs, which results in a velocity uncertainty of 1.68m/s, or 2.41% of the average profile velocity magnitude for the 50% corrected fan speed data. This agrees well with the repeatability uncertainty, given more samples to increase the degrees of freedom of the data set, which reduces the uncertainty by half.

Following the same process, the uncertainty in swirl angle (for definition, see Fig. 2) can be calculated to be 5.41%, which applies only to data subject to severe mechanical vibrations and in regions of velocity gradient. The uncertainty in swirl angle without consideration of vibration is 0.052%. While this value is very small, it again reflects real data under ideal conditions and only accounts for stereo-PIV uncertainty.

Reynolds stress is calculated according to equation 9. The unsteady velocity can be expressed as a sum of the average part, denoted with a bar over it, and the fluctuating part, denoted by an apostrophe.

$$\tau'_{ij} \equiv \rho\overline{u'_i u'_j} \quad where\ u_i = \bar{u}_i + u'_i \tag{9}$$

The turbulent kinetic energy, the root-mean-square of the velocity fluctuations, is characterized by equation 10.

$$TKE = \frac{1}{2}\left(\overline{u'_1{}^2} + \overline{u'_2{}^2} + \overline{u'_3{}^2}\right) \tag{10}$$

By applying equation 7 to the Reynolds stress and the turbulent kinetic energy (TKE), the uncertainty for a point in the measurement space can be calculated, which is reported in Table 4.

Table 4. Calculated uncertainties for velocity, swirl angle, Reynolds stress, and turbulent kinetic energy for both the general PIV measurements and for vibration affected measurements.

Quantity	**Uncertainty**
Velocity, General	2.41%
Velocity, Vibration	8.5%
Swirl Angle, General	0.052%
Swirl Angle, Vibration	5.41%
Reynolds Stress, General	0.2145 m^2/s^2
Reynolds Stress, Vibration	0.857 m^2/s^2
TKE, General	0.1709 m^2/s^2
TKE, Vibration	0.742 m^2/s^2

4. Results and Discussion

Using the experimental apparatus discussed in §2, several inlet distortion profiles were measured using stereoscopic particle image velocimetry to obtain the three component velocity vector field. The small scale test was completed as initial validation of the StreamVane method, with further validation using a five-hole probe being reported in [26]. Full scale testing was performed using a distortion screen designed to recreate a total pressure profile at the AIP and another distortion screen designed to generate a swirl profile at the AIP. The swirl descriptors will be used for comparison of analytic and experimental distortion data.

4.1 Small Scale Inlet-A Swirl Distortion

Two hundred images were calibrated and processed using DaVis 7.2 with a typical image interrogation of three iterations; one pass was done using 64x64 pixel interrogation windows followed by two passes with 32x32 pixel interrogation windows and 50% overlap to oversample the velocity field. One pixel unit in image space is equivalent to 0.0431 inches (1.094mm) in world space. The resulting vector fields were validated based upon image signal-to-noise ratio, correlation peak ratio, and normal distribution of data for time, which validation methods are further described in §4.4.

Contour plots of the three time-averaged velocity components along with the resulting 2D velocity vector field and swirl angle are given in Fig. 25. The primary features, two vortex cores, can be seen clearly, particularly in the velocity field, and the location of the cores and strength of the vortices are comparable to the model profile given by ‘Inlet A’. The magnitude of the swirl angle is slightly larger in the teal and light red regions of the top of the vortex cores, just inside the 1.5” radius line. Compared to the CFD input the vortex cores have moved in the positive vertical direction by 0.3683 inches (9.355mm) and have both moved toward one another by 0.006 inches and 0.004 inches for the left and right vortices, respectively. These experimental values differ from the expected value in part because of convection downstream of the screen; the turned vanes of the screen produce streamwise vortices which interact with each other and the solid surface of the tunnel due to induced velocities as predicted by the law of Biot and Savart and the method of images. In order to correct for this in future work, a vortex convection model has been made to predict the movement of the vortices in the test rig.

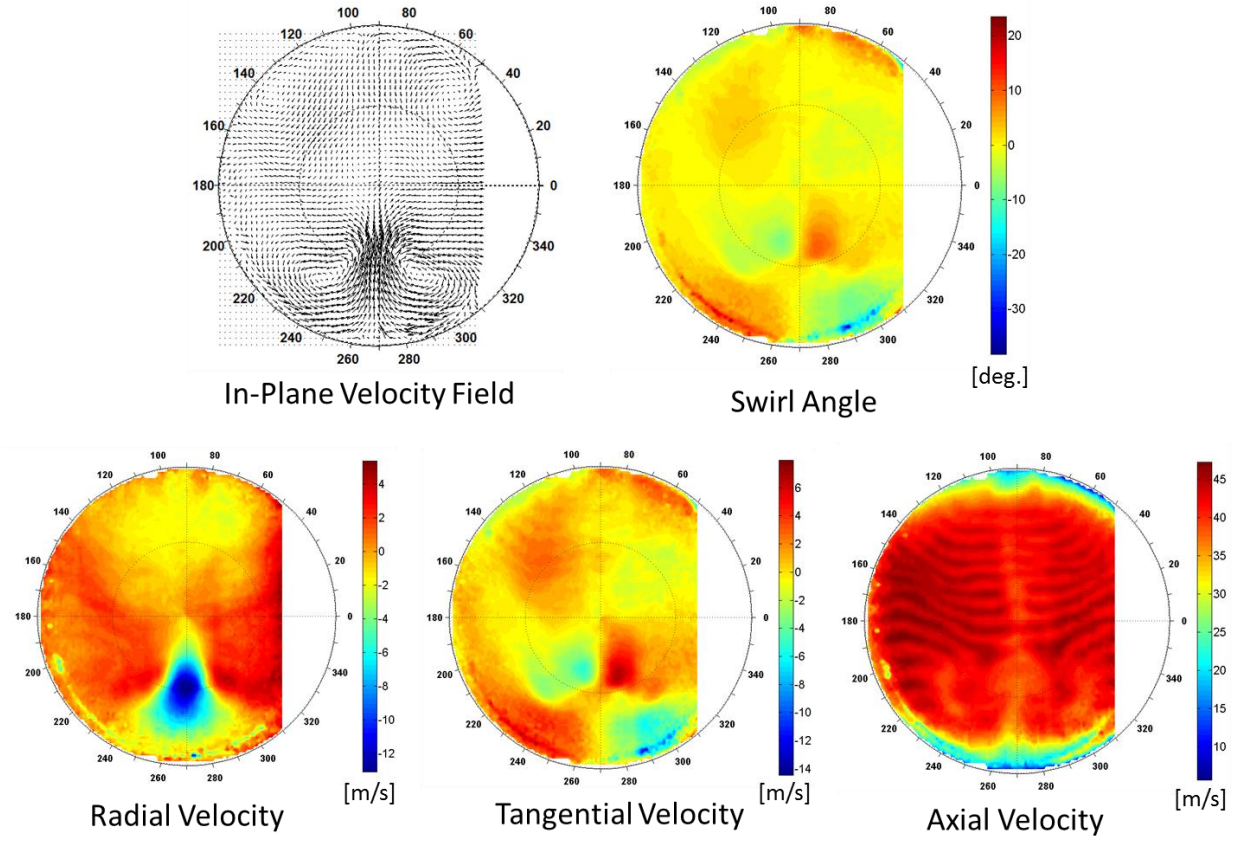

Figure 25. Stereo-PIV measurements of the 3D velocity vector field and swirl angle for the Inlet-A swirl distortion profile. A prominent vortex pair is measured in the bottom of the profile.

Because this has not yet been implemented experimentally, it is presented in the appendix and is not reflected in any data contained in the present work. It is proposed to start with the model profile at the AIP and step upstream to get the desired swirl distribution at the plane of the StreamVane screen.

Aside from vortex position and swirl magnitude, there are small regions of secondary flow at 50° and 140° near the wall that are likely a result of either non-smooth transitions in the tunnel test section or from imperfections in screen manufacturing. The three velocity components again show similar pattern and magnitude as the CFD input, though the axial velocity lacks a deficit in the bottom center of the data. The regions of wavy dark red in the axial velocity component are wakes from the turning vanes which have not yet mixed out in the flow. Of more interest is the comparison of swirl descriptors for the analytical and experimental data.

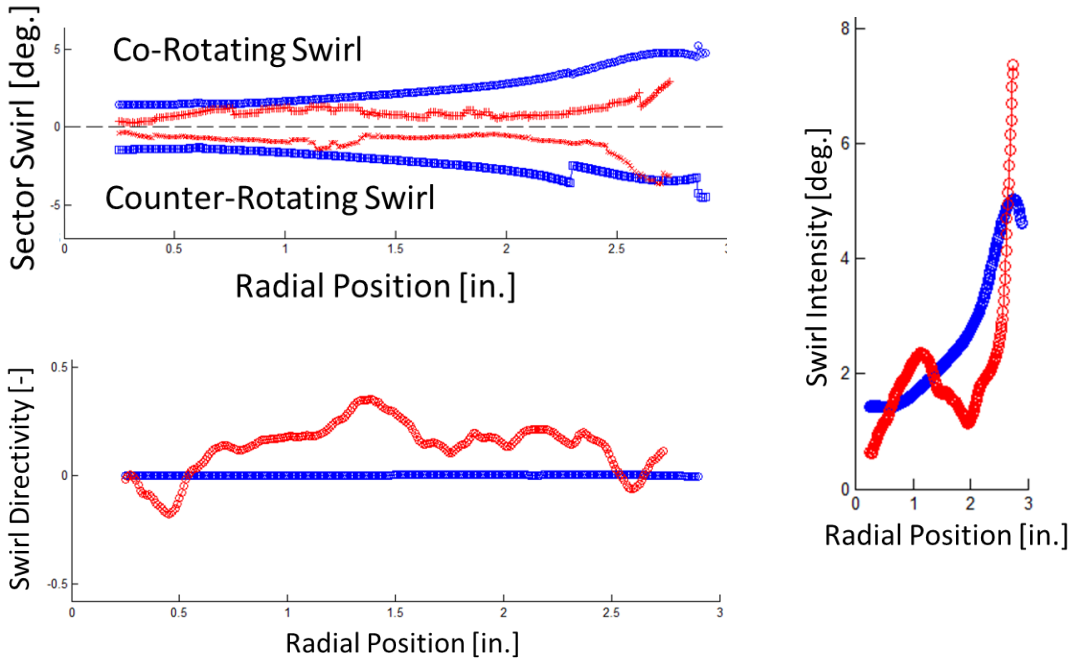

Figure 26. Analytic (CFD) and experimental sector swirl(top left), swirl directivity (bottom left), and swirl intensity (right) are plotted as a function of profile radius for the Inlet-A distortion.

Figure 26 shows the sector swirl, swirl intensity, and swirl directivity as a function of profile radius. The analytic sector swirl is characterized by a gradual increase in both positive and negative swirl in an equal manner; as radius increases the vortices are approached. Likewise, the swirl intensity increases with radius with a local maximum of 5 degrees just below the vortex pair followed by an increase to the global maximum of 5.7 degrees at the wall. The swirl directivity is a flat line with an average of 0.003, indicative of twin swirl as expected.

The experimental sector swirl parameter is nearly constant with radius, experiencing small fluctuations, through 75% of the radius after which both positive and negative swirl increase significantly. The swirl due to the vortices was appropriate created, however the remainder of the profile does not transition as well. The swirl intensity again has a similar trend of increasing intensity with a local maximum, but the local maximum occurs closer to the center of the profile and the global maximum 2 degrees more. The swirl directivity indicates that the experimental data represents a pattern in between twin swirl and a positive offset swirl with an average value of 0.136. As noted in [26], these differences could be caused by many factors, including the validity of the CFD profile from which the screen was designed, effects of scaling the CFD

profile, the location and extent of support structures, vane deformation, the nonlinearity of the cascade turning, the mixing of individual vane wakes, and downstream diffusion of the swirl profile. In spite of any differences between the analytical input and the experimental measurement, an important, real swirl distortion was generated and measured that consisted of a vortex pair which would have an impact on the performance of a fan system and subsequent engine systems.

4.2 Full Scale Inlet Distortion Test Rig

4.2.1 Total Pressure Distortion Screen

Five hundred images were calibrated and processed using DaVis 7.2 with the same three-iteration image interrogation as described in the previous section. One pixel unit in image space is equivalent to 0.00591 inches (0.015mm) in world space. The spatial resolution in the x- and y-direction is 2.35mm. The vector fields were again validated as described in §4.1.

Contour plots of the time-averaged radial, tangential, and axial velocity components along with the resulting 2D velocity vector field and swirl angle are given in Figs. 27 and 28 for the two engine power settings. Both the radial and tangential velocity components are small (maximum values ±7.27%) compared to the spacially averaged axial velocity. There are regions of apparent discontinuity and local minima/maxima which are believed to be due to inconsistent seeding and the presence of at least one ground vortex. The edge of the complete measurement volume is flower shaped because of a reflection of the laser sheet that was persistent through all images acquired. Data in the center of the profile has been removed because of insufficient seeding. There is a slight asymmetry in the measurement due to imperfections in the manufacturing of the screen.

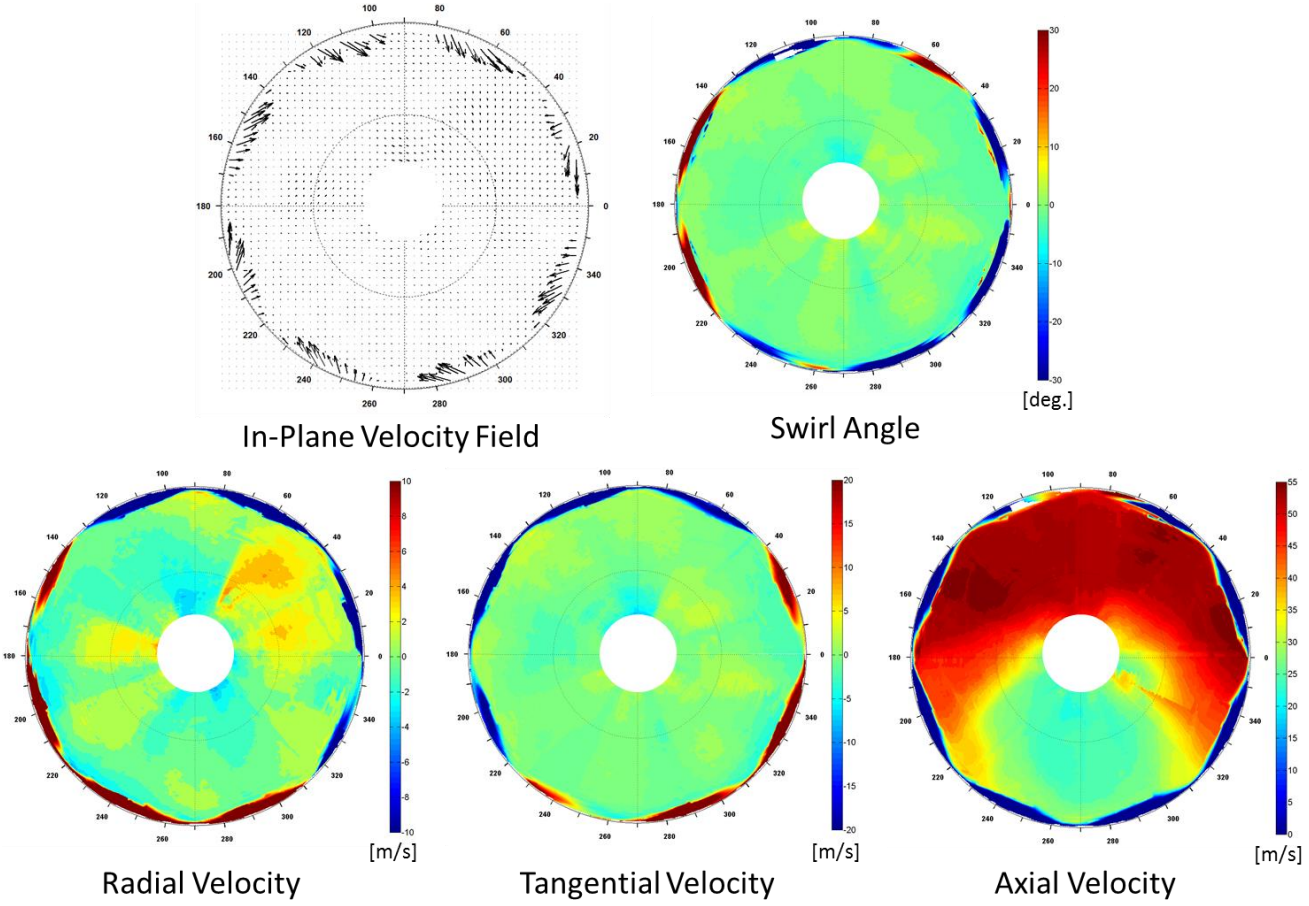

Figure 27. Inlet-A total pressure distortion profile at idle power setting produced the 3D velocity vector field and swirl angle, measured by SPIV.

The axial velocity component exhibits an expected velocity deficit in the region of lowest porosity, transitioning in the circumferential direction to the highest porosity region in the top of the profile. In the strongest region of the distortion the velocity deficit is 55.66%.

The purpose of acquiring data at with the total pressure distortion screen was not to recreate a specified swirl distortion at the AIP but to better understand the interaction between the gradients in a total pressure field and swirl distortion. It was anticipated that the differences in total pressure would influence the static pressure field, causing air to move from regions of high to low static pressure and would generate in-plane velocity components that contribute to swirl distortion. Instead, no significant swirl is detected at the AIP. The maximum swirl angle is 6° and the profile average magnitude is 1.5°. Maximum swirl angles in the analytic NASA Inlet-A profile are 15° with an average magnitude of 6°. This is important because it indicates that at the AIP the total pressure field and the swirl angle field are not coupled together and the effects of

each on fan performance and engine operability can be studied independently. This could also indicate that a total pressure distortion and swirl distortion could be added together to obtain the desired combined flow field. A recent study by Gunn et al. confirms the finding that significant swirl was not measured at the AIP due to a total pressure distortion alone. Gunn did measure swirl angle directly in front of the fan, indicating that much is still happening between the AIP and the fan face, which has yet to be investigated in the inlet distortion test rig.

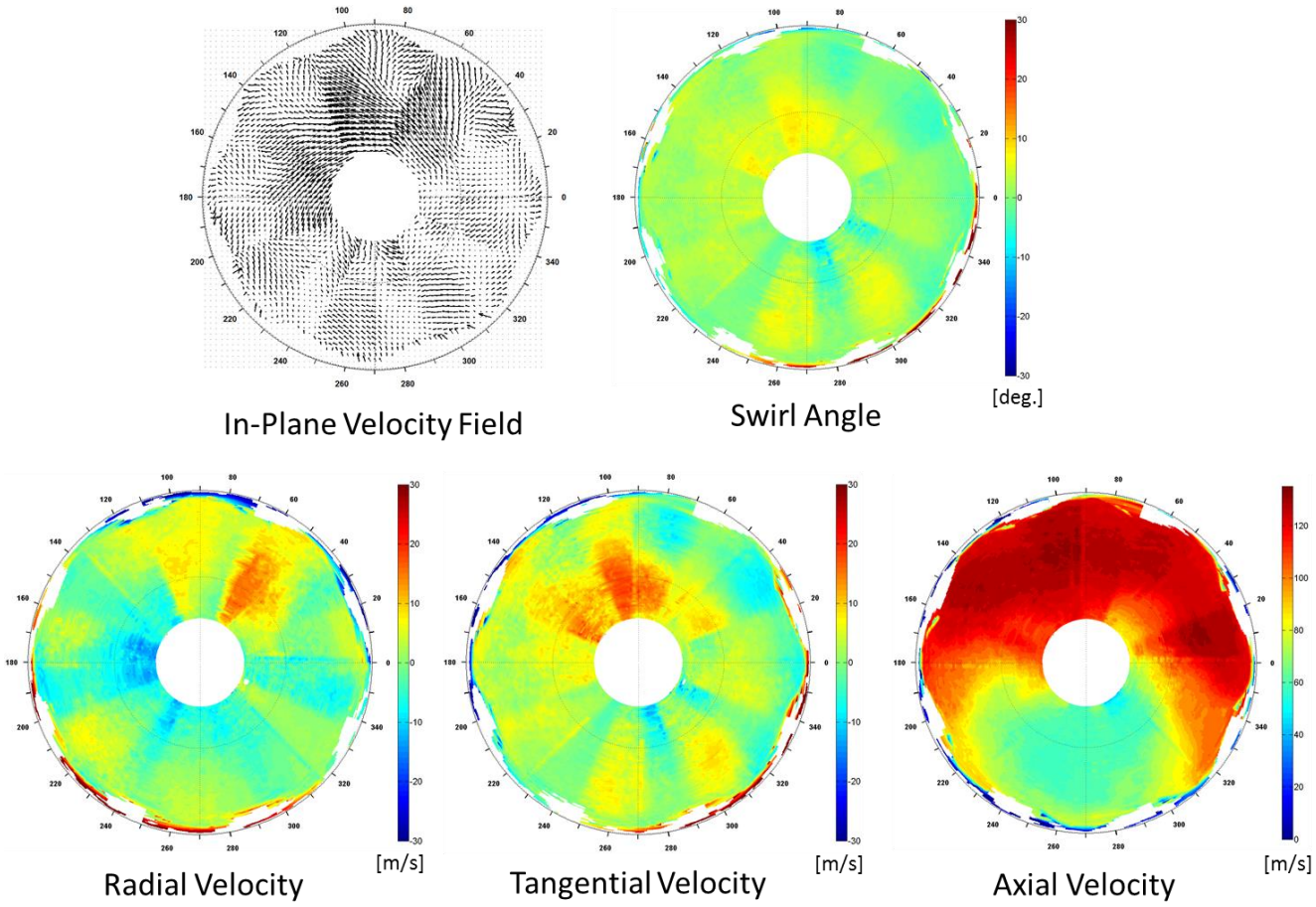

Figure 28. Inlet-A total pressure distortion profile measurements at 80% corrected fan speed.

The higher fan speed SPIV measurements show the same trends as the idle case but at a higher magnitude except for the velocity deficit, which stayed the same at 55.72%. The swirl angle has local maxima of 9° to 10° though the profile average is approximately 3.5° which is 2.333 times higher than the idle case. Because swirl angle can change so much with nominal axial flow speed, care must be taken to choose an appropriate corrected fan speed for matching

the swirl profile, though in this case 80% corrected fan speed represents a mass flow that is close to engine stall because of the strength of the distortion. Because the total pressure screen was not designed to recreate a specific swirl distortion and because no meaningful swirl angle was measured at the AIP, the swirl descriptors were not applied to this profile for comparison.

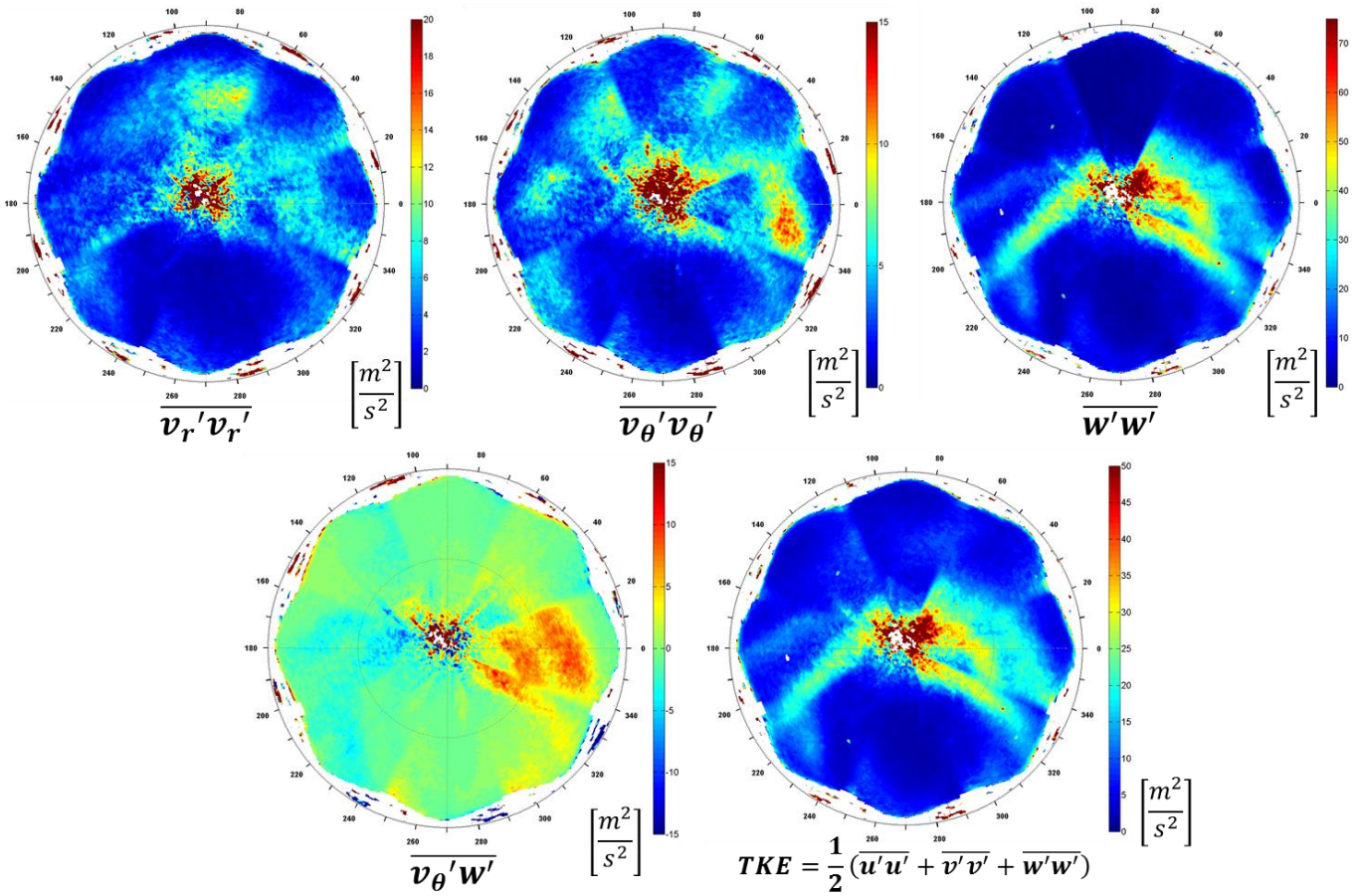

Figure 29. The normal components of the Reynolds stress tensor, a shear component, and the turbulent kinetic energy are plotted for the idle power setting; Total pressure distortion.

Because each PIV image pair represents an instant in time, other interesting aerodynamic quantities such as Reynolds stress and turbulent kinetic energy (TKE) can be easily calculated. Velocity in an unsteady flowfield can be split into a mean part and a fluctuating part. When the Navier-Stokes equations are written given the mean and fluctuating parts and averaged, a term exists which is the Reynolds stress, a correlation of fluctuating parts of the velocity field. Reynolds stress is indicative of the average turbulence present from combinations of different velocity components and must be modeled in CFD software to close or complete the Navier-Stokes equations. Turbulent kinetic energy is the square root of the summation of squares of the

principal Reynolds stress components and indicates the total magnitude of turbulence in the flowfield.

The Reynolds stress tensor is plotted in Figure 29 for the idle fan speed data. The TKE for the same data is also plotted in Figure 29.

4.2.2 HWB Swirl Distortion Screen

Five hundred images were taken for each measurement volume, with 50% overlap, such that 1,000 images per measurement volume were available for averaging and higher order statistics. This was important to account for any inconsistencies in seeding uniformity. Images were processed using DaVis 8 with settings previously described. One pixel unit in image space is equivalent to 0.00591 inches (0.015mm) in world space. The spatial resolution in the x- and y-direction is 2.35mm. Contour plots of the time-averaged radial, tangential, and axial velocity components along with the resulting 2D velocity vector field and swirl angle are given in Fig. 30 for a corrected fan speed of 50%. The data does not extend to the full extent of the maximum radius because of laser glare from the top window. Positive bulk swirl encompasses the majority of the profile and is evident in the in-plane velocity vector field. The intersection with the other vortex is also clearly seen, though the majority of the tightly wound vortex is cut off. The edges of that vortex are seen in the extreme blue and red regions in the radial velocity component. The remainder of the measured profile is nearly entirely tangential flow except for the first quadrant, which exhibits minimal radial flow. Tangential flow is intensified in the region where the two vortices meet. Of great interest is the swirl measurement, which is characterized by positive bulk swirl with an average magnitude of approximately 15 degrees. No vanes are present in the center of the screen, which is essentially the center of the bulk swirl vortex so the swirl is near zero. The maximum swirl is measured where the vortices interact, with a maximum value of 35 degrees. This matches the same pocket of 35 degree swirl distortion in the input profile. While it is anticipated that an even higher value of swirl exists near the wall as defined in the input profile, this cannot be validated with this measurement. The input profile includes regions of significant radial flow, especially in the bottom of the profile, which could be the influence of the inlet lip of the turbofan engine. In practice, though that radial flow may be generated directly behind the StreamVane screen, the flow in the test rig became more vortical in nature and is more representative of flow in an inlet duct.

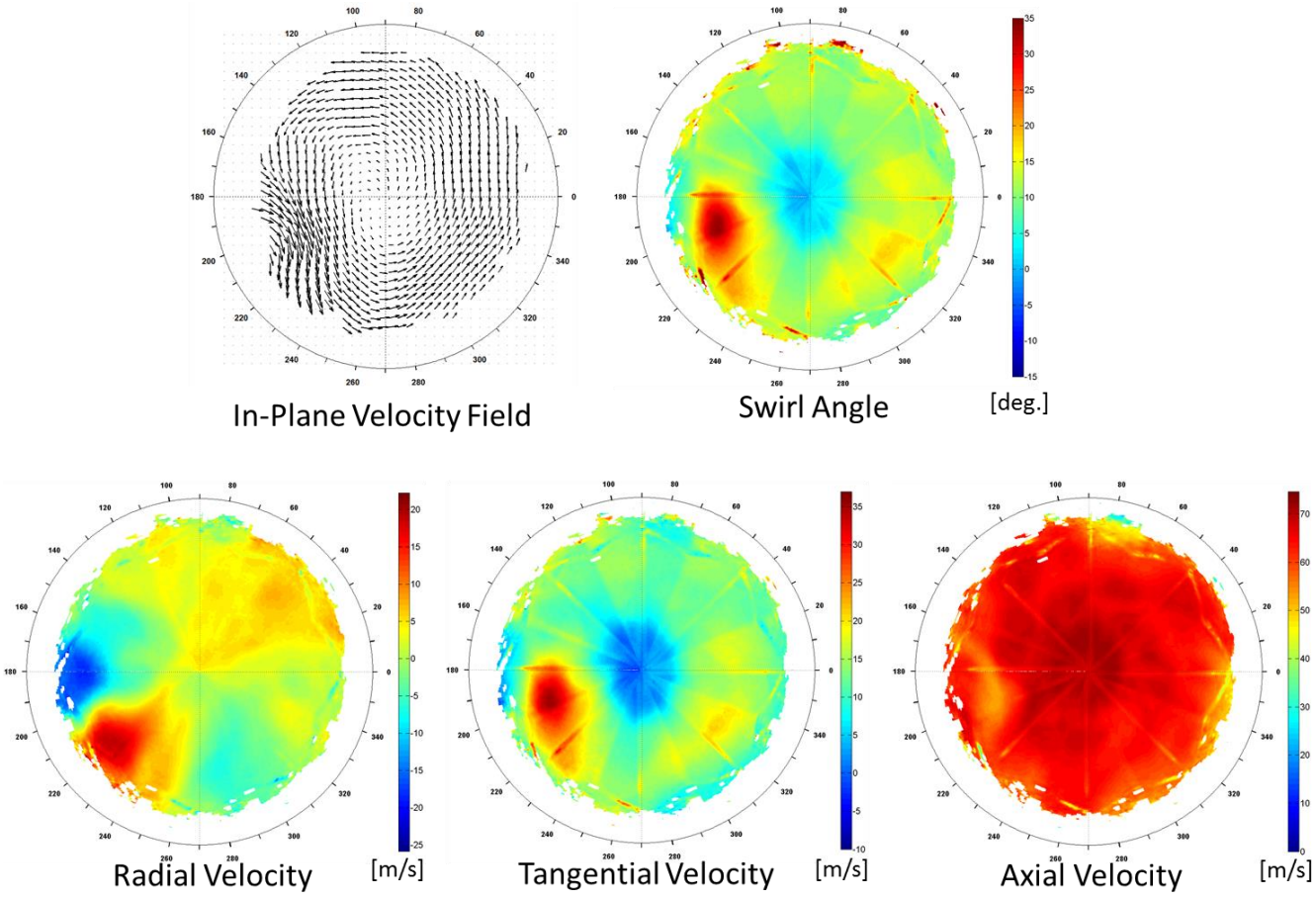

Figure 30. Hybrid wing body swirl distortion profile at 50% corrected fan speed; Contour plots of the 3D velocity vector field and swirl angle.

Portions of the Reynolds stress tensor for the HWB profile are shown in Fig. 31, which again indicates turbulence generated by the screen, specifically the structural supports.

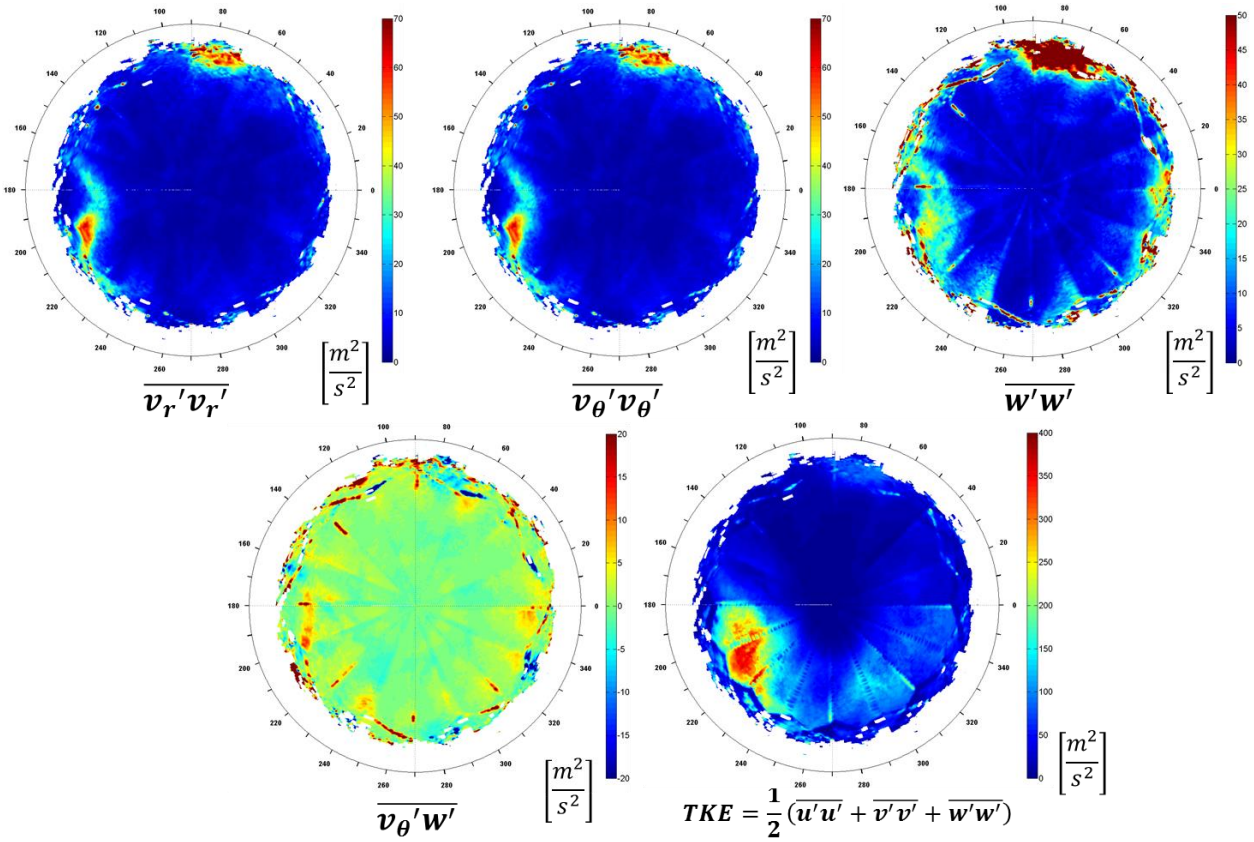

Figure 31. The normal components of the Reynolds stress tensor, a shear component, and the turbulent kinetic energy are plotted for 50% corrected fan speed; HWB swirl distortion.

4.3 Performance and Effect of Scale on the Measured Distortion

The swirl descriptors were used to best understand how the full scale StreamVane screen performed compared to the CFD input. It is also of interest to understand the relationship between the measured flow field of the sub scale and full scale screen. The x- and y-coordinates of all three profiles were normalized to obtain a radius of unity. Figure 32 shows a comparison of rings of swirl angle unwrapped. Each subplot is identified by the top left depiction of the swirl profile. At every radial location the normalized sub scale and full scale data match well. There is a small circumferential offset, which is due to the fact that the full scale StreamVane screen did not begin in a vertical position in the tunnel, but was slightly clocked due to tunnel manufacturing imperfections. In the fourth (green) and fifth (yellow) rings, the full scale data did not reach the same magnitude as the sub scale data, indicating that perhaps the fan weakens the flow angularity. Overall the StreamVane produced a flowfield with similar patterns as the CFD

input and, most importantly, generated one of the two extreme values of swirl angle, +34°. It is also important to note that the CFD input did not include the effects of a fan.

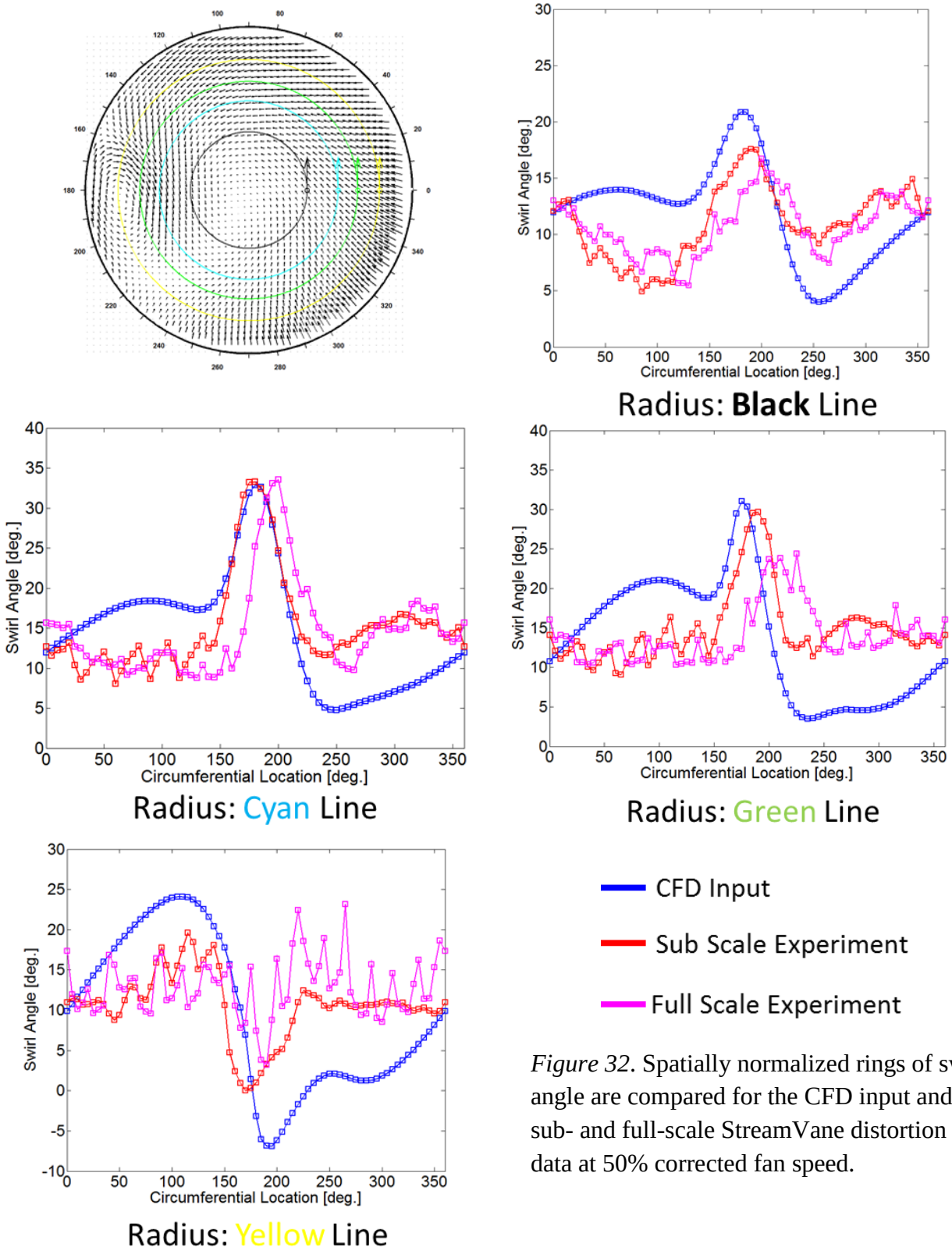

Figure 32. Spatially normalized rings of swirl angle are compared for the CFD input and the sub- and full-scale StreamVane distortion screen data at 50% corrected fan speed.

As the vortices approach the fan their diameter increases and tangential velocity is lost to maintain a constant circulation, which could be contributing to underperformance of the screen in this very complex flow. Figure 33 shows the sector swirl, swirl intensity, and swirl directivity as a function of radius for the input HWB swirl profile, the sub scale experimental data, and the full scale experimental data. It is evident from the analytic sector swirl and swirl directivity that the profile is dominated by positive bulk swirl.

The sector swirl has only a positive component and the swirl directivity is one for 76% of the radius of the profile, after which positive offset swirl is dominant. The swirl intensity is generally increasing, peaking where the two vortices meet and add together in a positive sense. There is a decline in swirl intensity moving from the edge of the smaller vortex through to its center, followed by a rapid increase in swirl intensity through the region of strongest swirl angle on the left side of smaller vortex.

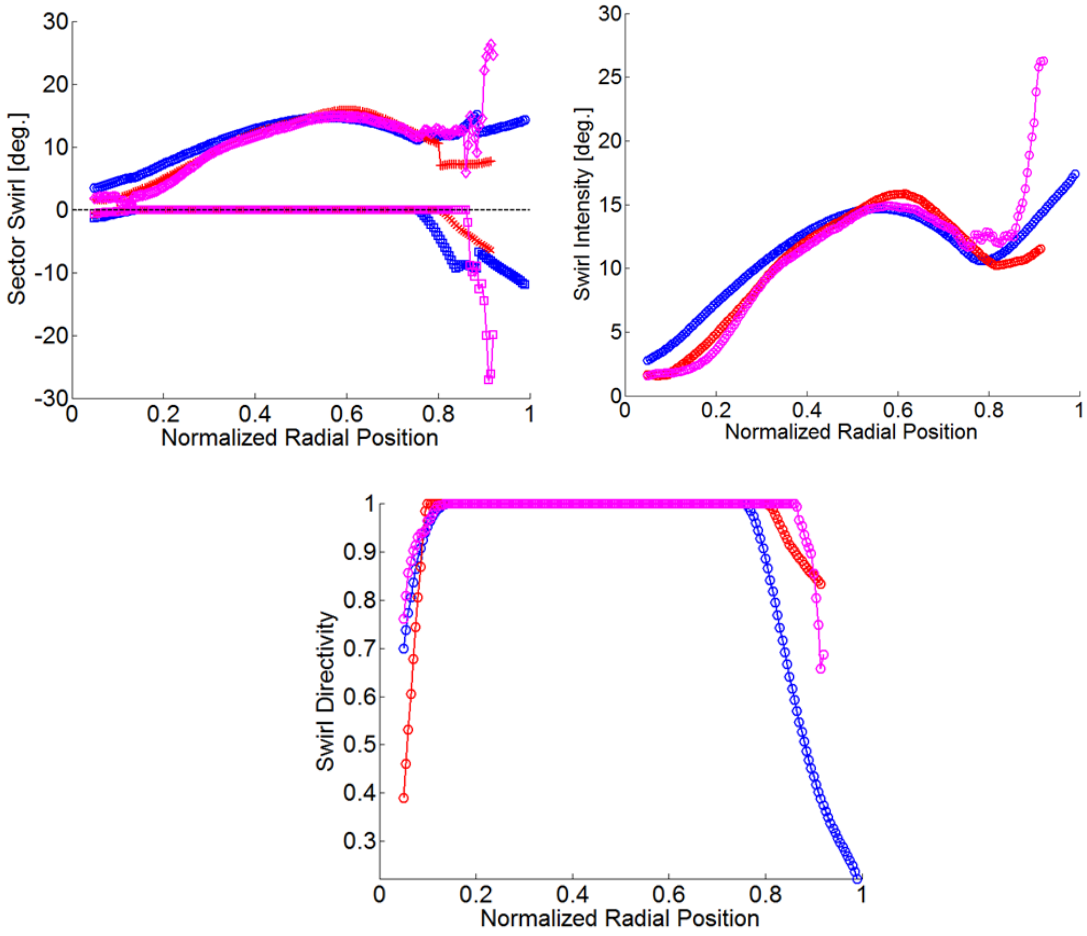

Figure 33. Spatially normalized sector swirl, swirl intensity, and swirl directivity for the CFD input, sub- and full-scale data for the hybrid wing body swirl profile at 50% corrected fan speed.

4.4 Data Validation

Because of the unsteady flow in the inlet distortion test rig, seed was not globally distributed throughout each image but was locally concentrated at different instants in time. There is a challenge to appropriately average this information without including spurious velocity data from regions where there is little to no seed particles. Three main methods are used to filter spurious vectors to improve the overall averaging of data.

4.3.1 Imaged Based Signal-to-Noise Ratio (SNR) Validation

The most fundamental piece of information in PIV is the raw image. Raw images are split up into small, square subregions called interrogation windows which are then cross-correlated in two dimensions to obtain a displacement at the point in space that is located at the center of the interrogation window. A mapping function is used to convert 2D image space in the camera sensor frame of reference to 3D world space in the measurement plane of reference. The quantity being correlated is pixel intensity. A new method [60] of removing spurious velocity vectors in PIV data attacks the problem at this most fundamental step, calculating the SNR of the image intensity and removing velocity vectors that do not fall within a valid range of SNR for both image frames of either camera per PIV image.

Figure 34 shows a sample raw image that is colored for image intensity. Seed particles are typically evident as a teal color. Regions of very high intensity are due to either too high a seed density or a reflection of the laser sheet and its resulting glare. Red dots signify valid interrogation windows for those image frames. While it may appear that valid seed has been ignored, there must be a valid SNR in both image frames for the same interrogation window for one camera it to be considered acceptable. Other correlation based SNR methods suffer from false positives whereas this method is more robust, except in regions of strong laser flare. Laser flare can be mitigated by applying surface treatments such as flat black paint which absorb more of the light than an untreated sheet metal finish. As previously stated, fluorescent paint can also be used in combination with a filter; green light at 532nm wavelength will fluoresce from a surface at a higher wavelength, which can be filtered out in the imaging with a small cost in light intensity from seed particles.

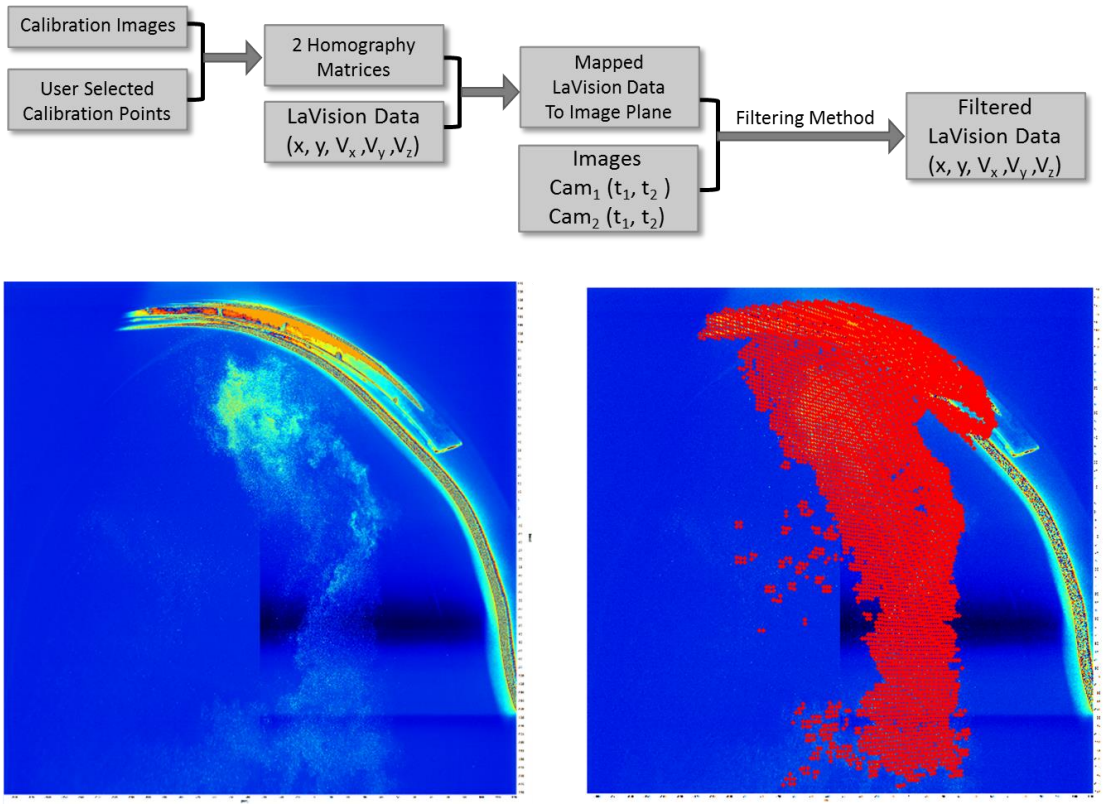

Figure 34. Top: A schematic of the 'particle percentage' data validation process. Bottom: A raw PIV image on the left and the corresponding valid interrogation windows (red) on the right.

4.3.2 Peak Ratio Validation

Peak ratio (PR), the ratio of the highest correlation peak to second tallest peak (Fig. 35), is an excellent measure of cross-correlation SNR and was used as a second pass to remove vectors with a peak ratio less than 1.30 and higher than 45. It was observed in plots of peak ratio that known regions of spurious data consistently had PR values that fell exactly between 50 and 51, and that were exactly 100. The cause of this phenomenon is unknown, however, it effectively removed spurious data.

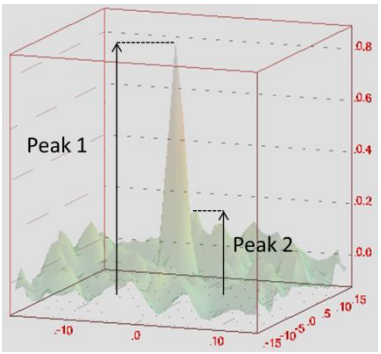

Figure 35. Sample cross correlation of two interrogation windows from DaVis 7.2 showing the highest two peaks.

4.3.3 Statistical Based Validation

The final filter used was simply to generate a time histogram at each point in space and remove any data that falls outside of $\pm 2\sigma$ of the median of the data set, where σ is the standard deviation. The median was used because the histograms were initially heavily skewed due to numerous images with no seed at the given point in space. After the initial pass of this filter was applied, the median and σ were recalculated and the process was repeated until convergence was achieved.

The combination of these validation methods has provided the highest quality data given intermittent seeding in a highly unsteady flowfield such as is the case in an operating turbofan jet engine. The image-based SNR filter effectively the amount of poor data input to the time average whereas the other two methods are effective at removing extreme outlying data points.

5. Conclusion and Recommendations

The StreamVane method of generating any arbitrary swirl distortion profile was demonstrated in a small scale wind tunnel using stereoscopic particle image velocimetry to measure three components of velocity. The distortion was characteristic of a boundary layer ingesting profile and was made into an ABS plastic screen using additive manufacturing. A full-scale inlet distortion test rig was described as well as the stereo-PIV measurement system used to measure planar, three-dimensional velocity vector fields. The challenges of implementing a PIV system with the test rig are examined, especially the proper seeding of the flow field. The final seeding configuration was accomplished by the use of two seeder-blower systems and a uniform porosity turbulence screen that covered the inlet of the test cell.

A full-scale total pressure distortion representative of a boundary layer ingesting inlet was generated by a wire mesh screen and measured in the inlet distortion test rig using SPIV at the aerodynamic interface plane at idle and 80% corrected fan speed power settings. The swirl profile was negligible at the AIP. Reynolds stress quantities indicate turbulence generated by the screen.

For the first time a full-scale swirl distortion representative of a hybrid wing body application was generated by a StreamVane screen and measured in the test rig at the AIP at 50% corrected fan speed. Two distinct vortices were seen, the combination of bulk swirl and a tightly wound vortex. The measurements were normalized and compared to the input profile and sub-scale measurements made in a related work. Favorable agreement was found between both experimental data sets, which strengthens the case for sub-scale development of future StreamVane design optimization and testing. While the full-scale PIV measurements did not extend fully to the wall, the maximum positive swirl angle was matched in both magnitude and location. The experimental data follows the same general trends as the CFD input. Future work could include more measurements made between the AIP and the fan rotor to better understand the development of the profile as it approaches the fan, which would lead to a better understanding of fan response to a complex distortion and could be the means of improving further upon the StreamVane method. The experimental data also compared well with three swirl descriptors, matching both trends and magnitude. This is important because the commonality in

swirl descriptors indicates that the fan will respond the same for the analytic CFD swirl profile and the actual measured swirl distortion.

Sources of uncertainty specific to the inlet distortion test rig were identified and the bias error due to mechanical vibration was estimated, scaled to other experiments, and a solution to minimize that error, aside from changing the experimental setup, was proposed. This error was found to be less than 7% for all velocity components. This error analysis and mitigation can continue to be made more robust and applied to SPIV image data. A data validation technique developed in conjunction with this research was also explained.

Necessary updates to the StreamVane method were also made, including a one-dimensional structural analysis to determine the normal stress in the turning vanes. The HWB StreamVane screen was designed to have a minimum factor of safety of 5, achieved by including more structural supports. The convection of distinct point vortices was modeled to better understand the streamwise development of a swirl distortion profile and to possibly improve the input profile used by the StreamVane method. A small but significant change was made to the airfoil profile of the StreamVane which improved aerodynamic performance and the quality of screen manufacturing via 3D printing.

With the full-scale validation of the StreamVane method, future work can be dedicated to more fundamental swirl distortion profiles. Fan response and engine operability can be investigated in detail and, with this understanding, novel distortion resistant fans can be designed to maintain the benefits of highly integrated airframe/engine systems.

References

[1] Collier, F., "Overview of NASA's Environmentally Responsible Aviation (ERA) Project: A NASA Aeronautics Project Focused on Midterm Environmental Goals," 48th AIAA Aerospace Sciences Meeting, Orlando, FL, January 4-7 2010.

[2] Suder, K., Delaat, J., Hughes, C., Arend, D., and Celestina, M., "NASA Environmentally Responsible Aviation Project's Propulsion Technology Phase I Overview and Highlights of Accomplishments," AIAA Paper 2013-0414, 51st Aerospace Sciences Meeting, Grapevine, TX, January 7-10 2013.

[3] Thomas, R., Burley, C., and Olson, E., "Hybrid Wing Body Aircraft System Noise Assessment with Propulsion Airframe Aeroacoustic Experiments," AIAA Paper 2010-3913.

[4] Sutliff, D., Brown, C., and Walker, B., "Hybrid Wing Body Shielding Studies using an Ultrasonic Configurable Fan Artificial Noise Source Generating Typical Turbofan Modes," AIAA Paper 2014-0256, 52nd Aerospace Sciences Meeting, National Harbor, MD, Jan. 13-17 2014

[5] Gatlin, G., Vicroy, D., and Carter, M., "Experimental Investigation of the Low-Speed Aerodynamic Characteristics of a 5.8-Percent Scale Hybrid Wing Body Configuration,"

[6] Drela, M., "Development of the D8 Transport Configuration," AIAA Paper 2011-3970, 29th AIAA Applied Aerodynamics Conf., Honolulu, HI, June 27-30 2011.

[7] Pandya, S., Huang, A., Espitia, A., and Uranga, A., "Computational Assessment of the Boundary Layer Ingesting Nacelle Design of the D8 Aircraft," AIAA Paper 2014-0907, 52nd Aerospace Sciences Meeting, National Harbor, MD, Jan. 13-17 2014.

[8] Callahan, G., and Stenning, A., "Attenuation of Inlet Flow Distortion Upstream of Axial Flow Compressors," Vol. 8, No. 4, Journal of Aircraft, April 1971.

[9] Soeder, R., and Mehalic, C., "Effect of Combined Pressure and Temperature Distortion Orientation on High Bypass-Ratio Turbofan Engine Stability," NASA Technical Memorandum 83771, Oct. 1984.

[10] Flitcroft, J., Dunhan, J., and Abbott, W., "Transmission of Inlet Distortion Through a Fan," Technical Report, DTIC Document, July 1987.

[11] Wadia, A., "Experimental Investigation of a Forward Swept Rotor in a Multistage Fan with Inlet Distortion," Vol. 2011, Int'l Journal of Aerospace Engineering, Article ID 941872, July 2011.

[12] Govardhan, M., and Viswanath, K., "Investigations on an Axial Flow Fan Stage Subjected to Circumferential Inlet Flow Distortion and Swirl," Vol. 6, No. 4, Journal of Thermal Science, May 1997.

[13] Yao, J., Gorrell, S., and Wadia, A., "A Time-Accurate CFD Analysis of Inlet Distortion Induced Swirl in Multistage Fans," AIAA Paper 2007-5059, 43rd AIAA/ASME/SAE/ASEE Joint Propulsion Conf., Cincinnati, OH, July 8-11 2007.

[14] Wu, Y., Ng, E., and Wong, K., "Numerical Study of the Swirl Flow in the F-5E Intake with Subsonic Speeds," Mathematical and Computer Modeling 48 (2008) 447-467, Oct. 2007.

[15] Yao, J., Gorrell, S., and Wadia A., "High-Fidelity Numerical Analysis of Per-Rev-Type Inlet Distortion Transfer in Multistage Fans – Part II: Entire Component Simulation and Investigation," Vol. 132, Journal of Turbomachinery, Oct.2010.

[16] Fidalgo, V., Hall, C., and Colin, Y., "A Study of Fan-Distortion Interaction Within the NASA Rotor 67 Transonic Stage," Vol. 134, Journal of Turbomachinery, Sept. 2012.

[17] Gunn, E., Tooze, S., Hall, C., and Colin, Y., "An Experimental Study of Loss Sources in a Fan Operating With Continuous Inlet Stagnation Pressure Distortion," Vol. 135, Journal of Turbomachinery, Sept. 2013.

[18] SAE Aerospace Information Report, "A Methodology for Assessing Inlet Swirl Distortion," SAE AIR5686, Oct. 2010.

[19] Sylvester, T., Brown, R., and Connor, C., "F-35B Lift Fan Inlet Development," AIAA Paper 2011-6940, AIAA Centennial of Naval Aviation Forum, Virgina Beach, VA, Sept. 21-22 2011.

[20] Hamed, A., and Numbers, K., "Inlet Distortion Considerations for High Cycle Fatigue in Gas Turbine Engine," AIAA Paper, 2007.

[21] Bailie, S., "Effects of Inlet Guide Vane Flow Control on Forced Response of a Transonic Fan," Dissertation at Virginia Polytechnic Institute and State University, Oct. 2003.

[22] Kozak, J., "Investigation of Inlet Guide Vane Wakes in a F-109 Turbofan Engine with and without Flow Control," Dissertation at Virginia Polytechnic Institute and State University, Aug. 2000.

[23] Genseler, M., Meyer, W, and Fottner, L., "Development of Intake Swirl Generators for Turbojet Engine Testing," Technical Report, DTIC Document, July 1987.

[24] Sheoran, Y., and Bouldin, B., "A Versatile Design of a Controlled Swirl Distortion Generator for Testing Gas Turbine Engines," ASME, 2008.

[25] Sheoran,Y., Bouldin, B., and Krishnan, P., "Advancements in the Design of an Adaptable Swirl Distortion Generator for Testing Gas Turbine Engines," ASME, 2009.

[26] Hoopes, K., "StreamVane Work"

[27] Dunavant, J., "Cascade Investigation of a Related Series of 6-Percent-Thick Guide-Vane Profiles and Design Charts," NASA Technical Note 3959. Journal of Fluid Mechanics, 332:71-104, 1997.

[28] Hathaway, M., "Unsteady Flows in a Single-Stage Transonic Axial-Flow Fan Stator Row," NASA Technical Memorandum 88929, Dec. 1986.

[29] Suder, K., Hathaway, M., Okiishi, T., Strazisar, A., and Adamczyk, J., "Measurements of the Unsteady Flow Field Within the Stator Row of a Transonic Axial-Flow Fan Part I: Measurement and Analysis Technique," NASA Technical Memorandum 88945, 1987.

[30] Hathaway, M., Suder, K., Okiishi, T., Strazisar, A., and Adamczyk, J., "Measurements of the Unsteady Flow Field Within the Stator Row of a Transonic Axial-Flow Fan Part II: Results and Discussion," NASA Technical Memorandum 88945, 1987.

[31] Strazisar, A., Wood, J., Hathaway, M., and Suder, K., "Laser Anemometer Measurements in a Transonic Axial-Flow Fan Rotor," NASA Technical Paper 2879, Nov. 1989.

[32] Mehalic, C., "Effect of Spatial Inlet Temperature and Pressure Distortion on Turbofan Engine Stability," NASA Technical Memorandum 100850, AIAA-88-3016.

[33] Denny, A., Horine, J., Nichols, R., Morton, S., Klepper, J., and Savelle, S., "Inlet/Engine Integration Examples Using Coupled Transient and Steady Engine Performance Models with Kestrel," AIAA Paper 2014-0753, 52nd Aerospace Sciences Meeting, National Harbor, MD, Jan. 13-17 2014.

[34] Park, J., Heister, S., and Sullivan, J., "Development of a Counter-Rotating Vortex Pair (CVP) Mixer for Aerospace Applications," AIAA Paper 2013-3832, 49th AIAA/ASME/SAE/ASEE Joint Propulsion Conf., San Jose, CA, July 14-17 2013.

[35] Pazur, W., and Fottner, L., "The Influence of Inlet Swirl Distortions on the Performance of a Jet Propulsion Two-Stage Axial Compressor," Vol. 113, Journal of Turbomachinery, April 1991.

[36] Mitchell, G., "Effect of Inlet Ingestion of a Wing Tip Vortex on Compressor Face Flow and Turbojet Stall Margin," NASA Technical Memorandum X-3246, July 1975.

[37] Gunn, E., and Hall, C., "Aerodynamics of Boundary Layer Ingesting Fans," ASME Turbo Expo 2014: Turbine Technical Conference and Exposition, Dusseldorf, Germany, June 16-20 2014.

[38] Stevens, C., Spong, E., and Hammock, M., "F-15 Inlet/Engine Test Techniques and Distortion Methodologies Studies," NASA Contractor Report 144866, June 1978.

[39] Chima, R., Arend, D., Slater, J., and Truax, P., "CFD Models of a Serpentine Inlet, Fan, and Nozzle," NASA Technical Memorandum 216349, May 2010.

[40] Walsh, K., Yuhas, A., Williams, J., and Steenken, W., "Inlet Distortion for an F/A-18A Aircraft During Steady Aerodynamic Conditions up to 60° Angle of Attack," NASA Technical Memorandum 104329, April 1997.

[41] Southwick, R., Gallops, G., Kerr, L., Kielb, R., Welsh, M., DeLaat, J., and Orme, J., "High Stability Engine Control (HISTEC) Flight Test Results," NASA Technical Memorandum 208481, July 1998.

[42] Orme, J., DeLaat, J., Southwick, R., Gallops, G., and Doane, P., "Development and Testing of a High Stability Engine Control (HISTEC) System," AIAA.

[43] Schroder, A., Geisler, R., Schanz, D., Agocs, J., Pallek, D., Schroll, M., Klinner, J., Beversdorff, M., Voges, M., and Willert, C., "Application of Image Based Measurement Techniques for the Investigation of Aeroengine Performance on a Commercial Aircraft in Ground Operation," 17th Int'l Symp. on Applications of Laser Techniques to Fluid Mechanics, Lisbon, Portugal, July 7-10 2014.

[44] Raffel, M., Willert, C., Werely, S., and Kompenhaus, J., "Particle Image Velocimetry: A Practical Guide," 2nd ed. 2007, Springer.

[45] Melling, A., "Tracer Particles and Seeding for Particle Image Velocimetry," Meas. Sci. Technol. 8, 1406-1416, Oct. 1997.

[46] Lazar, E., DeBlauw, B., Glumac, N., Dutton, C., and Elliott, G., "A Practical Approach to PIV Uncertainty Analysis," AIAA Paper 2010-4355, 27th Aerodynamic Measurement Technology and Ground Testing Conference, Chicago, Illinois, 28 June – 1 July 2010.

[47] Xue, Z., Charonko, J., and Vlachos, P., "Signal-to-Noise Ratio, Error and Uncertainty of PIV Measurements," 10th Int'l Symp. on PIV, Delft, Netherlands, 1-3 July 2013.

[48] Nobach, H., and Bodenschatz, E., "Limitations of Accuracy in PIV Due to Individual Variations of Particle Image Intensities," J. of Exp. Fluids 47:27-38, Feb. 2009.

[49] Jacobs, J., "Iced Airfoil Separation Bubble Measurements by Particle Image Velocimetry," Dissertation, University of Illinois at Urbana-Champaign, 2007.

[50] Bian, S., Ceccio, S., and Driscoll, J., "A Dual-Camera Cinematographic PIV Measurement System at Kilohertz Frame Rate for High-speed, Unsteady Flows," Journal of Experimental Fluids, 48:487-495, 2010.

[51] LaVision GmbH, "Product Manual: FlowMaster DaVis v8, 2014.

[52] Beresh, S., and Smith, B., "Effects of Spatial Realignment in Stereo PIV Calibration," AIAA Paper 2014-1101, 52nd Aerospace Sciences Meeting, National Harbor, 13-17 Jan. 2014.

[53] van Doorne, C., Westerweel, J., and Nieuwstadt, F., "Measurement Uncertainty of Stereoscopic-PIV for Flow with Large Out-of-Plane Motion," Chapter from "Particle Image Velocimetry: Recent Improvement," p213-227, 2004.

[54] Ferrar, A.M., and O'Brien, W.F. 2012 "Fan Response to Total Pressure Distortions Produced by Boundary Layer Ingesting Serpentine Inlets," 48th AIAA/ASME/SAE/ASEE Joint Propulsion Conf., 30 July – 01 Aug, Atlanta, Georgia, paper AIAA 2012-3996.

[55] Johns, C., "The Aircraft Engine Inlet Vortex Problem," AIAA Paper 2002-5894, Aircraft Technology Integration and Operations, Los Angeles, CA, 1-3 Oct. 2002.

[56] Paterna, E., Moonen, P., Dorer, V., and Carmeliet, J., "Mitigation of Surface Reflection n PIV Measurements," Technical Design Note, Meas. Sci. Technol. 24 057003, 16 April 2013.

[57] Gorton, S.A., Owens, L.R., Jenkins, L.N., Allan, B.G., and Schuster, E.P. 2004 "Active Flow Control on a Boundary-Layer-Ingesting Inlet," 42nd AIAA Aerospace Sciences Meeting & Exhibit, 5-8 January, Reno, Nevada, paper AIAA 2004-1203.

[58] Berrier, B.L., and Morehouse, M.B., 2003 "Evaluation of Flush-Mounted, S-Duct Inlets With Large Amounts of Boundary Layer Ingestion," Applied Vehicle Technology Panel Meeting, No. 39, NASA Langley Research Center.

[59] Bagsik, A., and Schoppner, V., "Mechanical Properties of Fused Deposition Modeling Parts Manufactured with ULTEM*9085," ANTEC, Boston, MA, 2011.

[60] Kirk, C., Lowe, K., "On Post-Processing Turbofan Engine Inlet PIV Data under Highly Intermittent Seeding Conditions," AIAA Paper

[61] Bühler, O. "Statistical Mechanics of Strong and Weak Point Vortices in a Cylinder," Phys. of Fluids, Vol. 14, No. 7, July 2002.

[62] Pozrikidis, C. "Introduction to Theoretical and Computational Fluid Dynamics," Oxford University Press, 2011.

Appendices

A.1 StreamVane Method Improvements

In order to implement the StreamVane method for inlet swirl distortion in the full scale test rig, two significant concerns were addressed to improve the method's performance and safety. These additions fit directly in with the five steps that were outlined in the introduction and do not alter the method as described.

A.1.1 Downstream Vortex Convection of the Swirl Profile

By definition of swirl distortion, non-zero velocity components in the circumferential and radial directions are present in the desired swirl profile and are constituted by discrete vortices. This vorticity can be generated by the boundary layer at the leading edge of a wing upstream of the engine, for example, and is ingested by the engine. The StreamVane method generates a specific 3D flow field in the test rig at the plane of the screen, with the measurement plane being any distance downstream of the screen plane. After the vortices are created at the screen plane they will induce a convective velocity on the rest of the flowfield as they move downstream according to the law of Biot-Savart. The vortices will have moved with respect to each other and their starting location by the time they have reach the measurement, which is located one fan diameter downstream of the screen. This vortex convection contributes to the error in the actual swirl profile produced and can be corrected by applying fundamentals of vortex dynamics.

In fluid dynamics, the governing equations of continuity, momentum (Navier-Stokes), and energy can be simplified by making assumptions of constant density and irrotational flow to obtain ideal flow conditions. It can be shown that the complex velocity field for a point vortex under these conditions is given by equation 1A.

$$W(z) = \frac{-i\Gamma}{2\pi(z - z_1)} = u - iv$$
$$\Gamma = \oint \vec{V} \cdot d\vec{s} \qquad (1A)$$

where W is the complex velocity, Γ is the circulation, z is the position in the complex plane, equal to $x+iy$, z_1 is the complex position of a vortex core, u is the spanwise velocity component, and v is the vertical velocity component. The circulation is calculated by the closed integral of the dot product of velocity, V, with path length, s. Then the method of images can be applied to simulate the circular cylinder surface of the distortion test rig. It can be shown [61, 62] that a circular surface can be simulated by placing an image vortex according to equation 2A.

$$\vec{X}_{image} = \frac{\vec{X}_{vort} R^2}{|X_{vort}|^2} \qquad (2A)$$

where $\boldsymbol{X}_{image}$ is the position of the image vortex and $\boldsymbol{X}_{vort}$ is the position of the vortex to be contained inside the circular surface. The circulation for each vortex is found drawing concentric circles of increasing radius that emanate from the center of each vortex. The average velocity around the circle is multiplied by the circle circumference to obtain an estimation of circulation as a function of radius. The value of gamma is taken to be that where two vortices meet. Having established the boundary conditions and the vortex circulation, N point vortices will be released and allowed to convect. The convection velocity, W_c, of the i^{th} vortex is the sum of the complex velocity of all point vortices, including image vortices, excluding the i^{th} vortex, which is expressed as equation 3A.

$$W_c(z_i) = \sum_{\substack{j=1 \\ j \neq i}}^{N} \frac{-i\Gamma_j}{2\pi(z_i - z_j)} \qquad (3A)$$

The vortex convection velocity can thus be found at a finite plane in the test rig. To simulate the movement of vortices due to convection downstream of the swirl screen, the Euler method can be used to solve the ordinary differential equation dx/dt = U(x,t) given the initial condition of the starting vortex position. Figure 36 shows an example of an input velocity vector field and the downstream convection of the vortex pair where the duct length is exaggerated to show the vortex movement.

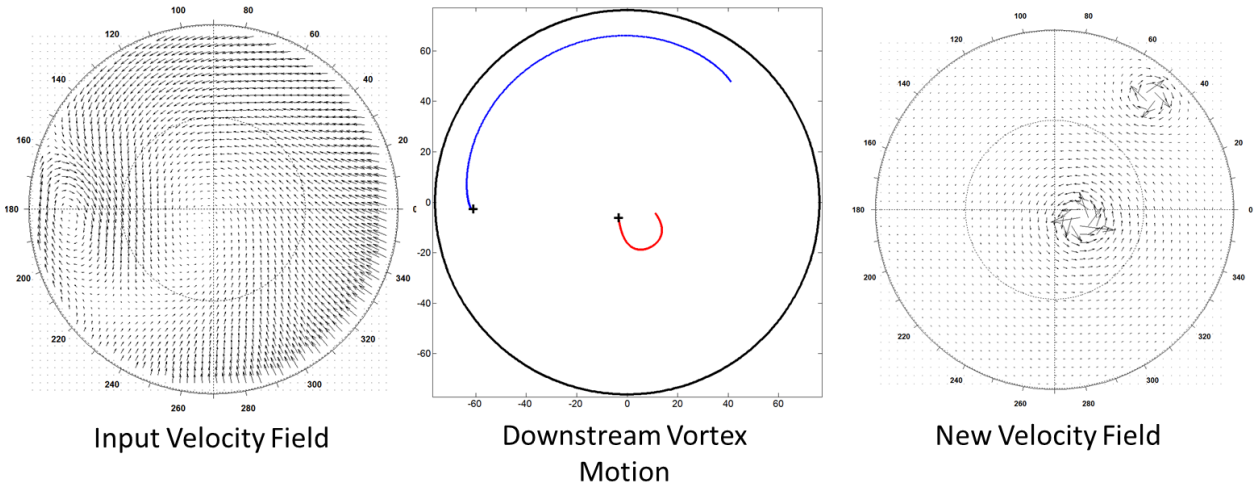

Figure 36. The input velocity field is discretized into point vortices, which are allowed to convect in ideal flow; the resulting flow field is estimated.

While it is interesting to have an understanding of where the vortices will be downstream of screen as the engine's fan interacts with the swirl profile, of greater interest to the StreamVane method is to be able to move upstream of distortion screen. The measurement plane is one fan diameter downstream of the distortion plane, so a negative "time" step can be applied to the vortex convection analysis to find the velocity vector field one diameter upstream of the original input profile. This upstream vector field would then become the new vector field for the StreamVane method such that by the time the vortices convected one diameter downstream, they would be located where desired in the original input swirl profile. Figure 37 shows a crude example of the original velocity vector field and the new, upstream convected velocity field. It is crude because a small amount (two) of vortices were used to model the flow field. If more point vortices are used, the resulting velocity vector field would much more closely reflect the nature of the original input velocity field. It would also be necessary to account for and shift the corresponding axial velocity components to match the respective change that occurs in the in-plane velocity components. For these reasons, this important step has not yet been implemented in the screen presented in the current work.

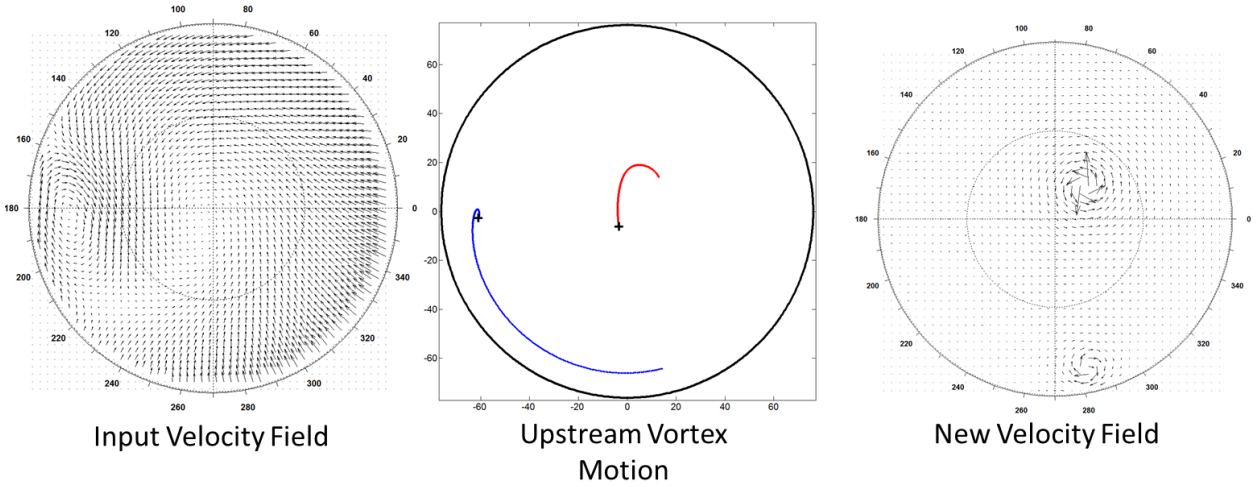

Figure 37. The flow field of discretized vortices is now allowed to convect backwards upstream.

With the ability to estimate the convected velocity vector field, the swirl profile at the AIP will have reduced uncertainty and the actual fan response will more closely match that which would be produced for the desired swirl profile. There are some limitations to this estimation. This model only predicts the x-y position of the vortices at a given plane and does not account for stretching of vortex filaments, which influences the circulation and convection velocity. It is recommended that small scale experimentation be conducted to validate this convection model. Further validation could be obtained by obtaining SPIV measurements directly in front of the fan to see both the movement of the discrete vortices as well as any change in vortex strength. Of the current five steps outlined in the StreamVane method in §1.2.1, obtaining a new velocity vector field due to vortex convection would become a new step in between steps one and two.

A.1.2 StreamVane Screen Normal Stress Analysis

All of the data obtained in [26] was performed on six inch diameter, ABS plastic swirl distortion screens with a maximum clean, axial velocity of 50m/s. The next step after validating the StreamVane method was to scale the screen's size so that it could be used with the inlet distortion test rig. At full scale the screen could experience axial flow speeds upwards of 135m/s which would generate much higher stresses in the screen. Additionally, structural failure of the screen in the inlet distortion test rig could result in damage to the research turbofan jet engine

that powers the test rig. Because of the complex geometry, a structural mesh could not be obtained for finite element analysis (FEA), so a lower order stress estimation was done to ensure that a sufficient factor of safety (FOS) was designed in the screen.

This was further driven by a lack of professional additive manufacturing companies that could 3D print a single part in a metallic material having a print bed with a volume requirement of at least 23x23x9 inches. For those companies with printers of the appropriate size, the strongest commercial plastic found was Ultem^{TM} 9085, a thermoplastic used in Fused Filament Fabrication (FFF). Depending on the build orientation and raster angle of the part, the maximum tensile strength has been found [59] to be 81MPa in the x-direction at a raster angle of 0°, 67MPa in the y-direction at a raster angle of 0°, and 43MPa in the z-direction at a raster angle of 30° and 45°. A change in build direction or angle can reduce the maximum tensile strength by nearly half and care should be taken to have the part properly printed.

The swirl distortion screen is modeled by independent beams having a tapered, rectangular cross section with boundary conditions defined as either fixed end (clamped on both ends) or cantilever. The beam base width changes along the length of a turning vane because the screen solidity is kept constant at two while the distance between turning vanes is variable, leading to a variable chord. Structurally this is important because the moment of inertia, I_x, varies along the length of a turning vane. The normal stress in each beam was found by using the integral method of beam theory as defined in equation 4A.

$$V_y(x) = \int F(x)dx + C_1$$
$$M_z(x) = \int V_y(x)dx + C_2 \qquad (4A)$$
$$EI(x)\frac{d^2u}{dx^2} = M_z(x)\,, \quad I(x) = \frac{bh^3}{12}$$

here V_y is the shear force, x is the distance along the beam, $F(x)$ is the distributed load along a turning vane, $C_{1,2}$ are constants of integration, M_z is the internal moment, E is the young's modulus, $I(x)$ is moment of inertia, u is the beam displacement, b is the length of the camber line of the turning vane, and h is the turning vane thickness. The displacement equation is required for the fixed end beam because it is statically indeterminate, having four unknowns. By applying

principles of statics and the boundary conditions, the following internal moment equations can be derived for both beam types. L is the beam length.

Fixed end:

$$M_z(x) = \iint F(x)dxdx - R_1 x + M_1$$

$$M_1 = \frac{\frac{B_L{}'}{B_L} A_L - A_L{}'}{C_L} \frac{B_L}{B_L{}'}$$

$$A_L = \int_0^L \frac{\iint F(x)dxdx}{I(x)} dx \quad , \quad A_L{}' = \iint_0^L \frac{\iint F(x)dxdx}{I(x)} dx$$

$$B_L = \int_0^L \frac{x}{I(x)} dx \quad , \quad B_L{}' = \iint_0^L \frac{x}{I(x)} dx$$

$$C_L = \int_0^L \frac{1}{I(x)} dx$$

$$R_1 = \frac{A_L + M_1 C_L}{B_L}$$

Cantilever:

$$M_z(x) = \iint F(x)dxdx - x\int_0^L F(x)dx + L\int_0^L F(x)dx - \iint_0^L F(x)dxdx$$

The distributed force is found from CFD analysis [27] of linear cascade data for the NACA A_4K_6 camber line with a constant thickness profile. The beam is divided into discrete elements and the lift force is found at each element to obtain a discrete function. MATLAB's *trapz* and *cumtrapz* functions are used to perform the numerical integrations. The lift force per unit span is determined from equation 5A.

$$F_i = \frac{1}{2}\rho {V_{ax}}^2 C_{l_i} c_i \qquad (5A)$$

$$C_{l_i} = \frac{\theta_i}{24.02}$$

where F is the lift force, ρ is the air density, V_{ax} is the axial velocity, C_l is the section lift coefficient, c is the chord, and θ is the local turning angle. At each discrete element the following quantities are found in order to quantify the normal stress in the beam: turning angle, section lift coefficient, chord, camber line length, moment of inertia, and lift force. For the symmetric turning vane cross section, the normal stress is determined using equation 6A, where y is half of the vane thickness.

$$\sigma_{xx}(x) = \frac{M_z(x)y}{I(x)} \tag{6A}$$

The input conditions for the stress distribution include a vane thickness of 3.5mm, an axial velocity of 135m/s, which corresponds to an approximate corrected fan speed of 80%, and a tensile strength of 71.6MPa. The calculation was done for the HWB swirl profile. The resulting stress distribution in each turning vane is shown in Figure 38. The black lines represent structural supports. As expected, stress is concentrated at the walls for both beam boundary conditions. The maximum stress is 55.12MPa which is a factor of safety of 1.30, predicting that the screen would not fail.

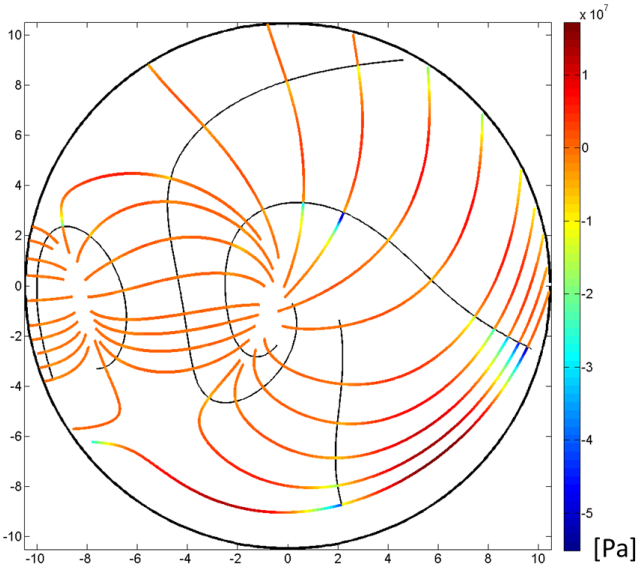

Figure 38. Normal stress distribution in the turning vanes of a StreamVane distortion screen representative of a hybrid wing body swirl profile.

A trade study was performed to see the effects of varying axial velocity and vane thickness (Figure 39). Factor of safety increases with vane thickness and decreasing axial velocity. In order to obtain a specific FOS, the length of each turning vane can also be shortened to reduce the stress in the beam. The tradeoffs of locally increasing the vane thickness include an increase in turbulence, an increase in geometry complexity, added material cost, and an increase in local and global blockage, the first of which can lead to choking. For the application of a swirl screen in the distortion test rig, and given previously cited reasons, a FOS of 5 was chosen as a minimum. It was decided to include four more structural supports and extend an existing support, which would serve the purpose of dividing the length of the turning vanes with a FOS that was lower than 5 by approximately half to lower the stress (Figure 40). This achieved the desired goal of a minimum FOS of 5 everywhere, with the actual minimum being 5.40, a maximum local blockage of 35%, and a global blockage of 13.20%.

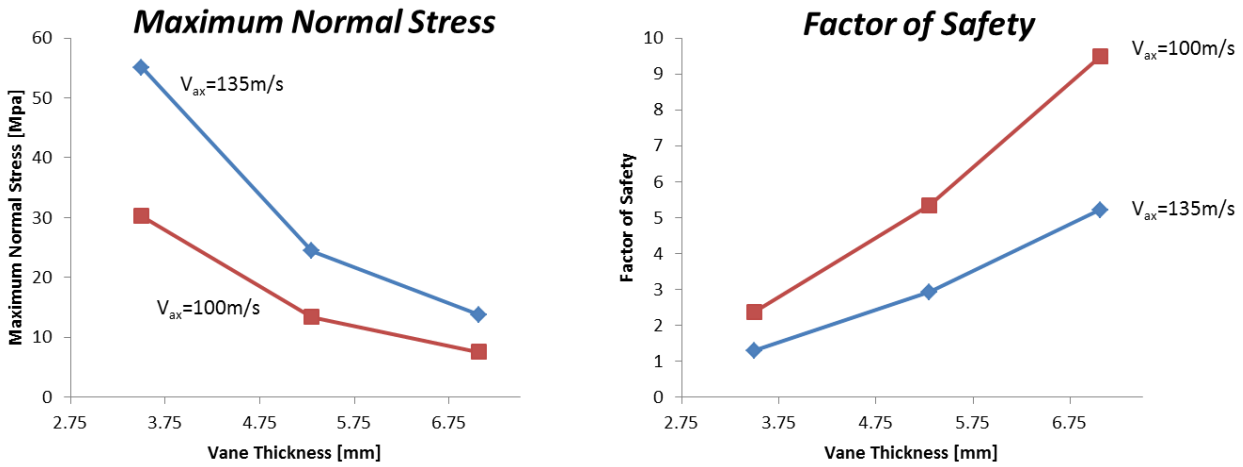

Figure 39. A trade study was conducted to determine the relationship between vane thickness and factor of safety at different axial velocities.

The material properties for the stress analysis were those of ULTEM* 9085, a high strength-to-weight ratio thermoplastic. It was chosen for having the highest tensile strength of plastic materials available for additive manufacturing. Because of the nature of the Fused Filament Fabrication (FFF) technique, the tensile strength varies with build orientation [59], having maximum tensile strengths of 81MPa, 67MPa, and 43MPa for the X-, Y-, and Z-directions of build, respectively. Minimum tensile strengths of 57MPa, 40MPa, and 32MPa were measured for the X-, Y-, and Z-directions of build, respectively. There is a discrepancy because of the

variation of two other parameters, raster angle and air gap. The material data sheet for ULTEM cited a maximum tensile strength of 71.6MPa, which was used in all calculations.

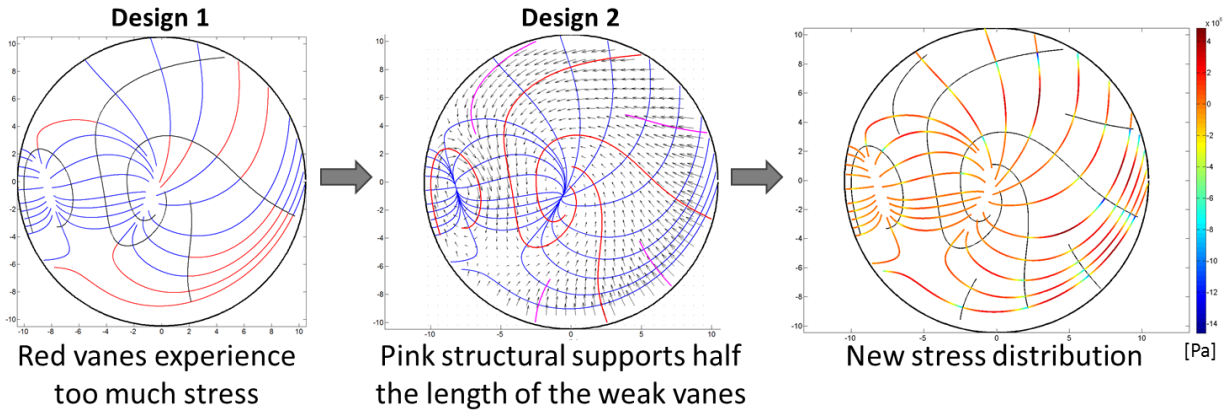

Figure 40. Another iteration of the hybrid wing body StreamVane screen included structural analysis, which indicated that failure was likely without more structural integrity.

This analysis gives confidence to the StreamVane design in light of concerns about engine safety, high screen cost, and screen performance. In order for the boundary condition assumptions to be valid, a 1/8" thick shroud is added around the outer ring of the vanes that acts as a fixed wall as well as provides protection to the turning vanes from friction in the test rig as it is rotated for measurements. An 8° chamfer is included at the end of the shroud to transition smoothly into the test rig wall. All vane/structure intersections are filleted where possible for added structural integrity, which also necessitates an offset of the leading edge of the turning vanes from the upstream flange face. A hole pattern (0.25"Ø every 15°) is included in the flange to mate directly to the test rig hole patterns; an adapter ring is used to mount the screen to the screen rotator device used by the Turbomachinery and Propulsion Lab. Of the current five steps outlined in the StreamVane method in §1.2.1, stress analysis would become step six, but is actually an iterative step that encompasses the entire method.

In future work, the shear stress distribution could also be found to obtain a more accurate estimate of the stress in the turning vanes. Ideally a structural and CFD mesh would be generated so that pressures from an appropriate 3D CFD analysis could be input into a structural FEA analysis for a higher order estimation. Additionally it is possible that the flat plate blade profiles are not achieving the desired turning angle because of losses due to separation, especially for extreme turning requirements. An airfoil blade profile or thickness profile could help reduce

these losses. Linear cascade data is readily available to obtain the lift force for a blade profile, however the moment of inertia of the airfoil needs to be calculated.

A.1.3 StreamVane Leading Edge Design

Before the first full scale StreamVane was ordered, a sample section of the screen was printed to ensure quality manufacturing. It was discovered that, because of the required build orientation, the leading edges of the all of the vanes were very rough. There were concerns about the effect the leading edge roughness would have on aerodynamic performance, so the leading edge was redesigned. The intent was to smooth out the leading edge in the design so that it would be printed smooth as well, with some help from a hand sanded finish.

It was agreed upon immediately that the leading edge could be smoothed by reshaping it as a half ellipse. Three values of semi-major axis were chosen as a leading edge profile (Fig. 41) and a CFD trade study was completed to determine which leading edge profile would perform the best, which was defined as achieving most closely the desired turning. The procedure of geometry and mesh generation was followed as outlined in [26]. A sample mesh of 185,000 elements is shown in Fig. 42. The geometric angle of attack was kept at 0 degrees and the angle of attack was varied in the CFD solver FLUENT. A k-ω SST turbulence model was used with periodic boundary conditions and a pressure based solution. The hybrid wing body StreamVane screen was queried for flow conditions. Table 5 details the parameters chosen.

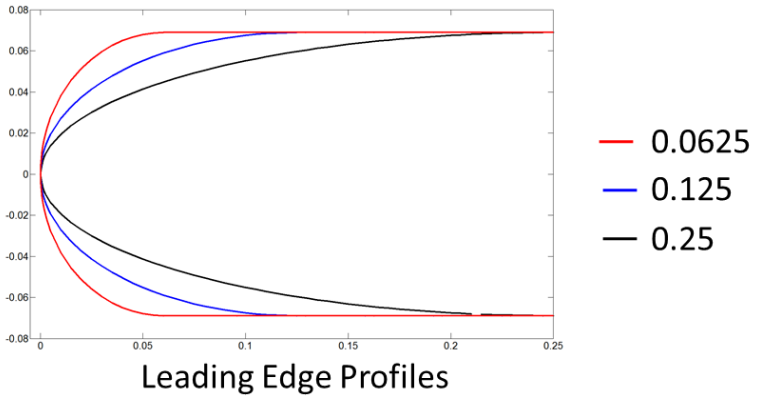

Figure 41. Three leading edge profiles were investigated for aerodynamic performance a part of a constant thickness airfoil.

The results of the CFD study are in Table 6 and Fig. 43. The flat plate profile suffered from separation around the sharp corners of the leading edge. The two largest value of semi-major axis provide 0.5° more turning and are close to each other in value. Because of the design of the StreamVane screen, the trends seen are expected throughout the screen. Three sample parts were 3D printed, each with a different leading edge to see which ones were manufactured to a high standard. The thinnest vane did not print as well as expected, and, with support from the CFD analysis, the 0.125 inch option for a semi-major axis of an elliptical leading edge was chosen and implemented.

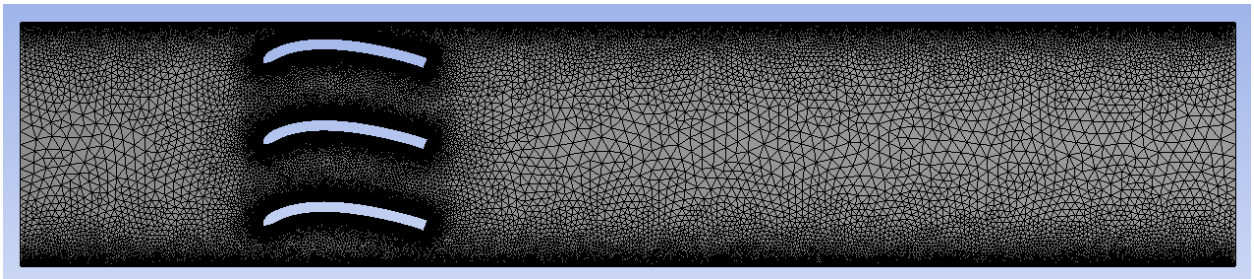

Figure 42. The mesh for a linear cascade of turning vanes with boundary layer considerations and periodic boundary conditions on the top and bottom domains.

Table 5. Aerodynamic parameters to be kept constant for each simulation.

Parameter	Value
C_l	2
AoA	30°
Chord	2in.
Mach No.	0.35

Table 6. Results for an angle of attack of 30°, with a trailing edge angle of attack of 22°.

Profile Type	Avg. Turning [deg.]	Avg. Vel. Magnitude [m/s]
Flat Plate	-47.724	109.470
0.0625	-48.411	109.427
0.125	-49.11	109.418
0.25	-49.028	109.452

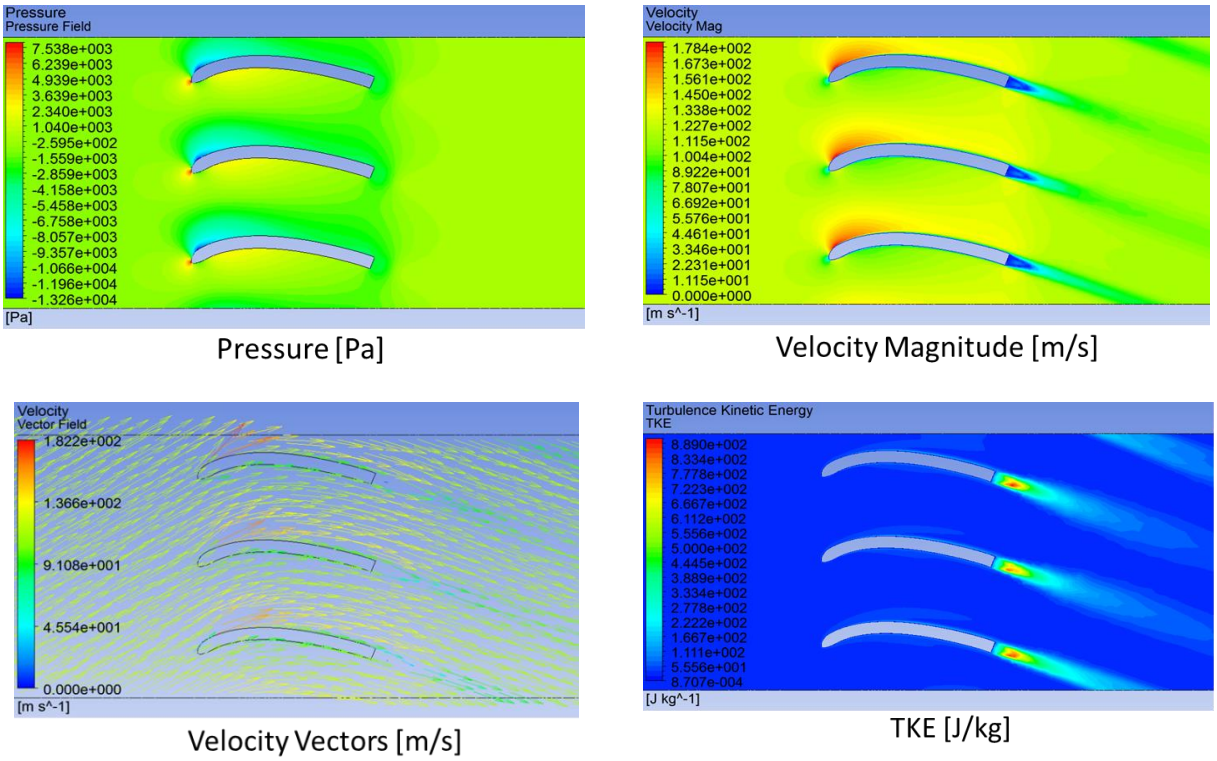

Figure 43. CFD results for the leading edge profile with a semi-major axis of 0.125 inches for a flat plate profile.